SYNTHESIS, ADVANCED CHARACTERIZATION, AND OPTOELECTRONIC/BIOLOGICAL APPLICATIONS OF NOVEL GRAPHENE QUANTUM DOTS

by

MD. TANVIR HASAN

Bachelor of Science, September 2007
Chittagong University of Engineering and Technology, Chittagong, Bangladesh

Master of Science, August 2018
Texas Christian University, Fort Worth, TX, USA

Submitted to the Graduate Faculty of the

College of Science and Engineering

Texas Christian University

in partial fulfillment of the requirements

for the degree of

Doctor of Philosophy

December 2019

ACKNOWLEDGMENTS

I want to express my earnest gratitude to my advisor Dr. Anton V. Naumov for his close supervision, guidance, and support so that this work can be accomplished. His motivation, continuous encouragement, patience, enthusiasm and excellent mentorship help me to overcome any crucial step throughout my Ph.D. research. It was an honor to work under his supervision. I am grateful to Dr. Yuri Strzhemechny for having faith in me and making an exception by evaluating my application on such short notice for the admission at TCU and helping me from day one at TCU with great advice. Next, I am glad to thank my committee members Dr. Yuri Strzhemechny, Dr. Zyzmunt (Karol) Gryczynski, and Dr. Hana Dobrovolny for their valuable suggestions, remarks and critical comments to successfully write this dissertation. I am also thankful to all other faculty members, staff, and my fellow graduate students of physics and astronomy department for offering assistance/advice if needed.

I am extremely thankful to my parents (Md. Moshraf Hossain Sarker and Hosne Ara Begum), maternal aunt (Shahnaz Parvin), paternal uncle (Zahirul Haque Sarker), maternal uncle (Dr. A.K.M Mustafizur Rahman), grandparents (Late Ashraf Ali and Fatema Begum), father/mother in laws (Dr. Abdus Salam and Shamsunnahar Nira), other relatives, and friends back home for their patience, faith, support and encouragement to pursue my higher studies.

Last but not least, I am really thankful to my wife Sadia Afrin, for her sacrifice, patience, and unending support so that I can pursue my graduate studies at TCU. I also want to thank her for all the delicious foods that she cooks (even after holding a full-time job), which provides me the necessary nutrition/energy for doing research and completing this work.

TABLE OF CONTENTS

LIST OF FIGURES

LIST OF TABLES

LIST OF ABBREVIATIONS

AFM – Atomic force microscopy

ATR – Attenuated total reflection

CdSe (cadmium selenide), PbS (lead sulfide), CdS (cadmium sulfide)

EDX – Energy dispersive X-ray spectroscopy

EL – Electroluminescence

FL – Fluorescence

FTIR – Fourier transformed infrared spectroscopy

GO – Graphene oxide

GQDs – Graphene quantum dots

HRTEM – High-resolution transmission electron microscopy

LEDs – Light-emitting devices

MWCO – Molecular-weight-cutoff

NaOCl – Sodium hypochlorite

N-GQDs – Nitrogen-doped graphene quantum dots

NIR – Near-infrared

NS-GQDs – Nitrogen/sulfur co-doped graphene quantum dots

Oz-NGQDs – Ozone-treated NGQDs

PEDOT:PSS – poly(3,4-ethylene dioxythiophene):poly(styrene sulfonate)

PL – Photoluminescence

PLE – Photoluminescence excitation/emission

QDs – Quantum dots

QY – Quantum yield

RGO – Reduced graphene oxide

RGQDs – Graphene quantum dots prepared from reduced graphene oxide

SEM – Scanning electron microscopy

TEM – Transmission electron microscopy

TiO_2 – Titanium dioxide

UV – Ultraviolet

UVT-NGQDs – UV treated N-GQDs

CHAPTER – 1

Background Study

1.1 Motivation:

Semiconductor quantum dots (QDs) are highly regarded nanomaterials because of their unique optical/electronic/structural properties that have great potential for optoelectronic devices and biological imaging applications. Although inorganic quantum dots such as CdSe (cadmium selenide), PbS (lead sulfide), CdS (cadmium sulfide) possess excellent optical/electronic properties including tunable bright emission in visible/NIR-I/II region, high extinction co-efficient, longer lifetimes, considering the complex high cost synthesis process, intrinsic cytotoxicity of some inorganic materials up to becoming potential environmental hazard, the majority of the inorganic QDs are unsuitable for household optoelectronic or biological applications. On the other hand, graphene quantum dots (GQDs) offer comparable optical/electronic properties, an eco-friendly/cost-effective/facile/scalable synthesis process along with low cytotoxicity and no potential harmful impact on the environment. This combination makes GQDs highly desirable material that can be utilized in solution-processable optoelectronic and biotechnology industry applications. Our goal was to develop simple, straightforward, and cost-effective synthesis routes to produce novel GQDs with novel optical and electronic properties that can be used as an active material to fabricate electroluminescence devices, solar cells, photodetectors, and a bioimaging probes for in-vitro/in-vivo/ex-vivo imaging. Bottom-up and top-down synthetic approaches implemented in this work allow synthesizing heteroatoms

(Oxygen/Nitrogen/Sulfur) doped GQDs exhibiting fluorescence with high quantum yield in visible and near-infrared (NIR) suitable for applications in optoelectronics and biomedicine.

1.2 Questions that will be answered by this study:

i. Can we synthesize graphene quantum dots (GQDs) with superior optical properties using a simple/scalable/eco-friendly bottom-up approach?

ii. Can we utilize these solution-processable GQDs for optoelectronic device applications?

iii. Can we utilize these GQDs for biological imaging applications?

iv. Can we modify the optical properties of these GQDs for specific applications?

v. Can we produce GQDs exhibiting visible/near-IR fluorescence using a simple/cost-effective top-down approach?

vi. Can these GQDs (prepared from a top-down approach) be used for biological imaging applications?

1.3 Literature review:

1.3.1 Graphene

Graphene is a two-dimensional carbon allotrope which is considered as the building block of graphite, reduced graphene oxide, graphene oxide, carbon nanotubes, fullerenes, graphene quantum dots, graphene nanoribbons, graphene nanowires, graphene nanoplatelets, etc. It has one atomic layer thick sp^2 hybridized hexagonal/honeycomb-shaped crystal lattice structure (Figure-1.1) having a bond length of 0.12 nm[3]. In graphene layers, 2s, $2p_x$, and $2p_y$ orbitals hybridize in a way that each carbon is covalently bonded with three neighboring carbons by sigma bonds whereas the $2p_z$ orbital forms a π-bond that is shared by the neighboring carbons forming a π electron system on the graphene surface. Usually, for metals and semiconductors, the valence band either overlaps with the conduction band (metals) or it is separated by a small gap from the conduction band (semiconductors). Graphene, on the other hand, is known as a zero-bandgap semiconductor or a semi-metal. By using density functional theory (DFT), the electronic band structure of single-layer graphene can be calculated revealing its unique character (Figure 1.2) having conical structures formed by its energy bands called Dirac cones (Figure 1.3). DFT indicates that due to the formation of such unique conical band structure, delocalized electrons from 2p orbital in graphene can act as massless relativistic particles with, however, electron speeds 300 times below the speed of light[1]. Graphene's physical/electronic structure yields remarkable electrical/thermal conductivity, high transparency, superior tensile strength, and high thermal/ chemical stability[4-8] which has a great potential for wide variety of electronic applications. Those include gas and biosensors[9], field emission displays[10], transparent electrodes[11, 12], field-effect transistors[13] and lithium-ion batteries[14]. Graphene has been synthesized utilizing both bottom-

up and top-down approaches. The bottom-up methods include thermal chemical vapor deposition (CVD) using camphor as the precursor on nickel foils[15], plasma-enhanced chemical vapor deposition requiring lower temperature than thermal CVD[16] within a plasma discharge, ultra-high vacuum thermal decomposition on SiC surface[17], and arc discharge methods[18]. On the other hand, the top-down methods include mechanical exfoliation of graphite [13], exfoliation–re-intercalation–expansion of graphite[19], or graphite exfoliation by high-shear mixing[20]. A plethora of synthetic approaches yield graphene with different quality, scalability and production yield. There is always a trade-off between the scale and quality of graphene production: mechanical exfoliation/epitaxial growth methods provide high quality graphene at the smaller scale compared to the graphene produced by chemical exfoliation method which is hampered by low uniformity of the resulting graphene material.

There are other graphene-like materials that can be synthesized via a variety of chemical methods showing similar structure/properties as graphene with a much lower cost such as reduced graphene oxide (RGO) produced by the reduction of graphene oxide (GO) that is in turn synthesized from graphene via chemical oxidation.

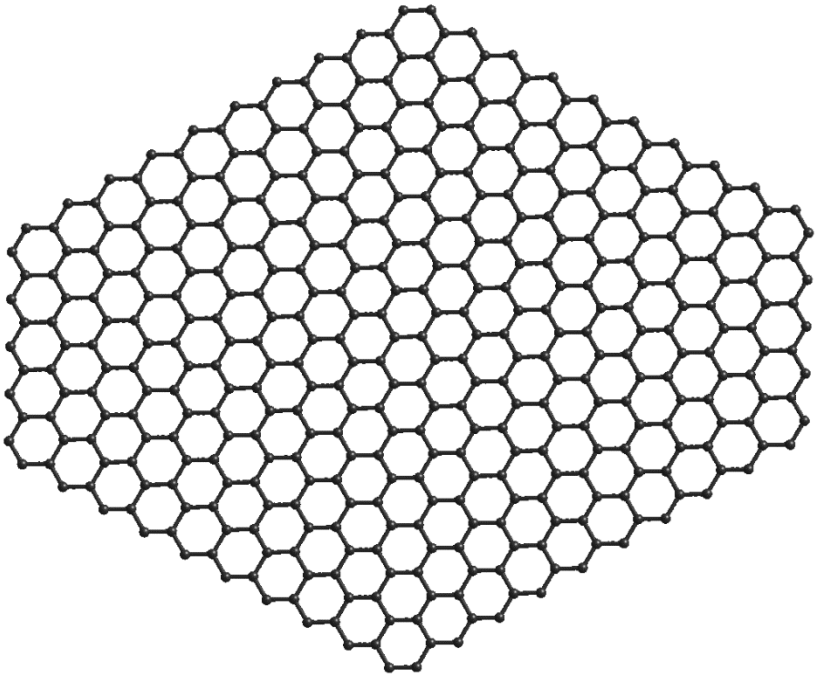

Figure 1.1: Single layer graphene sheet

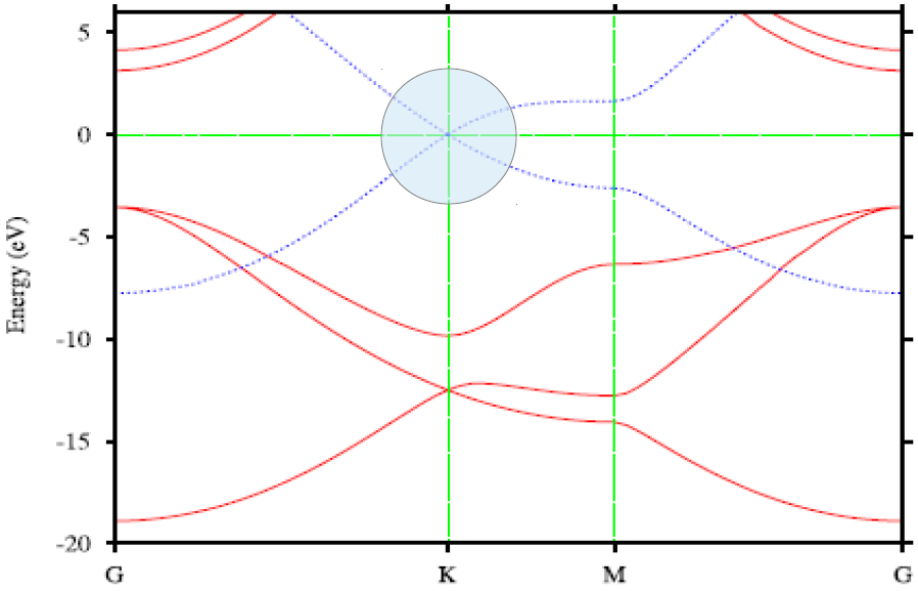

Figure 1.2: Band structure of single graphene layer showing σ bands with solid red lines and π bands with dotted blue lines [2]. In the x axis G represents the origin of the first brillouin zone; K and M represents the corner and border points of the first brillouin zone, respectively.

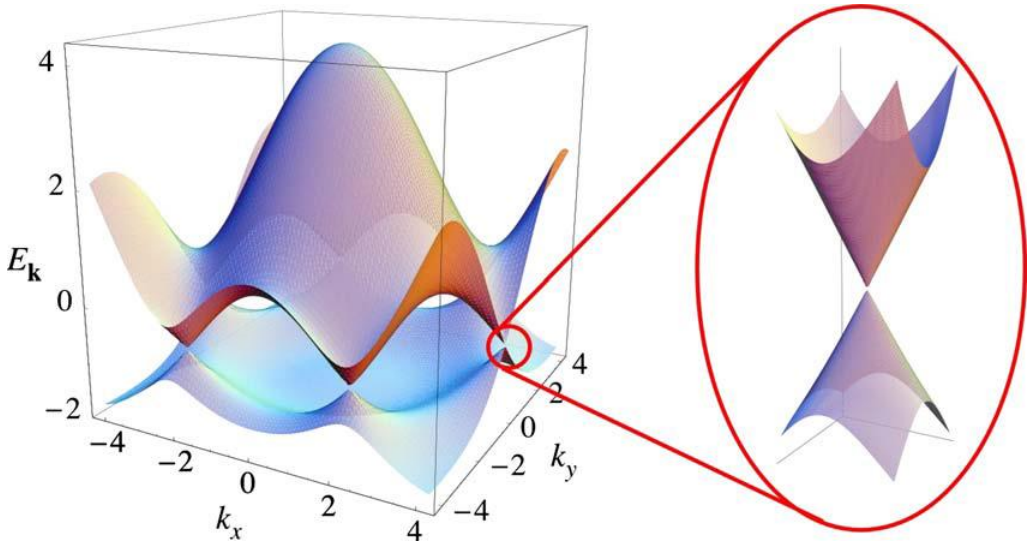

Figure 1.3: Electronic dispersion in the honeycomb graphene lattice.[1]

1.3.2 Reduced graphene oxide

Reduced graphene oxide (RGO) is a graphene-derived material that shows comparable mechanical, electrical and chemical properties to graphene. Usually, graphene oxide (GO) is utilized as a precursor to producing RGO *via* thermal reduction [21] or chemical reduction with hydrazine[22, 23] or sodium borohydrate[24, 25]. GO has a number of oxygen-containing functional groups on its surface, which are reduced via these processes making it more hydrophobic and resulting in unstable dispersion in water. However, the stability can be improved by further chemical processing such as pH variations along with aqueous ammonia addition that increases the stability of hydrazine-treated RGO in aqueous suspension [26]. Although reduction process yields the removal of functional groups on RGO graphitic sheet, some residual defects may still exist (Figure 1.4) in the place of removed functionalities decreasing the quality of the reduction-produced graphene. RGO can still be produced with very high conductivity (6300 Scm^{-1}), and

mobility (320 $cm^2V^{-1}s^{-1}$) synthesized via Joule heating reduction at 3000K[27] which shows great promise for electronics applications. However, due to the absence of substantial bandgap (optical inertness) it can not be used as an active material for optoelectronic or any other fluorescence-based applications.

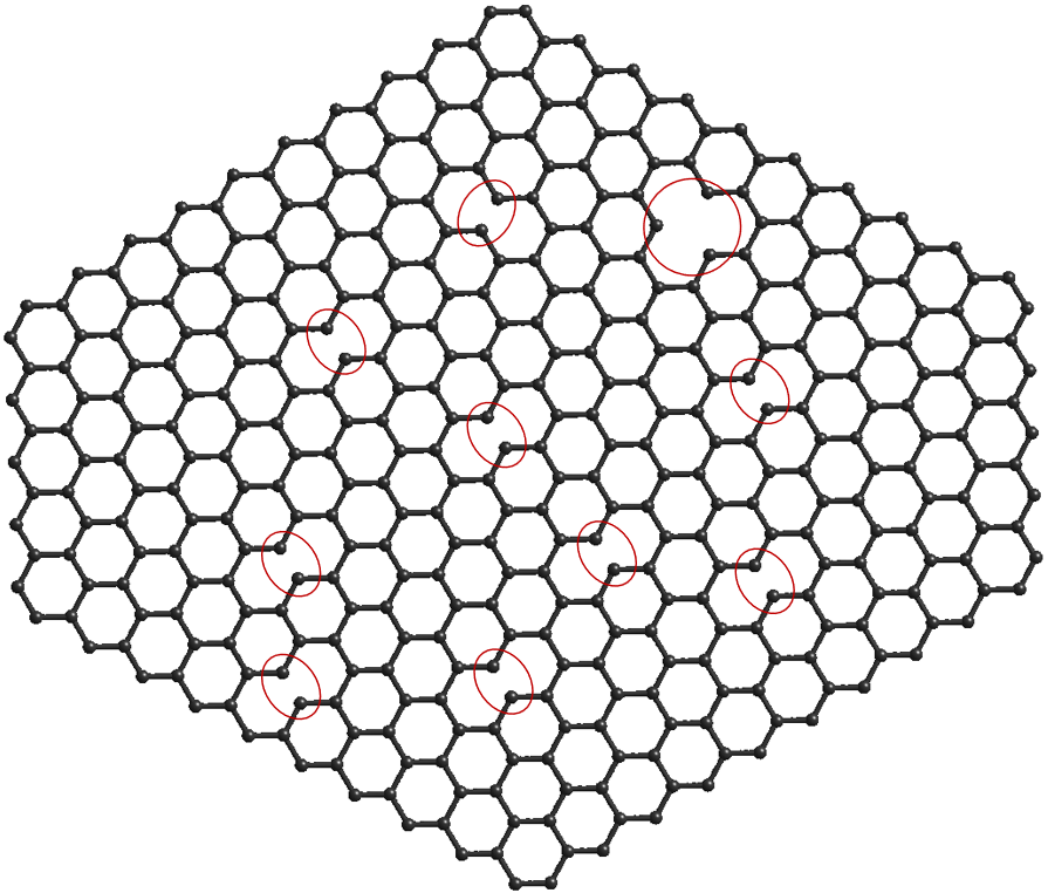

Figure 1.4: Single layer reduced graphene oxide (RGO) sheet. The red marked regions represent some defects on RGO.

1.3.3 Graphene quantum dots

Graphene quantum dots are a fragment of graphene sheet with small enough (on the order of several nanometers) dot-like shape (Figure 1.5 a,b) to exhibit quantum confinement-induced properties. Size-dependent quantum confinement takes place when the size of a semiconducting nanomaterial is comparable to the excitonic Bohr radius of the bulk material[28]. Since bulk graphene is a zero-bandgap semiconductor and delocalized electrons in graphene behave as massless relativistic particles[1, 7], the excitonic Bohr radius of bulk graphene becomes infinite indicating any size of graphene sheet may experience quantum confinement[29]. GQDs are nanometer-sized 0-D (zero-dimensional) structures where excitons remain confined in all three spatial dimensions that, unlike graphene, may exhibit bandgap induced by quantum confinement effect[30]. On the contrary, due to the zero-gap semiconductor bandstructure, graphene is optically inert, which hampers its use as an emissive material for optoelectronic or bioimaging applications. Compared to graphene, derivatives such as graphene oxide (GO), graphene quantum dots (GQDs), and graphene nanoribbons exhibit fluorescence (FL)[31-36] due to the presence of band gaps which makes them highly desirable for a diverse range of emission-based optical applications. Although GO has the advantages of a large heavily-functionalized platform for further modification, it exhibits a very broad emission with a lower quantum yield on the order of 1%[37, 38]. Graphene nanoribbons are complex in production and can not be modified while retaining their properties. On the other hand, GQDs are known to have a more ordered than GO uniform structure with size-confined band gaps[39-42], can be mass-produced and generally exhibit fluorescence with high quantum yields[43, 44] required for optical emissive devices and biological fluorescence probes.

(a)

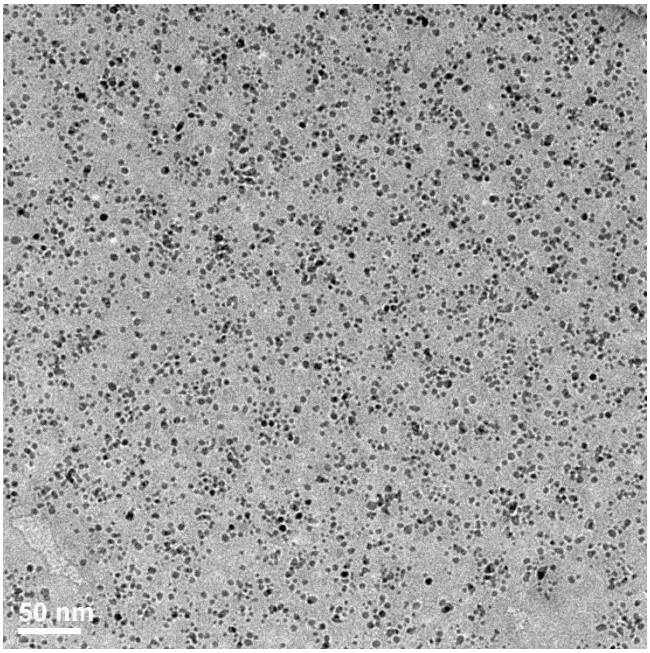

(b)

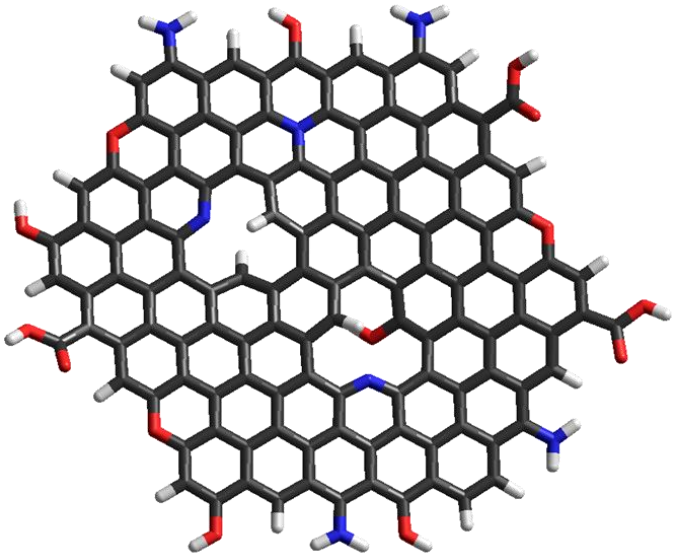

Figure 1.5: (a) TEM (transmission electron microscopy) image of numerous dot-like graphene fragment sheet, (b) Proposed single layer graphene quantum dot with oxygen and nitrogen containing functional groups. The carbon, oxygen, nitrogen, and hydrogen atoms are assigned with black, red, blue, and white color, respectively.

These zero-dimensional carbon allotropes are well-known to have stable fluorescence (FL)[45], remarkable photostability[45, 46], low cytotoxicity[47, 48], good general biocompatibility[47, 49], high water solubility[48], substantial pH sensitivity[50, 51], and low aggregation affinity. Having all these advantageous properties, GQDs show great potential to advance critical areas of modern technology including LEDs[52-54], photovoltaics[55-57], fluorescent bioimaging[58, 59], biosensing[60, 61], pH sensing[62, 63], photoelectrocatalysis[64, 65], photodynamic therapy[66, 67], therapeutics delivery[68-70] and fluorescence-based metal ion detectors[71, 72]. There are mainly two different approaches to synthesize graphene quantum dots: (1) the top-down approach, which involves scission of larger-sized (micrometer) structures into smaller-sized (nanometer) graphitic sheet yielding quantum dots, (2) the bottom-up method, that includes step-wise fabrication of GQDs via solution chemistry[73], or the synthesis of GQDs by pyrolysis/carbonization of small organic molecules (carbon precursors) via a hydrothermal method[74, 75]. The top-down approach can be performed either *via* strong acidic oxidation using carbon nanotubes, graphite, or carbon black[76, 77] as precursors, or electrochemical exfoliation using graphite rods or graphene films[78, 79] as carbon sources. Usually, these methods are time-consuming, complex, and provide no/little control over the optical/structural properties of the end products. On the other hand, GQDs synthesized *via* bottom-up approaches provide superior optical properties over top-down approach, but existing processes may involve complicated experimental setup, long reaction times, various starting materials, little/no control over GQD properties, and thus do not necessarily yield GQDs with optimal characteristics.

Compared to their inorganic counterparts, however, GQDs offer a simple/scalable/eco-friendly/cost-effective alternative that shows size-dependent bandgap which is inversely

proportional to the size of conjugated π domains in the case of graphene and the particle size in II-VI materials[42]. Given the mostly surface GQD morphology, the edge/surface also plays an important role in the origin of their emission. This allows for a broader size range for the emissive GQDs as opposed to their counterparts such as SiQDs (silicon-based QDs) that exhibit quantum confinement-induced size-dependent photoluminescence only below 5 nm diameter which is comparable to the excitonic Bohr radius of bulk silicon (~5nm)[80, 81], whereas for GQDs the limit is up to 20 nm[30] due to the emission originating from surface/edge states and their arrangement on GQDs. Depending on the synthetic approach and size-tuning of GQDs, the fluorescence can be either strongly excitation wavelength-dependent over a broad range (350-800 nm) [82-84] or shows a slight/negligible dependence over a shorter wavelength (300-470 nm) range [85, 86]. Excitation dependence arises from the presence of a variety of quantum dot sizes in the sample, each emitting at their particular wavelength. Excitation wavelength-independent emission can be obtained in more size uniform GQDs samples tuned in size and showing single transition with moderate quantum yields[87-90].

It is highly desirable to develop GQDs that can be synthesized using a simple, scalable, eco-friendly, and cost-effective process. Currently, the production of GQDs is limited as their synthesis is generally quite complex and yield GQDs with poor solubility/low production yield[91]. Additionally for the field of optoelectronics it is critical to developing a multifunctional GQD material with properties allowing utilization as an optically active layer to fabricate solution-processed optoelectronic devices such as LEDs, solar cells, photodetectors with outstanding device characteristics. Also, the optical properties, especially the NIR emission capabilities of these biocompatible GQDs, can be explored further for *in-*

vitro/in-vivo/ex-vivo bioimaging applications. Most GQDs exhibit emission in visible which only allows performing *in-vitro* imaging. Therefore, biocompatible GQDs with unique NIR emission properties at NIR excitation will enable *in-vivo* imaging with reduced autofluorescence background, less scattering, and high penetration depth. In this work, we have developed new synthetic procedures to produce several types of GQDs meeting the aforementioned needs which have not been developed so far. Further chapters will describe their characterization and utilization in optoelectronic and bioimaging applications.

1.3.4 Fluorescence

Upon photo-excitation of nanomaterials/molecules, the ground state electrons absorb the photon energy and get excited, leading to an electronic transition of these electrons from ground state to excited electronic state (Figure 1.6). After reaching the excited state, the electrons will undergo a non-radiative relaxation process *via* internal conversion and reach the lowest excited state. The electrons may release the gained energy from the lowest excited state either in a radiative or non-radiative fashion and come back to the ground state. The release of a photon via radiative relaxation is known as fluorescence. As a result of this process, the emitted photon is less energetic than the absorbed one.

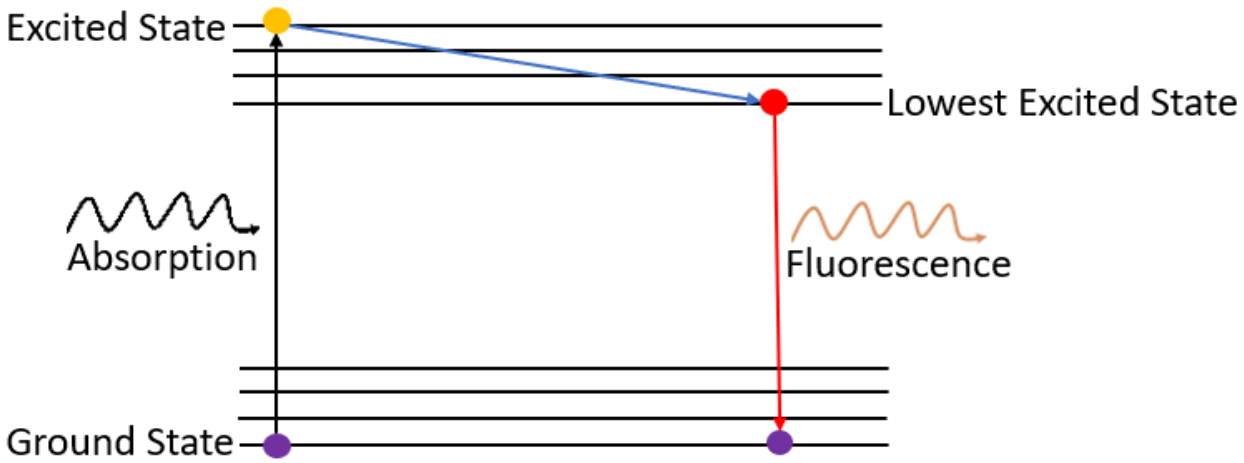

Figure 1.6: A schematic of fluorescence mechanism.

The non-radiative relaxation of the excited electron to the ground state does not result in photon emission leading to the lowered quantum yield for that particular material. The fluorescence quantum yield can be defined as the ratio of number of photons emitted to the number of photons absorbed, mainly describing the efficiency of the fluorescence process for a specific fluorophore. The fluorescence quantum yield can be measured either using a comparative method which renders a relative quantum yield or special instrumentation can be utilized to measure the absolute quantum yield. This can be accomplished via the experiment involving an integrating sphere allowing to measure absolute quantum yield. Generally, absolute quantum yield is expressed as:

$$Quantum\ Yield = \frac{Number\ of\ photons\ emitted}{Number\ of\ photons\ absorbed}$$

The measurement of relative quantum yield of fluorophores using a comparative method was first introduced by Parker and Rees in 1960[92] which can be described using the following equation.

$$\phi_{sample} = \phi_{ref} \times \left(\frac{FLI_{sample}}{FLI_{ref}}\right) \times \left(\frac{1 - 10^{Abs_{ref}}}{1 - 10^{Abs_{sample}}}\right) \times \left(\frac{\eta_{sample}}{\eta_{ref}}\right)^2$$

In the above expression, Φref denotes the quantum yield of the reference materials, FLI represents the experimentally measured integrated fluorescence intensity, Abs indicates the absorbance of materials at the excitation wavelength and η is denoted as the refractive index of the solvents.

Fluorescence has a plethora of practical applications including fluorescent lamps, fluorescent labelling with dyes in biomedicine, a variety of biological assay applications (e.g. flow cytometry, plate readers), biological and physical fluorescence microscopy, fluorescence spectroscopy, characterization of materials, fluorescence resonance energy transfer (FRET), and other technological applications in the area of gemology, mineralogy, optoelectronics etc[93-97].

1.3.5 Electroluminescence

Electroluminescence is a combined (electrical/optical) process in which electrical energy can be converted to light energy ideally without the generation of thermal energy. If a strong electric field or electrical current is applied across an electroluminescent material, the electrons in the conduction band will recombine with holes in the valence band, releasing the energy via radiative (emission of light) or non-radiative (heat dissipation) recombination. The radiative recombination of electrons/holes is regarded as electroluminescence. Electroluminescence can be obtained either intrinsically (high-field electroluminescence under the influence of the electric field) or via the injection of charge in a semiconducting material[98]. In order to achieve the high-field electroluminescence, a bias voltage is applied to develop a high electric field within the phosphor

material (could be either fluorescent or phosphorescent) which excites the luminescence species resulting in EL emission upon the relaxation of the excited state of the emissive centers. The injection of carriers can be performed within the semiconductor materials using a small bias voltage resulting in the injection of electrons from the cathode terminal and holes from the anode terminal recombining and exhibiting electroluminescence within the semiconducting layers. Like fluorescence, electroluminescence also has many important applications such as LEDs (light-emitting devices), backlights for LCDs (liquid crystal displays), electroluminescent lighting, optical logic circuits, etc.

CHAPTER – 2

Photo- and Electroluminescence from Nitrogen-doped and Nitrogen-Sulfur co-doped Graphene Quantum Dots[46]

2.1 Overview:

In this work, a bottom-up approach with single glucosamine hydrochloride (glucosamine-HCl) precursor is used for the first time to produce nitrogen-doped graphene quantum dots (N-GQDs) and a separate thiourea-driven reaction to synthesize nitrogen/sulfur co-doped graphene quantum dots (NS-GQDs), *via* a microwave-assisted single-step hydrothermal method. Structural and optical characterization was performed by TEM (Transmission electron microscopy), AFM (Atomic force microscopy), SEM (Scanning electron microscopy), FTIR (Fourier-transformed infrared spectroscopy), EDX (Energy dispersive x-ray spectroscopy), Raman, fluorescence, and absorbance spectroscopy. GQDs appear to be well-dispersed and distributed at 5.50±0.20 nm (N-GQDs), and 3.90±0.10 nm (NS-GQDs) average sizes with distinct crystalline structure detected by HRTEM (high-resolution transmission electron microscope). The composition of QDs is assessed via FTIR and EDX indicating a variety of oxygen-containing functional groups with nitrogen (N-GQDs) and nitrogen/sulfur (NS-GQDs) doping of the graphene structure. The synthetic procedure of N-GQDs/NS-GQDs is straightforward, scalable, reproducible, less time consuming, and requires fewer resources than other bottom-up or top-down approaches, allowing for mass GQD production for device and biomedical applications. Also, the source of precursor material used in this work is widely available and inexpensive.

What makes this material novel in addition to a simple/scalable/cost-effective synthesis is the excitation-dependent fluorescence emission that GQDs exhibit both in the visible and near-infrared regions of the electromagnetic spectrum, which is unique as compared to their existing counterparts[99-101]. Although a number of researchers have studied GQD photoluminescence, its origins are still debatable. Some of the well-regarded mechanisms include it is recombination of electron-hole pairs originating from localized sp^2 graphitic carbon platform surrounded by functionalized sp^3 carbon [102], size-dependent quantum confinement effects[103, 104], emissive defect states[85, 103, 105], or selective surface passivation[83, 85]. We propose that N-GQD/ NS-GQD emission originates from the combination of quantum confinement effects (size-dependent band gap) and potentially, as in graphene oxide, due to the types/arrangements of emissive trap states associated with functional groups. This also includes states originating from surface passivation of the GQD surface by amino/thiol groups originated during the hydrothermal reaction.

The structural composition of these GQDs manifests in unique optical properties with high (10 to 60%) quantum yield, blue/green excitation-dependent fluorescence in the visible attributed to size-dependent band gaps, and a second emission feature in the near-IR at 800-900nm potentially arising from the edge/defect states and their arrangements. In the present work, we have utilized these remarkable optoelectronic properties of GQDs in device applications. Electroluminescence devices were fabricated with these GQDs in a simple solution-processed method involving spin-coating of materials on ITO (Indium-doped tin oxide) electrodes with silver paste anode. N-GQDs serve as a recombination layer between PEDOT:PSS (poly(3,4-ethylene dioxythiophene):poly(styrene sulfonate)) and silver. These devices show observably bright electroluminescence emission in green/yellow for N-GQDs both at cryogenic and room

temperature. N-GQDs and NS-GQDs have excellent aqueous solution stability as well as tunable electronic structure, which allows for inexpensive fast-produced LEDs (light-emitting devices), providing potential advantage over inorganic GaN-devices[106]. Additionally, the use of highly fluorescent nitrogen and sulfur-doped GQDs in organic electroluminescence devices may avoid the use of rare earth element-based Iridium complex as a dopant material[107]. In this chapter, we will describe these devices from fabrication to testing.

2.2 Experimental methods and procedures:

2.2.1 Synthesis/purification/characterization of N-GQDs and NS-GQDs

A commercially available microwave (Hamilton Beach, model: HB-P90D23AP-ST) was utilized to synthesize N-GQDs and NS-GQDs *via* a hydrothermal method. In a standard procedure, a 0.14 M aqueous solution of glucosamine-HCl was placed in a microwave for 40 min at 450 W (Power level 3). Additionally, for the synthesis of NS-GQDs, thiourea was used as a source of sulfur, with a 1:1 ratio of thiourea to glucosamine-HCl. As prepared graphene quantum dots were collected and purified utilizing bag dialysis with 0.5–1 kDa MWCO (molecular-weight-cutoff) membrane for seven days as the DI water dialyzed against was replaced daily. After such purification, a synthesis yield of (15-20) % was achieved. To verify the efficiency of this purification process, Benedict's test[108, 109] was utilized to detect the presence of glucosamine precursor in GQDs. For as-prepared GQDs, the concentration of glucosamine assessed *via* the pre-quantified detection range of this test was observed to be over 0.15 mg/ml (Figure 2.3a) showing the presence of glucosamine precursor. However, a negative result was observed for the purified GQDs suggesting minimal/negligible presence of unreacted materials in the suspension of bag-dialyzed GQDs (Figure 2.3b).

Transmission Electron Microscopy (Model: TEM JEOL JEM-2100) was utilized for the morphological characterization of N-GQDs and NS-GQDs. Samples for TEM were prepared on the carbon-coated 200-mesh copper grid under ambient conditions. Optical characterization was performed via absorption and fluorescence spectroscopy. Fluorescence spectra were measured using SPEX NanoLog, Horiba Scientific spectrofluorometer in the regions of 300 nm to 1000 nm with the excitation varied from 280 to 800 nm. Absorbance was recorded in the range of 200 to 800 nm with Agilent Technologies (Cary 60 UV-Vis) absorption spectrometer. Chemical composition of N-GQDs and NS-GQDs was assessed via the ATR (attenuated total reflection) mode of the Thermo Nicolet Nexus 670 FTIR. The samples for FTIR were freeze-dried using a Labconco, FreeZone 4.5 lyophilizer to reduce the water background. Raman spectrometer (DeltaNu) was used to characterize the GQDs with 785 nm excitation at 100 mW peak power. The solution-based GQDs Samples for Raman spectroscopic measurements were spin-coated on a silicon wafer at 1000 rpm for 30 seconds. Finally, in order to assess the thickness profile of both GQDs, a tapping mode AFM (Atomic Force Microscope: NT-MDT nanosolver) was utilized. For AFM measurements GQDs from suspension were spin-coated three times at 3000 rpm for 30 seconds (each time) on a silicon substrate.

2.2.2 Preparation of Benedict's Solution

Benedict's reagent was prepared by mixing sodium carbonate, sodium citrate, and copper-II sulfate in DI water. A known amount of glucosamine/N-GQDs was mixed in 1 mL of Benedict's reagent followed by heating the final solution at 90°C for 20 minutes. Any change of color/precipitation indicates the presence of reduced sugars (free aldehyde group) from

glucosamine precursors (positive result). Different concentrations of glucosamine were tested with Benedict's reagent showing color change/precipitation starting from 50 mg/ml down to 0.15 mg/ml indicating positive results (Figure 2.3a). Any concentration of glucosamine below 0.15 mg/ml showed neither color change nor precipitation (Figure 2.3a). After testing only glucosamine, unpurified quantum dots were tested with Benedict's reagent and showed a slight color change along with precipitation indicating the presence of non-reacted glucosamine with a concentration of $\geq$ 0.15 mg/ml. The purified quantum dots tested with the same reagents show no color change/precipitation suggesting either the absence of non-reactant glucosamine or the presence of only a low amount of impurity (Figure 2.3b). In order to avoid a false-positive result, three samples of the same concentration were tested at the same time yielding similar results.

2.2.3 Calculation of Quantum Yield (QY)

A comparative approach was followed to calculate the quantum yield of N-GQDs/NS-GQDs choosing Coumarin-153 in ethanol (47% QY at 400 nm excitation) and Fluorescein in 0.1 M NaOH (92% QY at 360 nm excitation) as reference materials. We use the following formula to find the QY of both GQDs.

$$\phi_{GQDs} = \phi_{ref} \times \left(\frac{FLI_{GQDs}}{FLI_{ref}}\right) \times \left(\frac{1 - 10^{Abs_{ref}}}{1 - 10^{Abs_{GQDs}}}\right) \times \left(\frac{\eta_{GQDs}}{\eta_{ref}}\right)^2$$

In the above expression, Φref denotes the quantum yield of the respective materials, FLI represents the experimentally measured integrated fluorescence intensity, Abs indicates the absorbance of materials at the excitation wavelength and η is denoted as the refractive index of the solvents. The refractive indexes of water, Coumarin-153, and Fluorescein are considered as 1.33,

1.36, and 1.33, respectively. In order to verify the quantum yield of N-GQDs assessed via a comparative method, an absolute quantum yield of N-GQDs was also measured using a Newport 819C-SL (with spectralon coating) integrating sphere at 405 nm laser excitation.

2.2.4 Device fabrication

Indium doped tin oxide-coated glass (ITO) was used as a substrate for device fabrication due to its excellent transparency and substantial conductivity[110]. ITO substrates were submerged in 10% HCl for 1 hour which was followed by cleaning in acetone for 1 hour using ultrasonic treatment in preparation for further layer deposition and blow-dried by N_2 gas. Prior to deposition on the ITO glass substrate, PEDOT: PSS at a concentration of 1.1 wt % in water with a ratio of 1:1 PEDOT to PSS was filtered using a 0.45 µm pore size syringe filter, and dispersed in an ultrasonic bath for 30 min. After that, 200 µl of PEDOT: PSS solution was spin-coated on treated ITO glass at 3000 rpm for 20 seconds, which was further oven-baked for one hour at 120 °C. This was followed by the deposition of N-GQDs on the ITO-PEDOT:PSS *via* spin-coating (300 µl of 5 mg/mL aqueous suspension of N-GQDs at 3000 rpm for 20 s). The spin-coated sample was further annealed at 120 °C for one hour. Finally, a conductive silver paste was deposited on the top of the device to make the electrical contacts. Before testing the device, the morphological characterization of the LEDs was performed via Scanning Electron Microscopy (JEOL-JSM-7100F). In device testing experiments, a 15V (Harrison 6205B DC power supply) bias voltage was used for the electroluminescence experiments providing electron and hole current. We further utilized the Keithley 2420 Source Meter Unit (SMU) instrument to measure the turn-on voltage of both devices. Finally, in order to record electroluminescence under the application of DC bias voltage, the devices were placed inside a Horiba Spex Nanolog fluorescence spectrometer and the

spectra were recorded continuously as a function of applied bias. In order to confirm the electronic nature of the emission this experiment was repeated under liquid nitrogen temperatures and the photoluminescence of the devices was also measured using the Ocean Optics (S2000) spectrometer at 365 nm excitation wavelength.

2.3 Results and Discussion:

Aqueous glucosamine-HCl or glucosamine-HCl with thiourea was used as low-cost starting materials for the synthesis of N-GQDs or NS-GQDs. These precursor materials undergo a microwave-assisted hydrothermal process in the presence of continuous uniform microwave treatment for 40 min yielding well-distributed GQDs in a stable aqueous suspension. We utilized glucosamine-HCl as a single precursor for the source of carbon and nitrogen dopants to synthesize N-GQDs and both glucosamine/thiourea as a source of carbon/nitrogen and only thiourea as a source of sulfur to produce NS-GQDs. In addition to that, thiourea works as a catalyst for the dehydration process and provides nitrogen and sulfur for doping. With continuous microwave treatment, inter-molecular dehydration takes place, resulting in a polymeric chain to produce N-GQDs (Figure 2.1). After this polymerization process, at a supersaturation condition, a burst of nucleation takes place followed by the doping of nitrogen/nitrogen-sulfur to form N-GQDs/NS-GQDs. This growth mechanism of GQDs is illustrated in figure 2.1 *via* a schematic diagram. The formation/growth of carbon nuclei is verified by the crystalline lattice structure images of GQDs captured by HRTEM indicating the presence of graphene structure and thus characterizing the product as graphene quantum dots as opposed to just carbon dots produced by a variety of similar hydrothermal methods. It is expected that higher powers (> 450W) of microwave radiation may significantly increase the reaction rate to produce GQDs. However, a power level greater than 3

(over 450W) is not considered to avoid the possibility of rapid water evaporation and spill/overflow of the precursor containing aqueous solution.

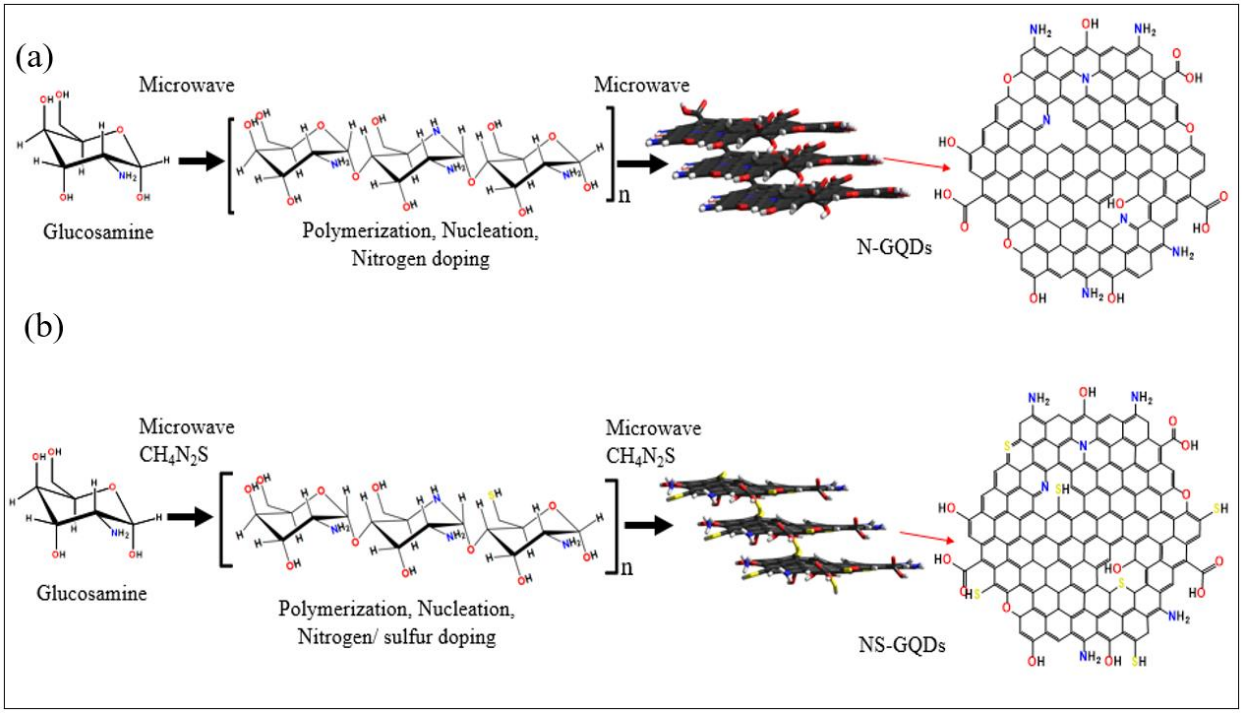

Figure 2.1: Schematic of the growth mechanism of (a) N-GQDS and (b) NS-GQDs.

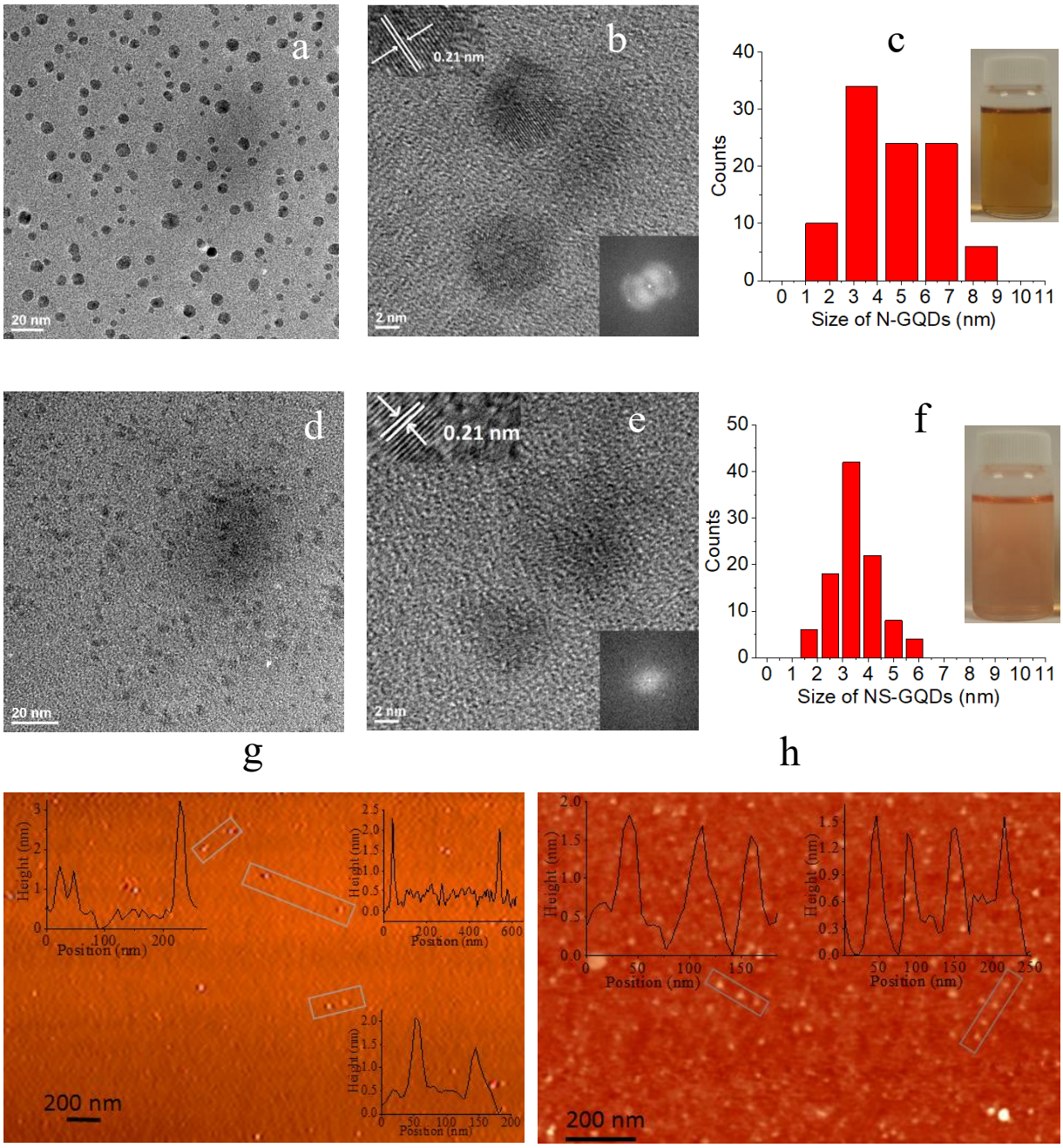

Figure 2.2: TEM images showing the distribution of (a) N-GQDS, (d) NS-GQDs. HRTEM images of (b) N-GQDs, (e) NS-GQDs. Inset: separation between lattice fringes and FFT images of selected area. Size distribution of (c) N-GQDs, (f) NS-GQDs. Inset: As prepared respective GQD samples. AFM height profile for (g) N-GQDs and (h) NS-GQDs.

A dramatic change of physical color from starting water-like transparent solution to yellow (N-GQDs) and pink/orange (NS-GQDs) (Inset of Figure 2.2c,f) is observed after the 40 min microwave treatment, suggesting the formation of new materials including a change in the structural/optical properties compared to the starting ones. Prior to further characterization, GQDs are dialyzed in a 0.5-1 kDa MWCO (molecular-weight-cutoff) dialysis bag for a week to remove the unreacted precursor materials. Dialyzed GQDs are further tested to verify the purification process via Benedict's test showing a minimal/negligible presence of glucosamine precursor (Figure 2.3).

The morphological characterization/distribution of N-GQDs/NS-GQDs is assessed *via* HRTEM in order to characterize the form, structure, and composition of this novel material. The TEM study indicates that the GQDs are individualized, well-dispersed (Figure 2.2a,d) as well as well-distributed, which is shown by the histogram plot describing GQDs size distribution analysis (Figure 2.2c,f). We consider ~100 of GQDs to calculate the average size (diameter) of each type yielding an average size of 5.50±0.20 nm with a range of 1.61 nm to 9 nm for N-GQDs and a 3.90±0.10 nm average size within a range of 1.91 to 6.22 nm for NS-GQDs. Both N-GQDs (Figure 2.2b) and NS-GQDs (Figure 2.2e) show distinguishable lattice fringes with a lattice spacing of 0.21 nm (inset of Figure 2.2b,e) corresponding to (100) plane of graphene[40]. A high crystalline lattice structure is apparent in the fast-Fourier-transform (FFT) images of the chosen area (inset of Figure 2.2b, 2.2e) captured by HRTEM. A qualitative assessment of GQDs atomic percentage is performed using EDX (energy-dispersive X-ray spectroscopy), showing the presence of ~11% nitrogen in N-GQDs (Figure 2.4a,c) and ~8% nitrogen/~2.5% sulfur in NS-GQDs (Figure 2.4b,c). Additionally, AFM (atomic force microscopy) is used to measure the thickness of GQDs, showing

on average up to ~2.5 nm for N-GQDs (Figure 2.2g) and ~1.75 nm for NS-GQDs (Figure 2.2h) which suggests the multilayered and potentially spherical structure of GQDs.

(a)

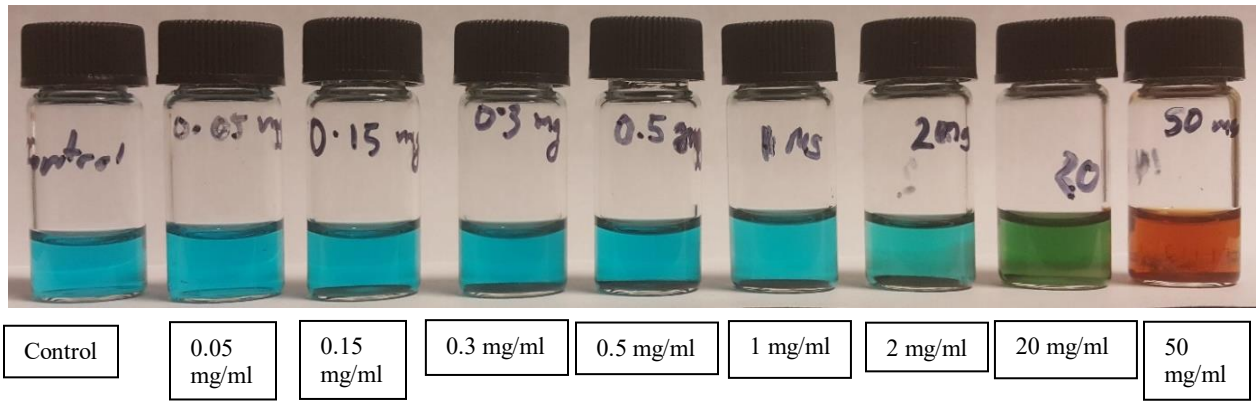

(b)

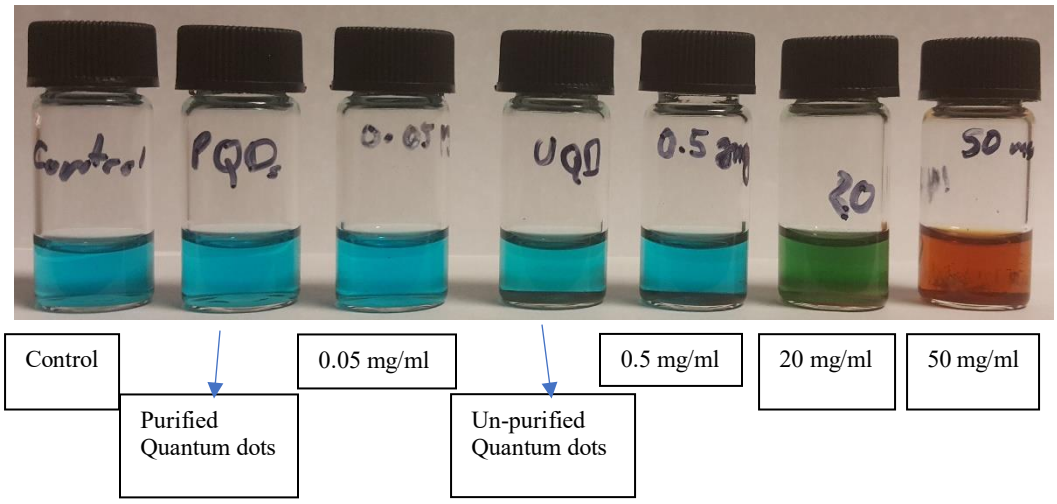

Figure 2.3: Benedict's solution (a) with a different concentration of glucosamine precursor starting from 50 mg/ml (rightmost) down to 0.15 mg/ml showing a change of color/precipitation compared to the control solution (leftmost) but no color change/precipitation for 0.05 mg/ml concentrated solution. (b) with a different concentration of only glucosamine and unpurified quantum dots showing color change/precipitation (except 0.05 mg/ml glucosamine sample) whereas purified quantum dots/low concentrated glucosamine (0.05 mg/ml) exhibiting no color change/precipitation.

The functional groups present on the GQD surface are best assessed via Fourier Transform Infrared Spectroscopy (FTIR). FTIR spectra of N-GQDs/ NS-GQDs show the presence of well-pronounced stretching vibrations of O-H and N-H groups at 3275 and 3090 cm^{-1}[111] (Figure 2.5a,b). The peaks centered at 2935, 1602, 1530, and 1412 cm^{-1} correspond to the vibrational transitions of C-H, C=O of COOH, C=C, C-O-C. Additionally, stretching vibrations of C-OH, C-N/ N-H/ C-H, and C-O are detected at 1330, 1240, and 1021 cm^{-1}, respectively[85, 111]. These peaks are typical for both types of GQDs except C-S, S-H stretching peaks/shoulders at 1159, 2557 cm^{-1} [112-114]for NS-GQDs that are very weak in intensity because of the low sulfur content detected qualitatively by the EDX. The presence of these transitions supports the proposed structural schematic containing oxygen/nitrogen-based addends in Figure-2.1. Raman spectroscopy is utilized to characterize the graphitic structure within the GQD platform showing a sharp G-band at ~1537 cm^{-1} corresponding to the sp^2-hybridized carbons and a weak shoulder at ~1330 cm^{-1} (D band) suggesting the presence of some disordered structures (Figure 2.6a,b).

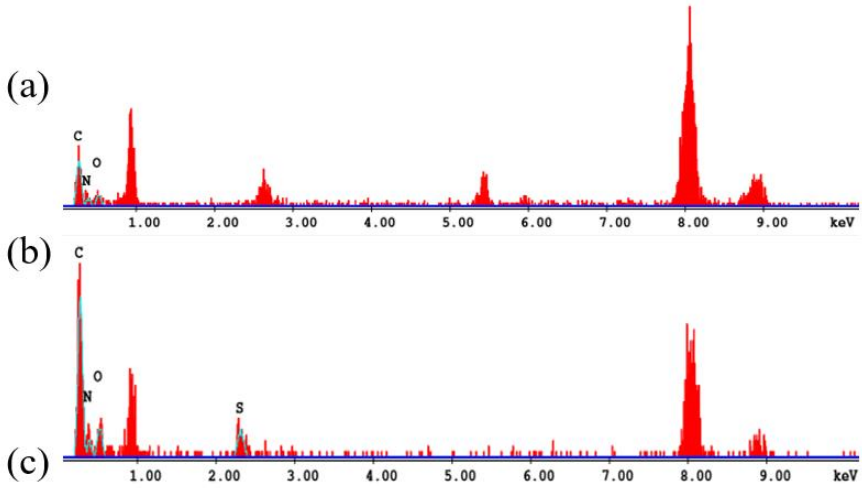

Element	N-GQDs (Wt%)	N-GQDs (At%)	NS-GQDs (Wt%)	NS-GQDs (At%)
CK	73.92	77.98	76.11	81.95
NK	12.11	10.95	9.03	8.34
OK	13.98	11.07	9.19	7.43
SK	N/A	N/A	5.68	2.29

Figure 2.4: EDX measurement of (a) N-GQDs and (b) NS-GQDs (c) Table shows the percentage of elements in N-GQDs and NS-GQDs

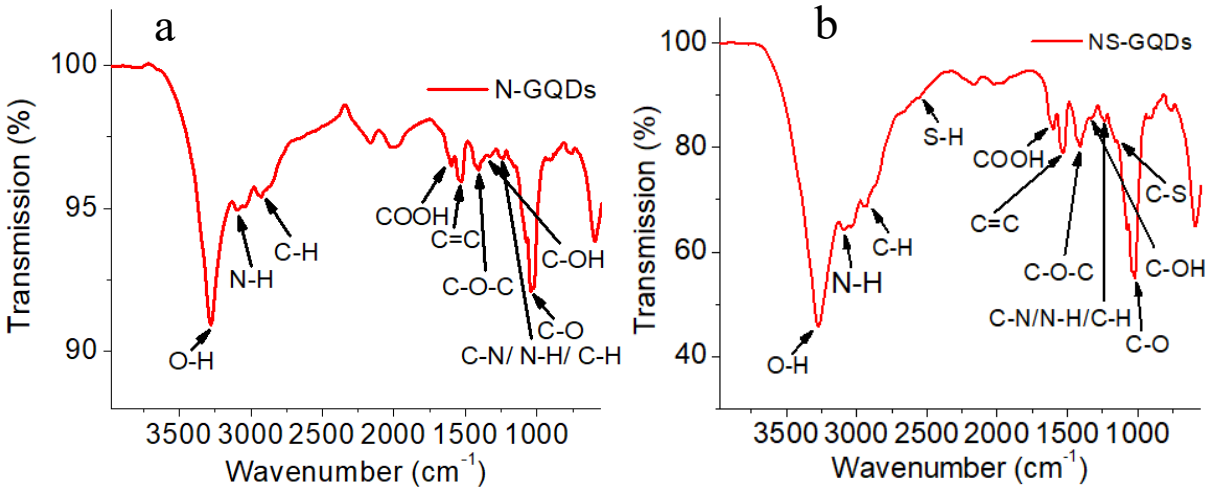

Figure 2.5: FTIR spectrum of (a) N-GQDs and (b) NS-GQDs

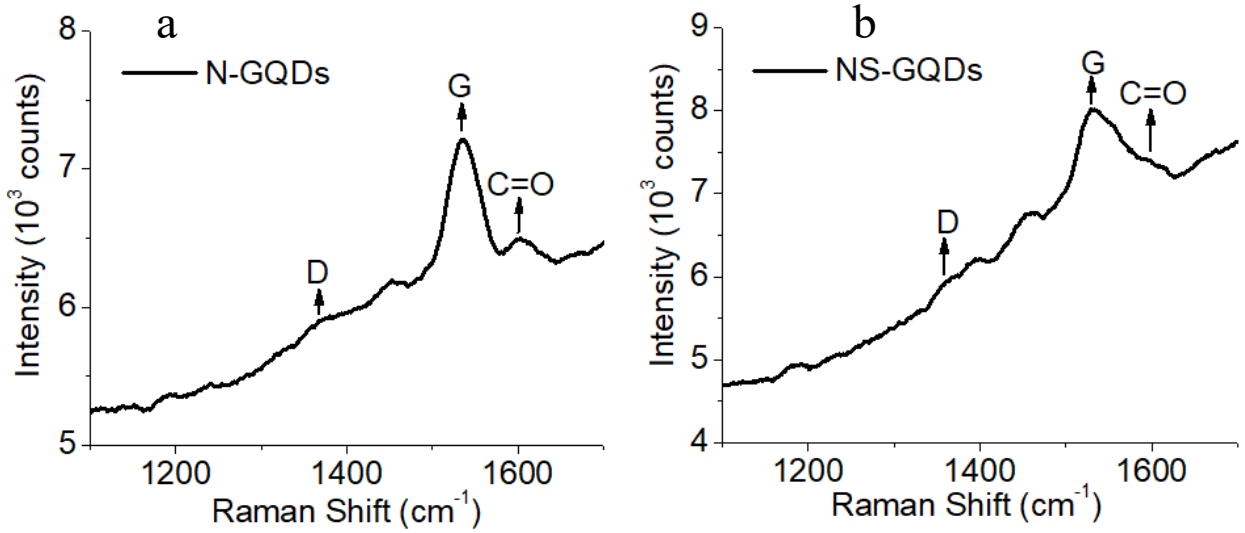

Figure 2.6: Raman spectra for (a) N-GQDs and (b) NS-GQDs

UV-vis and fluorescence spectroscopy techniques are utilized to characterize the optical properties of N-GQDs/NS-GQDs which can be dictated by the synthesis conditions along with the structural properties and the types of functional groups present on GQDs surface. Absorbance measurements of aqueous NGQD show four major features peaking at ~215, 239, 283, ~317 nm (Figure 2.7e) that are attributed to the π-π* electronic transitions of C=C[114], n-π* electronic transitions of C=C, C=O[115], and π-π* transitions of C=N[116], respectively. NS-GQDs show absorption band (Figure 2.7e) at 236 nm consistent with π-π* transition of C=C bond[114] and weak shoulders at 276, 300, 370 nm as the potential signature of n-π* transitions in C=O and C=N bonds. The shifts in absorption peaks between NGQDs and NS-GQDs are likely due to the presence of sulfur dopants in NS-GQDs indicating the interaction of the major absorbing species on the sp^2 platform with the dopants. Such interaction mechanisms govern the fluorescence emission in these QDs as the fluorescing species appear not to be the major absorbers: bright fluorescence in visible is observed with an excitation far from major absorption transitions.

We observe fluorescence in visible and considerable emission features in the near-infrared (NIR) region from both N-GQDs/NS-GQDs measured via fluorescence spectrofluorimeter. In order to consider the emission contributed by π-π* and n-π* absorption transitions[117], excitation wavelengths ranging from 280 to 340 nm are utilized, showing multiple emission peaks (Figure 2.9a,b). As the excitation wavelength increases, these additional peaks get weaker/disappear indicating less fluorescence contribution from π-π* and n-π* transitions. Finally, starting from 330/340 nm excitation wavelength, one main broad fluorescence feature remains which is further explored in this work. This broad emission feature shows direct excitation dependence: scanning excitation from 350 to 475 nm allows to tune the emission in the visible from 425 to 531 nm for

N-GQDs (Figure 2.7a) and 448 to 539 nm for NS-GQDs (Figure 2.7c). Similar behavior is observed for NIR emission (Figure 2.7b,d) with excitation wavelengths ranging from 700 to 800 nm, inducing fluorescence ranging from ~800 to 890 nm (Figure 2.7b,d). Such excitation-dependent emission and intensity variation for both GQDs in the visible and near-IR region with the excitation wavelength indicates a presence of multiple sizes/types of emissive features or structures. Observed blue/green emission occurring with >330nm excitation is usually attributed to the confinement-induced band gap dictated by the size of the quantum dots [118] and thus the emission band is expected to vary with GQDs size. As excitation is shifted, different sizes are excited in resonance, therefore providing shifted emission with the possibility of exciting more species at higher excitation energies. As seen from the GQD size histogram, the size distribution is limited to the GQD diameters, potentially contributing to the emission in the visible. Larger structures would be expected to result in confinement-related NIR emission[119]. Thus it can be assumed that the excitation-dependent near-IR emission could potentially arise from different distribution/arrangements of emissive trap states [120, 121]. Such defect trap states can be associated with functional groups present in both N-GQDs/ NS-GQDs[120, 121]. Although in the process of thiourea-driven NS-GQDs synthesis, amino/thiol groups are expected to passivate the non-emissive trap states[122] on the surface to diminish the excitation dependent emission characteristics, the potential high local temperature produced by high power microwave treatment may prevent the surface passivation some functional groups may get unstable at higher temperatures leaving the surface of GQDs[122] with defects in their place. The distribution of these defects may therefore result in excitation-dependent emission observed for both N-GQDs/NS-GQDs in NIR. In both spectral regions GQDs show excellent photostability for several hours

without any signs of photobleaching. Under 365 nm 100 W UV illumination, a cyan-like, and blue fluorescence are also observed visually (Figure 2.7f) for N-GQDs and NS-GQDs, respectively, suggesting a high fluorescence efficiency.

Fluorescence quantum yield (QY) of N-GQDs/NS-GQDs is calculated using a comparative method [123] choosing Coumarin-153 and Fluorescein as two standard materials with excitation and emission wavelengths similar to the GQDs by using the following formula.

$$\phi_{GQDs} = \phi_{ref} \times \left(\frac{FLI_{GQDs}}{FLI_{ref}}\right) \times \left(\frac{1 - 10^{Abs_{ref}}}{1 - 10^{Abs_{GQDs}}}\right) \times \left(\frac{\eta_{GQDs}}{\eta_{ref}}\right)^2$$

In the above expression, Φref denotes the quantum yield of the reference materials, FLI represents integrated fluorescence intensity measured experimentally, Abs indicates the absorbance of materials at the excitation wavelength and η is denoted as the refractive index of the solvents. The refractive indexes of water, Coumarin-153, and Fluorescein are considered as 1.33, 1.36, and 1.33, respectively. Both standards show similar results with estimated QY ranging from 50 to 60% for N-GQDs and from 10 to 22% for NS-GQDs (Table-2.1a,b). The lower quantum yield of NS-GQDs, compared to N-GQDs, can be potentially caused by the additional non-radiative pathways introduced by sulfur dopants. Therefore, at the same concentration of both types of GQDs, NS-GQDs exhibit fluorescence with less peak intensity along with no significant difference in absorbance compared to N-GQDs resulting in lower quantum yield. The absolute quantum yield of N-GQDs was measured as 57±4% at 405 nm laser excitation showing good agreement with the values assessed via a comparative method.

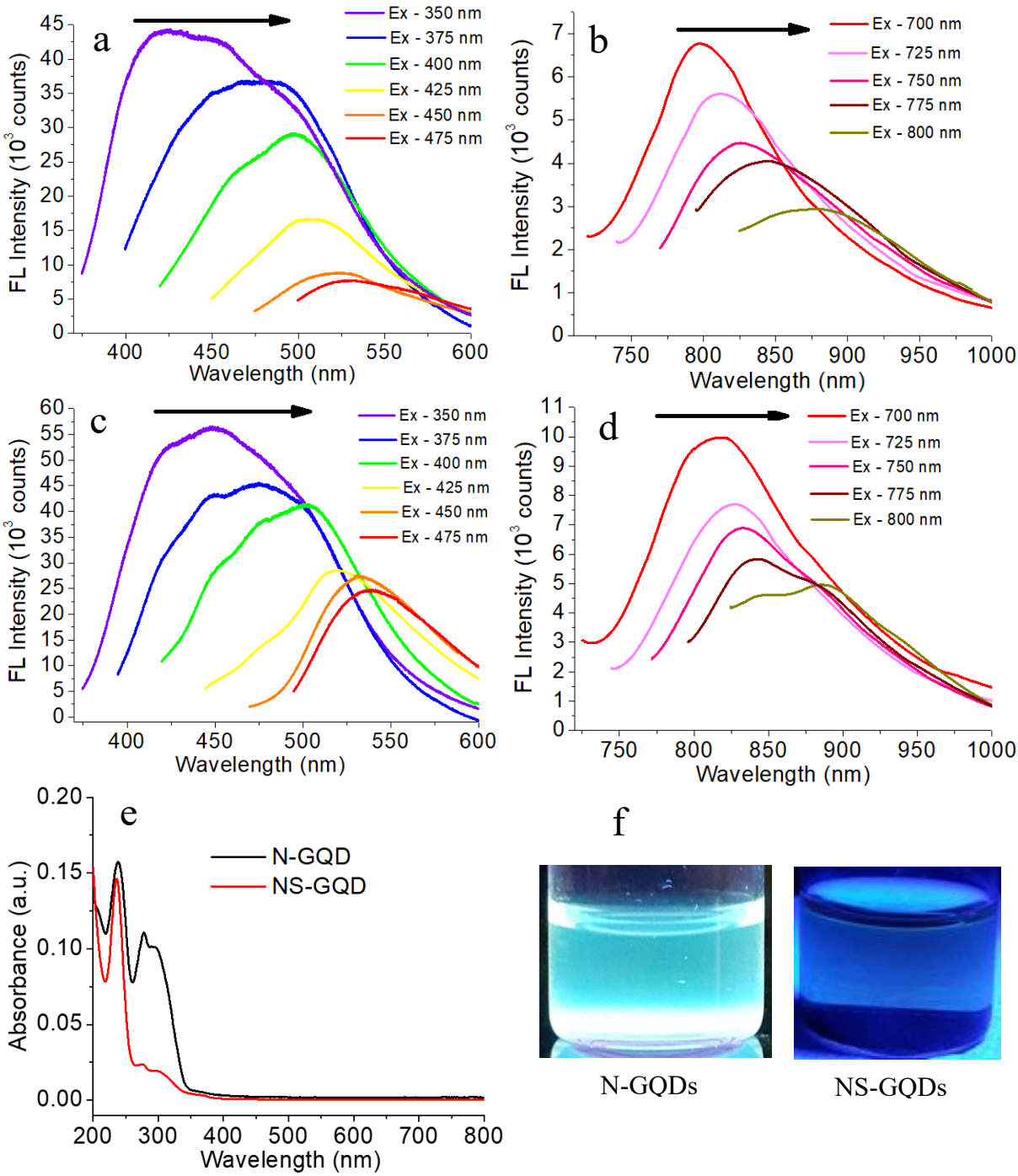

Figure 2.7: Excitation-dependent-emission in (a) visible, (b) NIR from N-GQDs and in (c) visible, (d) NIR from NS-GQDs. (e) Absorbance spectra of N-GQDs and NS-GQDs (f) Cyan and blue emission from the respective as prepared N-GQDs and NS-GQDs under the illumination of a 365 nm UV lamp.

Table-2.1: Quantum yield of N-GQDs and NS-GQDs

(a) Using Coumarin-153 as a reference material which has 47% quantum yield in ethanol at 400 nm excitation

Types of GQDs	Quantum Yield (%)
N-GQDs	60%
NS-GQDs	22%

(b) Using Fluorescein as a reference material which has 92% quantum yield in 0.1M NaOH at 360 nm excitation:

Types of GQDs	Quantum Yield (%)
N-GQDs	50%
NS-GQDs	10%

The absolute QY of N-GQDs measured further utilizing an integrating sphere at 405 nm excitation providing 57±4% absolute QY (Figure 2.8) which was calculated by using the following formula.

$$Quantum\ Yield = \frac{Area\ of\ Peak\ C}{Area\ of\ Peak\ A - Area\ of\ Peak\ B} \times 100\%$$

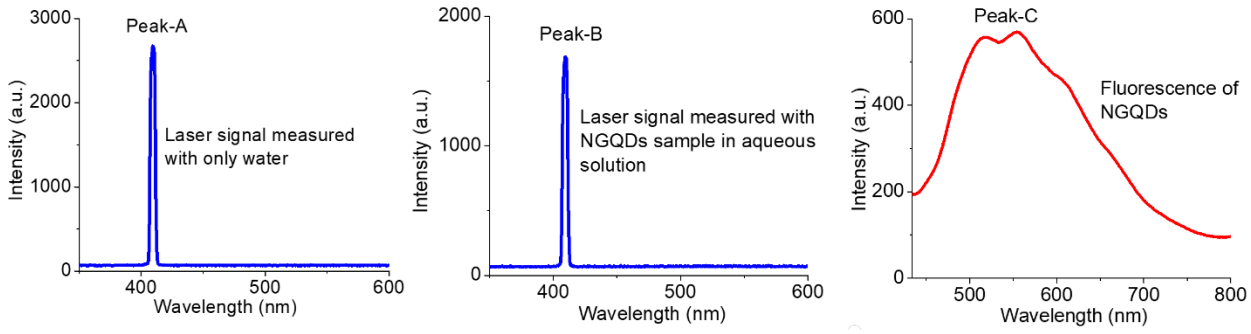

Figure 2.8: Utilizing an integrating sphere, (a) Signal measured with reference (water only); (b) Scattered signal from aqueous NGQDs sample; (c) Enhanced fluorescence emission with NGQDs at 405 nm laser excitation.

Substantial quantum yield and multicolor emission (green, blue, and near-infrared) observed from these QDs, suggest a great promise for optoelectronic and biomedical imaging applications.

We have also explored the routes to adjust the optical (photoluminescence) and structural (size) properties of these GQDs with a variation in microwave treatment time. N-GQDs/NS-GQDs synthesized with 20, 40, and 80 minutes of microwave treatment time show an increase in average NGQDs size from 3.60±0.13 to 9.70±0.40 nm (Figure 2.10) and NS-GQDs size from 2.30±0.07 to 5.02±0.14 nm (Figure 2.11). This size increase is complemented by a red-shift in visible emission band with more prolonged microwave treatment. The fluorescence intensity also increases with treatment time suggesting an increase in the concentration of GQDs confirmed qualitatively with TEM.

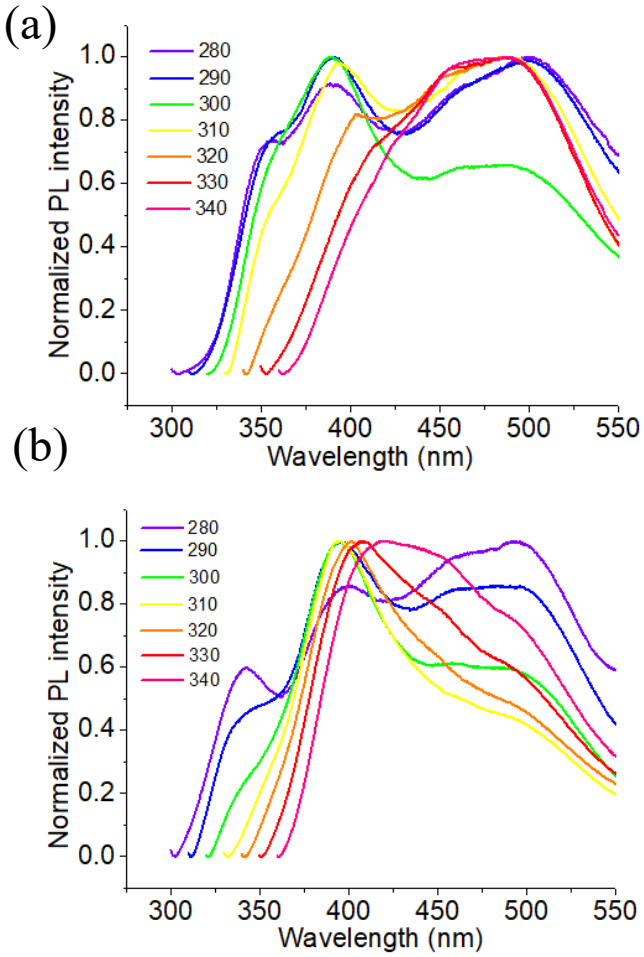

Figure 2.9: Emission spectra within the excitation range of 280-340 nm for (a) N-GQDs and (b) NS-GQDs

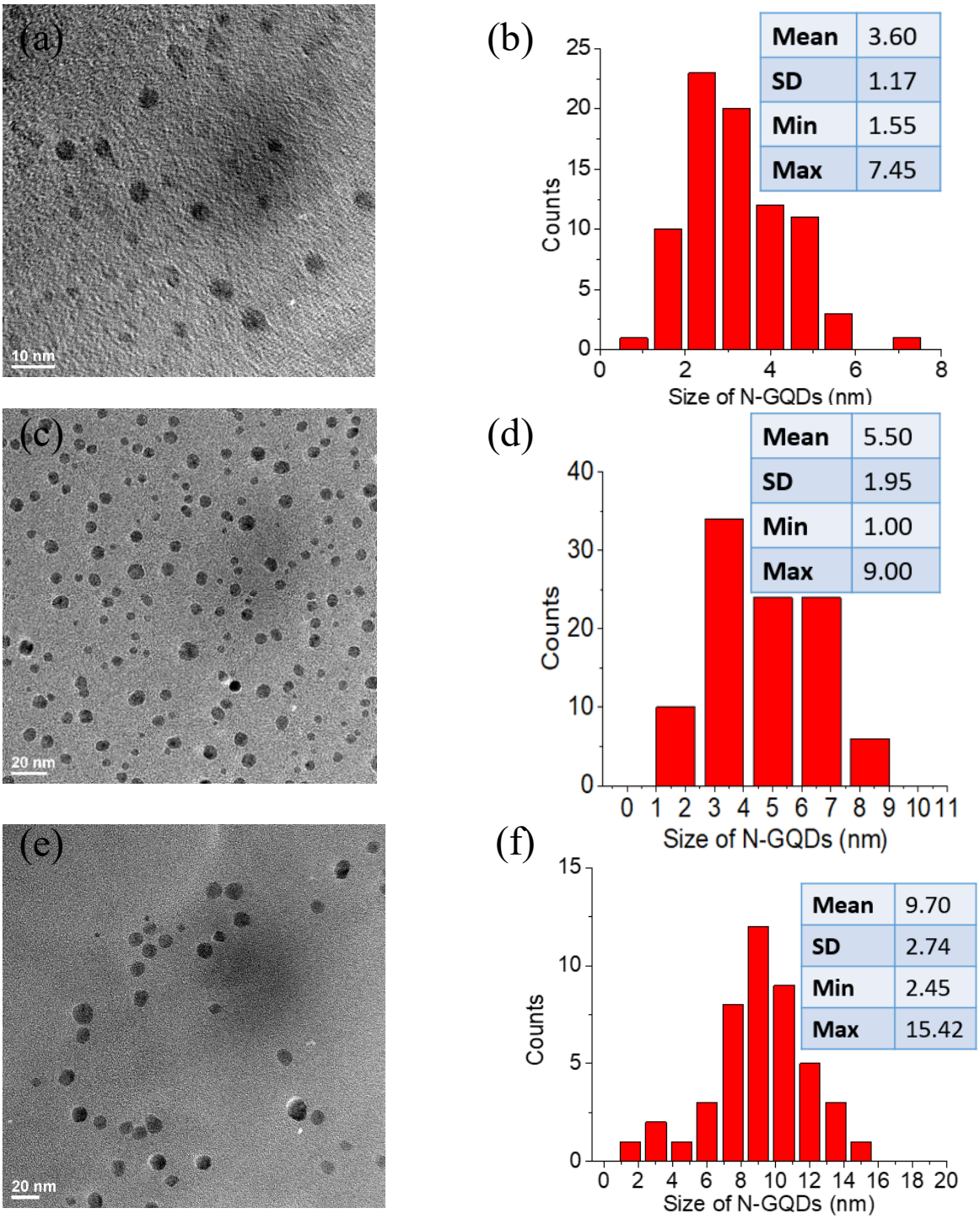

Figure 2.10: TEM images showing the distribution of (a) 20, (c) 40, (e) 80 min microwave treated N-GQDs. Statistics of the size distribution (in nm) of N-GQDs microwave treated with (b) 20, (d) 40, (f) 80 min. Inset: The mean, standard deviation, minimum, and maximum sizes of N-GQDs in nanometer.

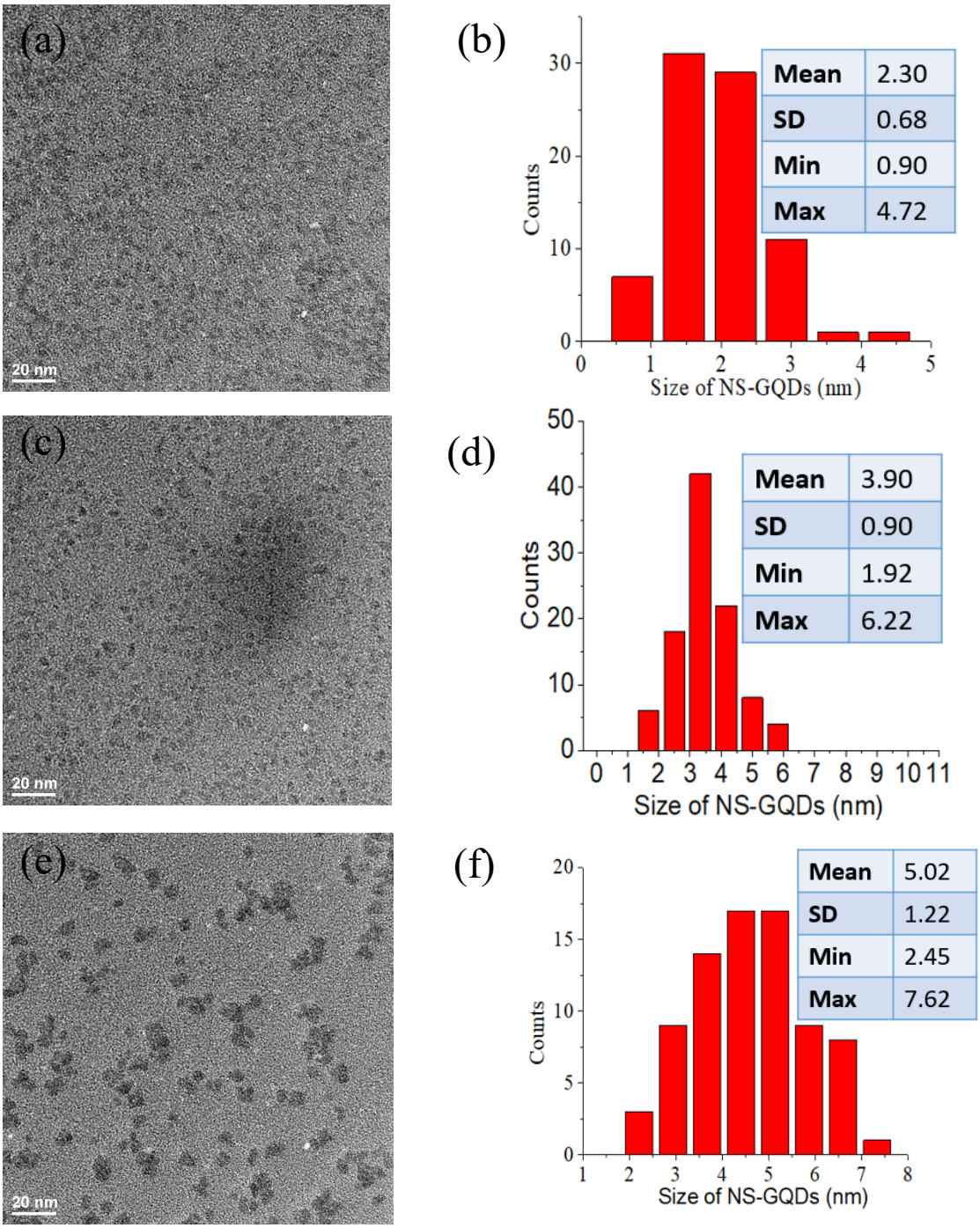

Figure 2.11: TEM images showing the distribution of (a) 20, (c) 40, (e) 80 min microwave treated NS-GQDs. Statistics of the size distribution (in nm) of NS-GQDs microwave treated with (b) 20, (d) 40, (f) 80 min. Inset: The mean, standard deviation, minimum and maximum sizes of NS-GQDs in nanometer.

Although the fluorescence peak maxima show considerable red-shift ~30 nm for N-GQDs (Figure 2.12a) and ~24 nm for NS-GQDs (Figure 2.12c) in the visible, no significant shift is detected in the NIR region (Figure 2.12b,d) for both GQDs. As GQDs exhibit size-dependent emission in the visible part of the electromagnetic spectrum, the redshifted peak maxima can be attributed to the increase in GQDs size with microwave treatment time. The insignificant change of NIR response suggests that NIR emission does not originate from quantum confinement-induced bandgap instead as suggested above potentially arising from the localized electronic environments influenced by the defect states at the functional groups that are unaffected by GQD size increase.

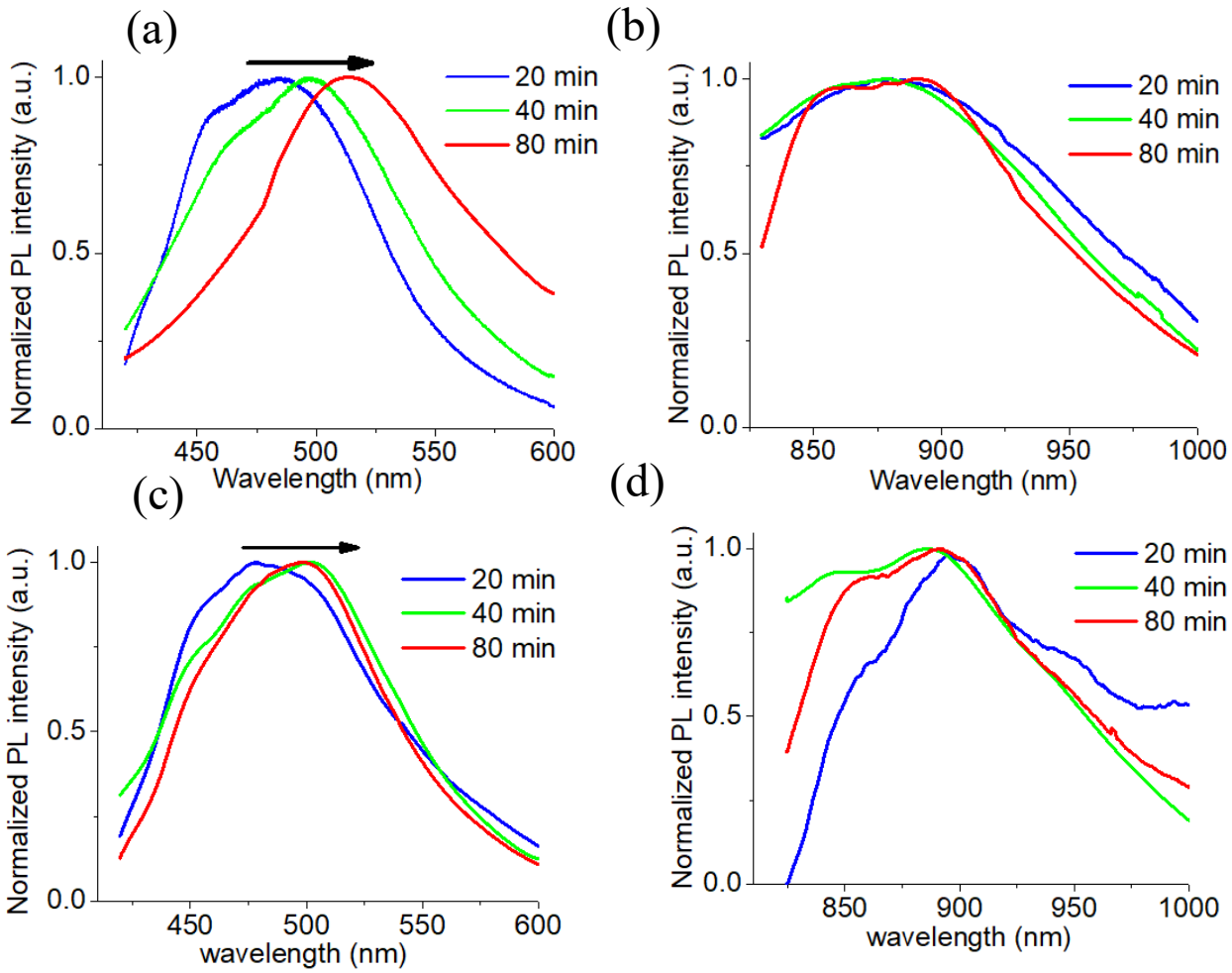

Figure 2.12: Fluorescence spectra of N-GQDs in (a) visible and (b) NIR and NS- GQDs in (c) visible (d) NIR region prepared with 20, 40, and 80 min microwave treatment time.

Besides changing microwave treatment time, the concentration of the initial dopant-containing precursor is also varied to find its potential effect on the GQD optical properties. As the synthesis of N-GQDs requires a single glucosamine precursor and nitrogen atoms get self-doped in the synthesis process, it is observed that with the increase of glucosamine precursor concentration, only the concentration of N-GQDs increases which leads to a higher emission intensity in visible/NIR without any significant shift in fluorescence maxima (Figure 2.13a,b). On the other hand, for the production of NS-GQDs, the initial concentration of thiourea precursor can be changed showing a decrease in visible emission intensity (Figure 2.13c), and on the contrary, an enhancement of NIR emission up to glucosamine/thiourea molar ratio of 1:1 (Figure 2.13d), while further it diminishes. However, with such variation of the precursor/dopant concentration, still no significant shifts in the emission maxima (visible and NIR) are observed. The decrease in emission intensity (visible) with the increase of sulfur dopant concentration can be potentially caused by the creation of more defect sites, which may introduce additional non-radiative pathways in NS-GQDs (Figure 2.13c) leading to lower quantum yield from NS-GQDs compared to N-GQDs. However, a higher number of defect states could lead to an increase in NIR emission potentially arising from those states (Figure 2.13d) competing with non-radiative quenching.

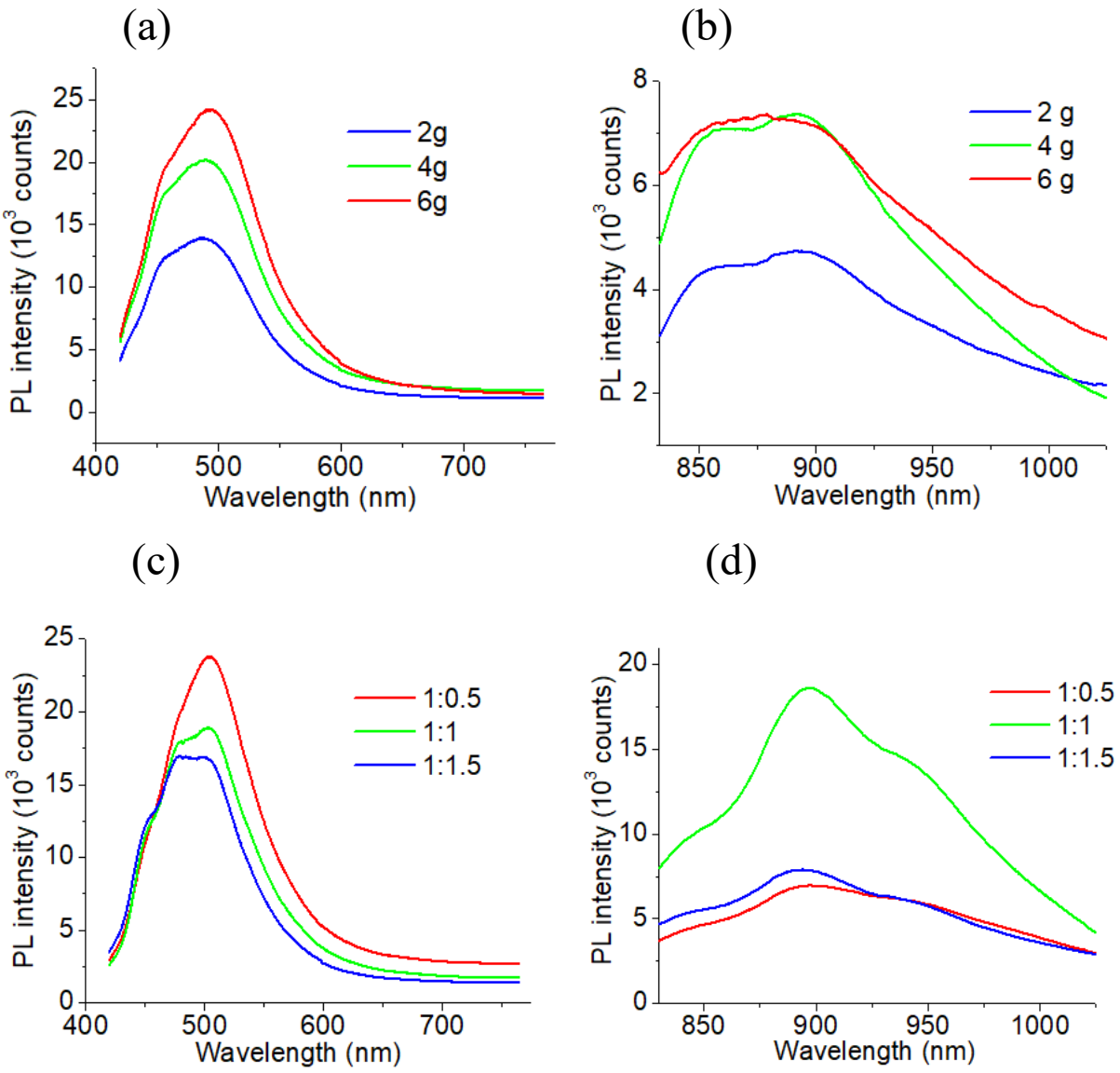

Figure 2.13: Fluorescence spectra of N-GQDs (a) in the visible and (b) NIR region with the change in precursor concentration from 2 to 6 g. Fluorescence spectra of NS-GQDs (c) in the visible and (d) NIR region with the variation in a precursor to dopant concentration from 1:0.5 to 1:1.5.

We fabricate light-emitting devices to explore the optoelectronic applications of NGQD using 150 nm Indium tin oxide (ITO)-coated glass as anode topped by a hole injection layer of poly(3,4-ethylene dioxythiophene):poly(styrene sulfonate) (abbreviated as PEDOT:PSS) with a thickness of 200 nm. On top of this, the active emissive dopant layer of N-GQDs is deposited via spin-coating. Finally, a silver-based cathode is used to complete the device geometry (Figure 2.14a) as a top layer. The multi-layered structure of this device is verified by a cross-section of the LED captured with the Scanning Electron Microscope (SEM) (Figure 2.15). The schematic of the energy band diagram of N-GQDs (Figure 2.14b) shows the feasibility of transporting electron and hole from one electrode to the other through the emissive NGQD layers. With the application of a particular bias voltage, holes can be injected from the PEDOT: PSS and electrons from the silver into the recombination layer consisting of N-GQDs.

As a result of this process in the experiment bright electroluminescence emission (inset of Figure 2.14c) is observed from the N-GQD-based device through transparent ITO electrodes. The electroluminescence spectra (Figure 2.14c) are measured by placing the device (ITO/PEDOT:PSS/N-GQDs/Ag) inside the spectrofluorometer at a fixed bias of 12V under ambient conditions. The same peak positions are observed in the EL spectra under liquid nitrogen (LN) at a fixed bias of 12V (Figure 2.14d) confirming that the nature of the observed transitions is electronic rather than thermal. Additionally, a separate measurement is performed to observe the photoluminescence emission from this device showing a number of peak maxima in PL spectra resemble those in EL spectra (Figure 2.14f) with minor to no spectral shifts between the two.

In this EL process, the holes in the HOMO (higher occupied molecular orbital) recombine with electrons in the LUMO (lower unoccupied molecular orbital) of the quantum dots. There are O, N, and S states in the LUMO that are related to π * orbitals of C=O, C=N, while the holes in HOMO are localized in the n orbitals of C=O, C=N and π orbitals in C=C[113]. The observed electroluminescence, therefore, originates from the electronic transitions between these states. Consistent with this mechanism, EL spectra of ITO/PEDOT: PSS/N-GQDs show four main peaks (Figure 2.14c) at 400 nm (3.09 eV), 441 nm (2.81 eV), 524 nm (2.37 eV) and 600 nm (2.07 eV). The peaks around 3 eV for ITO/PEDOT: PSS/N-GQDs correspond to the bandgap of PEDOT: PSS, while the other three main peaks at 2.81 eV, 2.37 eV, and 2.07 eV are then expected to correspond to the O and N states[113].

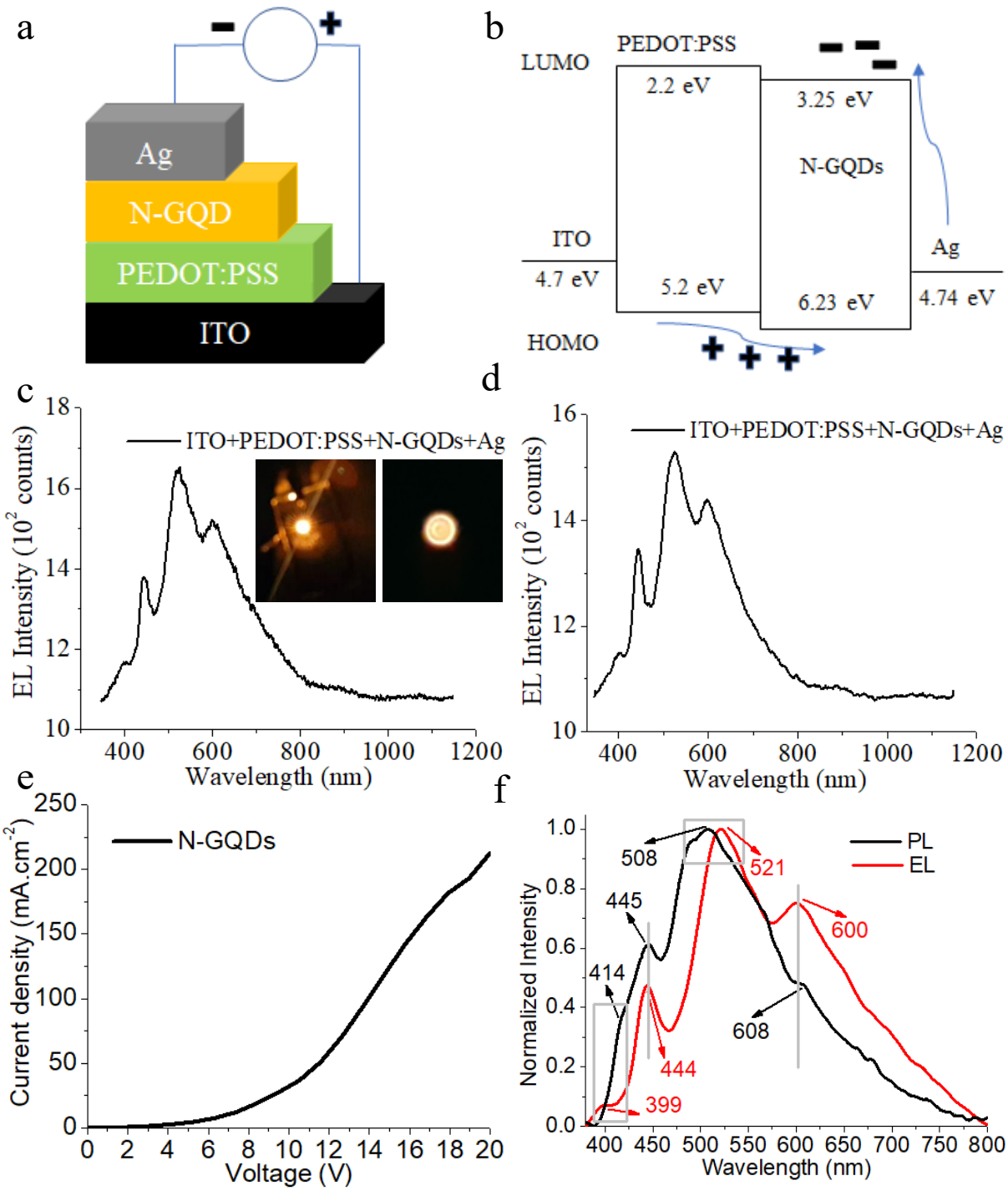

Figure 2.14: (a) Schematic and (b) Illustrative energy band diagram for N-GQDs based LED device. Electroluminescence response from N-GQDs based device under (c) room temperature (d) cryogenic temperature. (e) Current density-voltage (*J-V*) characteristics for the device fabricated with N-GQDs. (f) Comparison of Photoluminescence (PL) and Electroluminescence (EL) measurement spectra of LEDs fabricated with N-GQDs.

Here we consider 4.74 eV as the Fermi level of the GQDs based on the Kelvin Probe analysis reported by Kwon et al. [90] shown to be independent of QDs size for similarly-structured graphene quantum dots. Values of HOMO and LUMO are assessed with respect to the mid-gap Fermi energy and the bandgap size is calculated directly from fluorescence peak maxima of GQDs produced in this work. The devices are tested at different bias voltages showing a moderate turn-on voltage of ~ 7V (Figure 2.14e) with a variation in the EL peak intensity but no apparent spectral shifts. This work offers a new one-step/scalable/cost-effective synthesis of N-GQDs/NS-GQDs with visible/NIR emission for a variety of fluorescence applications and also presents a versatile, low-cost alternative for the fabrication of effective EL devices.

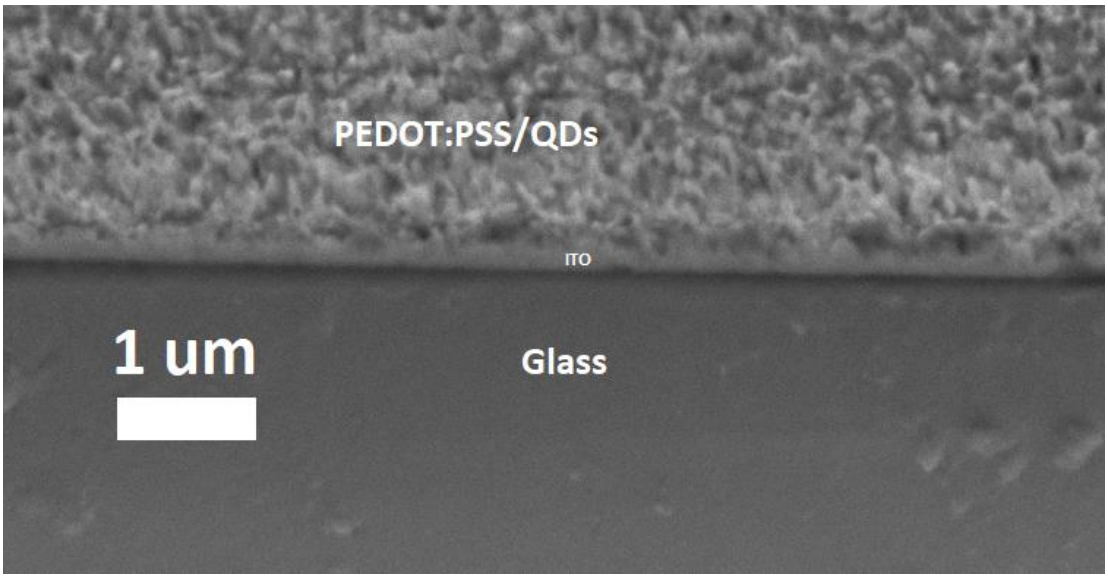

Figure 2.15: Cross-section SEM at 30° tilt of Glass/ITO/PEDOT:PSS/GQDs

2.4 Summary of chapter-2:

In this part of the work, we have for the first time synthesized novel nitrogen-doped graphene quantum dots (N-GQDs: average diameter size 5.5±0.19 nm) and nitrogen-sulfur co-doped graphene quantum dots (NS-GQDs: average diameter size ~3.9±0.09 nm) using an inexpensive single glucosamine precursor for N-GQDs and glucosamine/thiourea for NS-GQDs *via* a single-step microwave-facilitated hydrothermal method. These novel quantum dots are capable of forming stable water suspensions and exhibiting bright/stable fluorescence in the visible and near-infrared with high visible quantum yields of up to 60%. It has been proposed that excitation-dependent visible emission is governed by the QDs size-dependent band gaps induced by quantum confinement effects, whereas the near-IR emission can be potentially attributed to the functional groups-related trap states and their arrangements on GQDs surface. These quantum dots are further utilized as an active emissive layer due to their suitable energy level structure to successfully fabricate light-emitting devices showing bright electroluminescence in the visible. Considering their high quantum yield, the ability to emit photo- and electroluminescence and low-cost one-step preparation, N-GQDs/NS-GQDs produced in this work can be potentially used for biological imaging probes or, as shown in this work, as a basis for novel optoelectronic devices suitable for lower-cost production.

CHAPTER - 3

Nitrogen-doped Graphene Quantum Dots: Modification of Optical Properties and Photovoltaic Applications[124]

3.1 Overview

In this chapter, we focus further on the photovoltaic applications of N-GQDs. Solar cells fabricated with as-prepared N-GQDs as a photoactive layer show power conversion efficiency of ~0.41% along with moderate current density, open-circuit voltage, and fill factor. Although there are reports of devices prepared with other graphene quantum dots as photoactive layer[125-129], it is expected that alteration of the optical properties of as-prepared N-GQDs developed in our laboratory may significantly enhance their photovoltaic performance. A number of methods are utilized to date to modify the optical properties of GQDs including doping with potassium[130] or other heteroatoms (nitrogen, sulfur, boron, phosphorus), hydrazine-mediated reduction of graphene oxide quantum dots[131], band-gap modulation of GQDs *via* functionalization with amine groups [132], application of an external electric field[133], surface functionalization with carboxylic moieties[134], nitric acid-induced oxidation of graphene oxide[135], variation of temperature[136], redox processing[137] or photochemical fluorination[138]. However, all these methods require complicated design/set-up along with multi-step reaction phases. In our previous work, the optical properties of reduced graphene oxide (RGO) and graphene oxide (GO) were controllably modified in aqueous suspension using a simple in-situ ozone treatment [32, 118]. Here the same straightforward technique is utilized to alter the optical properties of as-prepared nitrogen-doped graphene

quantum dots in aqueous suspension. This is the first report of modifying optical properties of N-GQDs *via* ozone treatment to enhance the photovoltaic characteristics of GQDs-based solar cells. Additionally, thermal treatments are applied to provide the means for further adjustment of GQD optical properties.

With controlled ozone treatment, the amount of oxygen-containing functional groups on N-GQD surface increased in an efficient way which may potentially enhance charge transfer between TiO_2 and GQDs in a device state. This favorable mechanism is utilized in solar cell devices fabricated using the ozone-treated NGQDs (Oz-NGQDs) as a photoactive layer providing the best performance reported for this type of GQD solar cell configuration. Besides that, a one-step simple/scalable/cost-effective/eco-friendly synthesis process and organic structure of N-GQDs make them an advantageous alternative to existing counterparts utilized in solar cells.

3.2 Experimental Methods and procedures:

3.2.1 Synthesis/Characterization of N-GQDs and Oz-NGQDs:

The hydrothermal method which has been described in chapter 2 was used to prepare the N-GQDs utilizing a commercially available microwave (Hamilton Beach, model: HB-P90D23AP-ST) from an aqueous suspension of glucosamine-HCl (purchased from Sigma-Aldrich) at concentration of 0.14 M treated in the microwave for 60 min at 1350 W (Power level 3). As-prepared N-GQDs were purified utilizing MWCO (molecular-weight-cutoff) 0.5–1 kDa bag dialysis for 24h against DI water that was changed every after 6h. The purified NGQDs were further processed using an Enaly (Model: 5000BF-1) ozone generator fed by oxygen, producing ozone at a concentration of 0.3 gL^{-1} (10% of maximum ozone level -3 gL^{-1}). The N-GQDs were

subjected to ozone treatment in aqueous suspension over the periods of 0 to 65 min to produce ozone-oxidized N-GQDs. The morphological characterization of untreated N-GQDs and Oz-NGQDs was completed by Transmission Electron Microscopy (TEM JEOL JEM-2100). The samples for TEM characterization were prepared on the carbon-coated 200-mesh copper grid under ambient conditions. The optical characterization of N-GQDs/Oz-NGQDs samples was performed utilizing Horiba Scientific SPEX NanoLog Spectrofluorometer for measuring fluorescence with 400 nm excitation used previously[32] for visible emission, as well as 730/800 nm excitation for NIR emission and a Cary 60 UV-Vis (Agilent Technologies) absorption spectrometer for measuring the absorption within the range of 200 to 1000 nm. In order to eliminate the water content from the samples for the FTIR (Fourier transformed infrared spectroscopy) measurements, a Labconco, FreeZone 4.5 freeze-dryer was utilized to lyophilize purified N-GQDs/Oz-NGQDs. The functional groups on the untreated N-GQDs/Oz-NGQDs surface were further detected using the ATR (Attenuated total reflection) mode of the Thermo Nicolet Nexus 670 FTIR. The graphitic structure of untreated N-GQDs/Oz-NGQDs was further analyzed using a Raman spectrometer (DeltaNu) with 785 nm excitation at 100 mW maximum power and their topology – by tapping mode Atomic Force Microscopy (NT-MDT nanosolver AFM). The samples for Raman measurements as well as for AFM were prepared *via* spin-coating of aqueous suspension of N-GQDs/Oz-NGQDs on a silicon wafer at 1000 rpm.

3.2.2 Device fabrication:

The solar cells were fabricated using Fluorine doped tin oxide (FTO)-coated glass as a substrate. Before depositing other materials on the substrate, it was cleaned by 10% HCl for 1 hour

followed by an additional ultrasonication cleaning in acetone for 1 hour. After that, the FTO glass was blow-dried by nitrogen gas. In order to deposit a layer of TiO_2 (titanium dioxide) on the FTO glass substrate, TiO_2 was prepared from a solution containing titanium isopropoxide at 0.4 M in ethanol and 0.3 M of acetic acid which was spin-coated at 3000 rpm followed by baking at 500°C for two hours. We deposited 300 µl volume of 5 mg/ml aqueous suspension of NGQD by spin-coating at 3000 rpm for 20s followed by annealing at 120°C for one hour onto the FTO-TiO_2 film. To make electrical contacts, a conductive silver paste was deposited on top of the devices (each contact area is ~5 mm^2). The morphological characterization of the devices was carried out using a Field Emission Scanning Electron Microscope (JEOL-JSM-7100F) and the electrical/photovoltaic characterization of the devices was performed under one full sun illumination (solar simulator at one sun) using a Keithley 2420 Source Meter unit instrument.

3.3 Results and discussion:

In this work, we develop nitrogen self-doped GQDs (N-GQDs) using a straightforward synthetic route inside a commercially-available microwave oven from an aqueous glucosamine-HCl precursor. Glucosamine molecules dehydrate due to the hydrothermal reaction with continuous microwave treatment forming a chain of polymers and aromatic clusters. As the reaction time increases, condensation followed by carbonization along with self-doping of nitrogen takes place forming a limited range of well-distributed NGQD (Figure 3.1a). The size-distribution of untreated NGQD assessed by the TEM shows an average diameter of 6.01±0.22 nm considering over a hundred individual NGQD (Figure 3.1c). The HRTEM (high-resolution transmission electron microscope) images indicate the formation of carbon nuclei and crystalline lattice structure, which was verified by the FFT (fast-Fourier-transform) images (inset of Figure 3.1b) of

selected areas showing discernible lattice fringes with a lattice spacing of 0.21 nm (inset of Figure 3.1b) corresponding to the (100) plane of graphene[40].

These purified quantum dots are further processed by solution-processing ozone and thermal treatment to develop a technique for achieving optimized optical properties for photovoltaic applications. The aqueous NGQDs are subjected to the controlled ozone treatment for the periods of 0 to 65 min exhibit a substantial suspension color change from dark to light yellow with prolonged ozone exposure.

The crystallinity, size distribution, and morphology of ozone-treated NGQDs (Oz-NGQDs) characterized by HRTEM (Figure 3.1d) show significant changes including a decreased average size of 5.53±0.35 nm (Fig. 1(f)) for 16 min ozone-treated sample along with a less pronounced crystalline lattice structure (inset of Fig. 1(e)). This morphological change continues with the increase of ozone treatment time up to 65 min (maximum ozone treatment used in this study) which shows (Figure 3.1g,h,i) further substantial decrease in average GQD size down to 5.23±0.14 nm along with a higher degree of disorder in the graphitic structure.

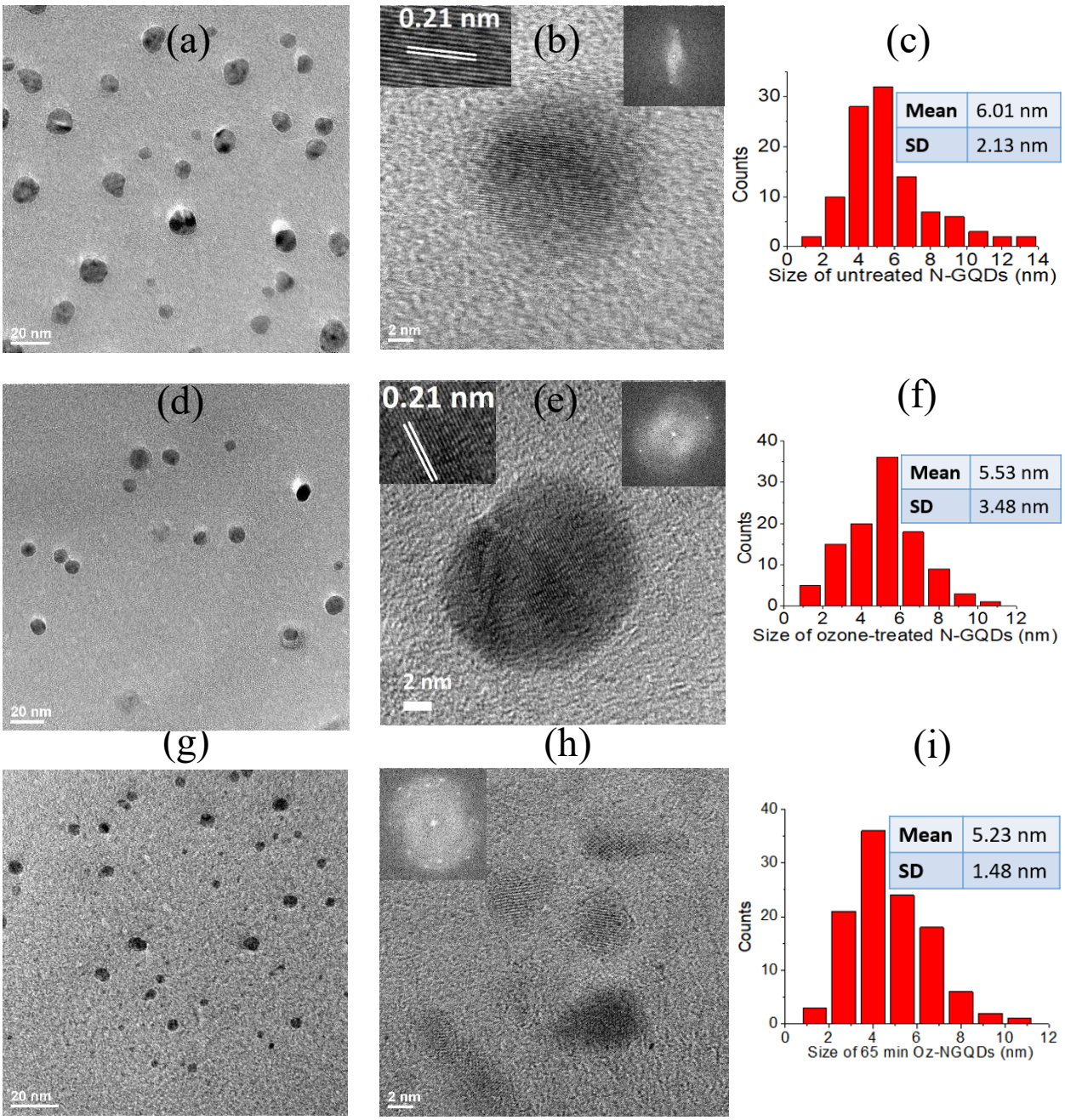

Figure 3.1: (a) TEM images showing the distribution of Un-NGQDS. (b) HRTEM images of Un-NGQDS. Inset: separation between lattice fringes (left side) and FFT images of the selected area (right side). (c) Size distribution of Un-NGQDs. (d) TEM images showing the distribution of 16 min Oz-NGQDS. (e) HRTEM images of 16 min Oz-NGQDS. Inset: separation between lattice fringes (left side) and FFT images of the selected area (right side). (f) Size distribution of 16 min Oz-NGQDs. (g) TEM images showing the distribution of 65 min Oz-NGQDS. (h) HRTEM images of 65 min Oz-NGQDS. Inset: FFT images of the selected area (left side). (i) Size distribution of 65 min Oz-NGQDs.

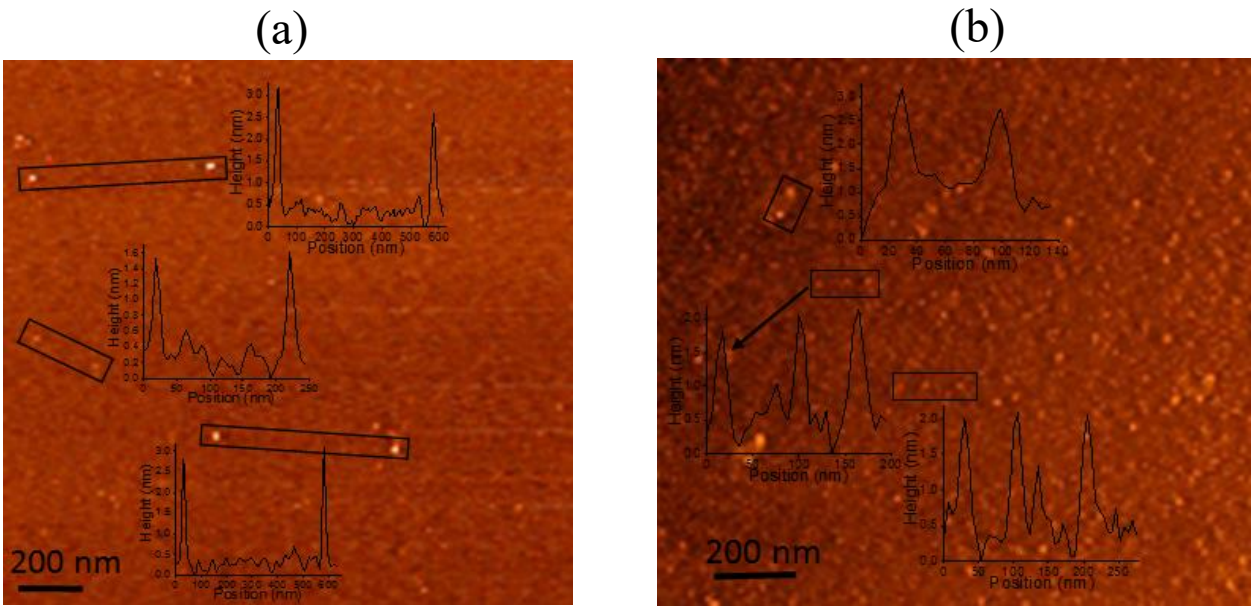

Figure 3.2: AFM height profiles for (a) Un-NGQDs and (b) Oz-NGQDs

The decrease in average GQD size along with narrower size distribution range suggests the scission of N-GQDs and a change in crystallinity/shape of GQDs compared to the untreated NGQDs indicates the introduction of defects induced by prolonged ozone-oxidation. Although ozone treatment introduces a change in the lateral dimension of N-GQDs, the height profile analysis performed *via* AFM shows similar thickness (up to ~3 nm) for both NGQDs (Figure 3.2a) and Oz-NGQDs (Figure 3.2b) indicating that quantum dots still possess multi-layered (potentially spherical-shaped) structure. As HRTEM images show change in average size, lateral dimension, lattice structure with timed ozone treatment, it is expected to observe potential changes in type and abundance of particular functional groups, which is later verified by FTIR (Fourier-transform infrared spectroscopy) measurements.

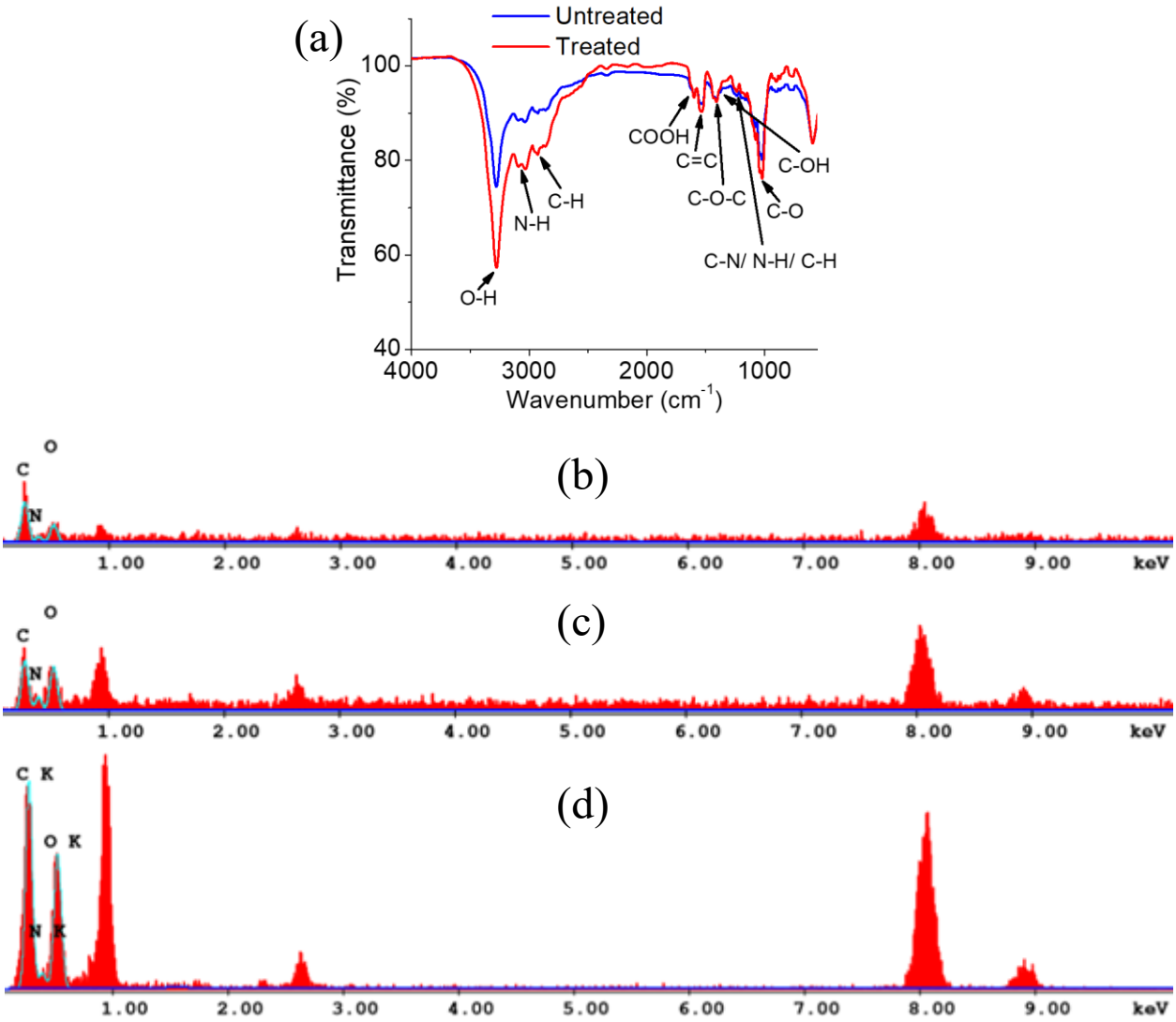

(e)

Element name (Shell)	Untreated NGQDs (Wt%)	16 min Ozone-treated NGQDs (Wt%)	65 min Ozone-treated NGQDs (Wt%)	Untreated NGQDs (At%)	16 min Ozone-treated NGQDs (At%)	65 min Ozone-treated NGQDs (At%)
C(K)	83.37	75.91	68.12	86.10	79.85	73.56
N(K)	9.18	10.05	5.28	8.13	9.06	4.88
O(K)	7.45	14.04	26.60	5.77	11.09	21.56

Figure 3.3: FTIR spectra of (a) untreated and 16 min ozone-treated NGQDs. EDX spectra of (b) untreated, (c) 16 min ozone-treated, (d) 65 min ozone-treated NGQDs (d) Table of elemental weight and atomic percentages of untreated, 16 min ozone-treated, and 65 min ozone treated NGQDs.

Ozone treatment introduces a distinct increase in absorbance for the vibrational transitions of O-H groups centered at 3275 cm^{-1} (Figure 3.3a), suggesting the introduction of hydroxyl groups. The stretching vibrations of C-H, C=O of COOH, C=C, C-O-C peaking at 2935, 1602, 1530, and 1412 cm^{-1} (Figure 3.3a), also show a slight increase of intensity for Oz-NGQDs. However, no significant intensity change is observed for the bands at 1240 cm^{-1} corresponding to the stretching vibrations of C-N/N-H and with only a moderate variation of C-O transition at 1021 cm^{-1} (Figure 3.3a)[85, 111]. These functional group-dependent characteristic changes of vibrational transitions are further supported by EDX (Energy dispersive x-ray spectroscopy) measurements which show a significant increase in oxygen and a very moderate decrease in carbon/nitrogen atoms (atomic percentage) (Figure 3.3b,c,d,e) verifying the addition of oxygen-containing functional groups in NGQD surface detected by FTIR. A change in the intensities of D and G bands observed *via* Raman measurements and a much higher I_D/I_G ratio (0.99) for Oz-NGQDs (Figure 3.4b) than for Un-NGQDs (I_D/I_G=0.7) (Figure 3.4a) suggests the introduction of defects during ozone-oxidation. It is evident from the FTIR, EDX, and Raman data that timed ozone treatment introduces/transforms oxygen/nitrogen-containing functional groups. Based on this concept, a qualitative schematic (Figure 3.5) is envisioned reflecting ozone-induced structural and functional group changes observed at 16 min treatment followed by the next step of 65 min deteriorative over-oxidation.

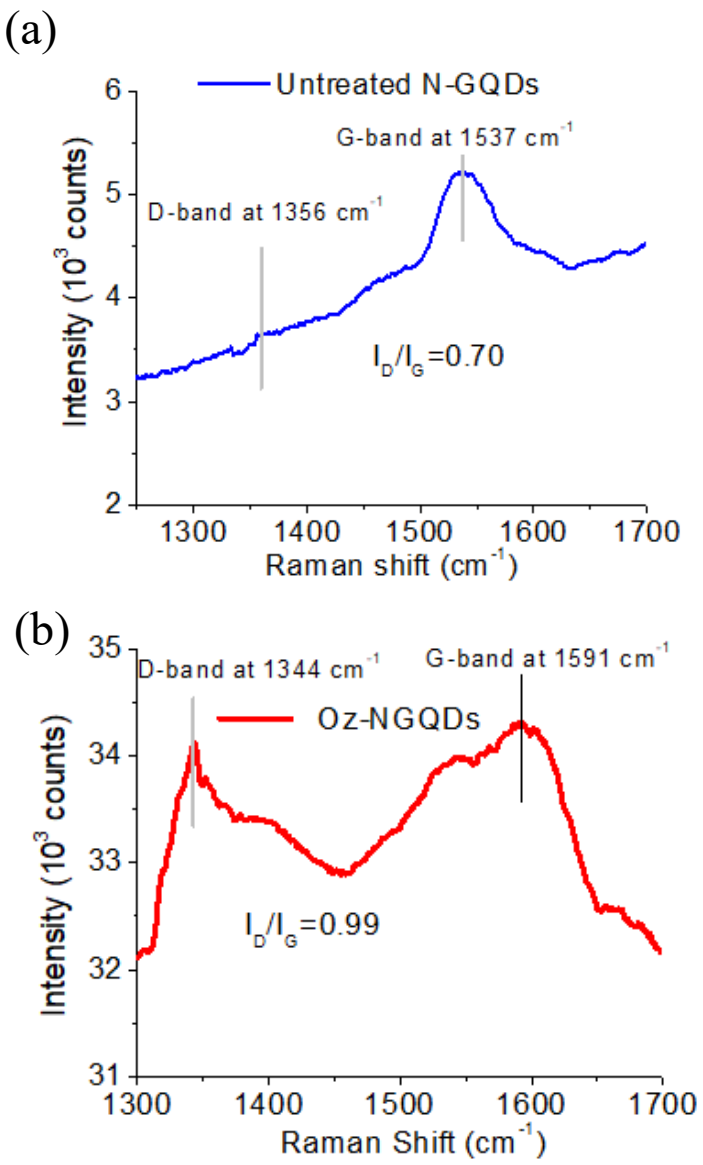

Figure 3.4 Raman spectra of (a) untreated NGQDs and (b) Ozone treated NGQDs.

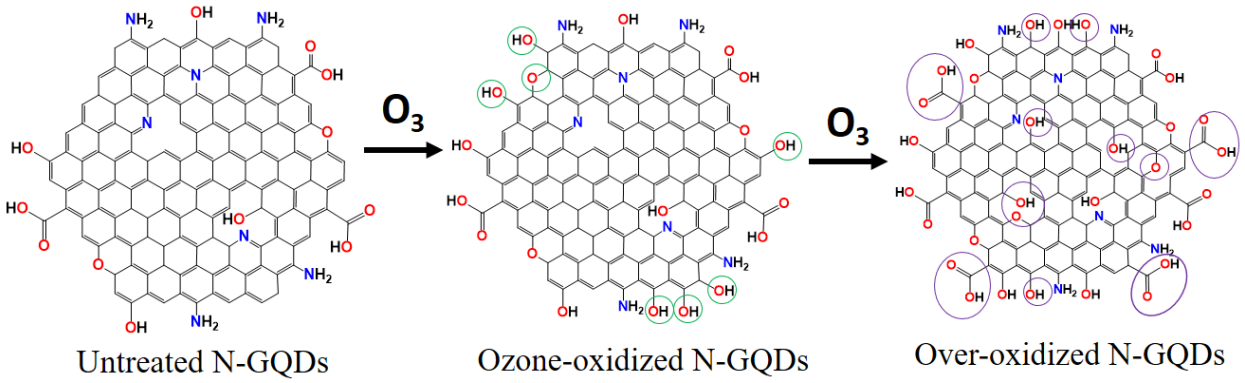

Figure 3.5: A schematic of untreated NGQDs chemical structure and their change due to ozone-induction and over-oxidization. Green circles denote the introduction of new functional groups during the ozone-oxidization step whereas purple colored circles highlight functional groups transformed due to over-oxidation.

It is also apparent that the color of NGQD suspension changes from dark to light yellow (more transparent) with prolonged ozone treatment (Figure 3.6b) due to the considerable variations in its UV-visible absorption. We observe two absorption peaks at 239 and 283 nm (Figure 3.6a) corresponding to the π-π* and n-π* electronic transitions of C=C and C=O[115] and a shoulder at ~317 nm (Figure 3.6a) ascribed to the π-π* transition of C=N[116] for untreated NGQDs. With timed ozone treatment, the absorption peaks at 239, 283 and 317 nm decrease substantially (by the factors of ~9.9, ~2.5, and ~10 respectively after 65 min ozone treatment) suggesting a significant alteration in dominant absorbing species along with the disappearance of absorption features for 239 nm peak indicating modification/deterioration of the GQDs graphitic structure. Additionally, prolonged ozone-oxidation induces ~8 nm blue shift of the 283 nm peak spectral feature suggesting the increased electronegativity from additional oxygen atoms with the introduction of new functionalities. No significant absorption is observed for untreated NGQDs or Oz-NGQDs within the range of 350-950 nm (Figure 3.7) at the same concentrations.

Although a change in color is observed upon ozone treatment under daylight condition, no apparent color change is seen with the naked eye under UV illumination as both untreated NGQDs and Oz-NGQDs retain their usual cyan like emission (Figure 3.6b). Similarly to absorption spectral features, we observe a significant change in the fluorescence upon ozonolysis. An excitation-dependent visible and NIR emission is observed from untreated NGQDs which has been studied thoroughly in the previous chapter[46]. With timed ozone treatment for the periods of 0-16 min at an ozone concentration of 0.3 g l^{-1}, the fluorescence intensity increases along with a slight blue shift of ~6 nm (Figure 3.6c,d) suggesting potential transformation/rearrangement of some oxygen-containing functional groups into the emissive species indicated by the FTIR/absorbance measurements. Also, the slight blue shift can be potentially originated from the decrease of average GQD diameter with prolonged ozone exposure as detected by TEM, since GQD optical bandgap is inversely proportional to their size[118]. However, with further ozone processing (more than 16 min ozone treatment), the fluorescence emission starts to show irreversible quenching (Figure 3.6c,d) potentially due to the introduction of charge traps which is considered as destructive over-oxidation[32]. It is observed that a slight increase in ozone concentration or treatment time may over-oxidize the NGQDs resulting in a significant change in optical/structural properties. Therefore, it is imperative to have control over ozone concentration to obtain optimized visible emission intensity. Unlike the decreased emission intensity in the visible region exhibited by over 16 min-treated Oz-NGQDs, the NIR emission intensity continues to increase up to 45 min treatment followed by intensity drop for over 45 min treatment (Figure 3.6e,f).

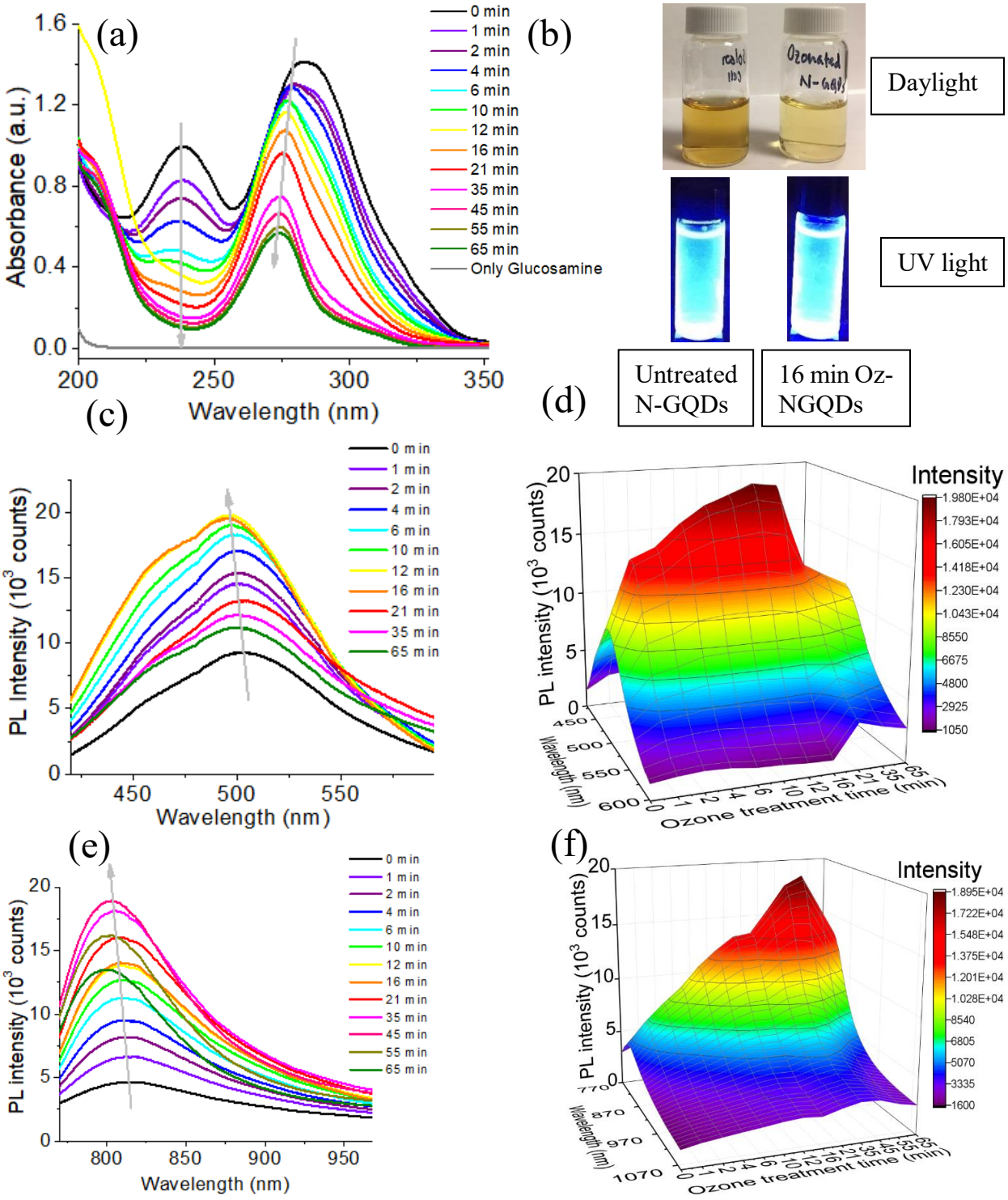

Figure 3.6: (a) Absorbance of 0 to 65 min ozone-treated NGQDs over the scanning range of 200 to 352 nm. (b) Physical color of untreated and 16 min ozone-treated NGQDs under the daylight and irradiation of a 365 nm UV lamp. Emission of 0 to 65 min ozone-treated NGQDs in (c) visible region at 400 nm excitation and (d) a corresponding 3-D plot. (e) Emission in NIR region at 730 nm excitation and (f) a corresponding 3-D plot.

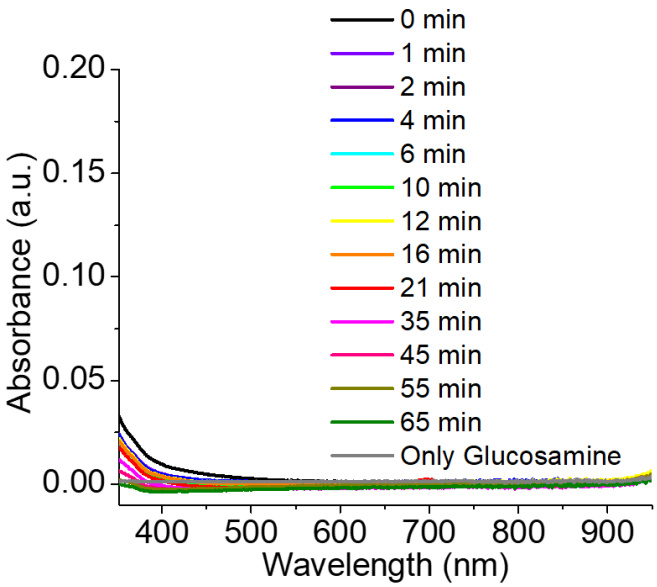

Figure 3.7 Absorbance of 0 to 65 min ozone-treated NGQDs over the scanning range of 352 to 950 nm.

Since the NIR emission was thought to be defect state-related as described in Chapter 2[46], the increase of NIR emission intensity can be ex by the creation of additional defects in GQDs surface through oxygen functionalities with prolonged ozone-oxidation which is verified by the FTIR/EDX/Raman studies. We can further suggest that with over 45 min ozone treatment, over-oxidation may take place, which can transform the NIR-emissive defect states into non-emissive species which may result in the observed further decrease in the emission intensity (Figure 3.6f).

The optical properties of NGQDs can also be controllably altered using stepwise thermal treatment leading to irreversible monotonic fluorescence quenching in the visible and NIR with a variation of temperature from 27 to 90°C (Figure 3.8a,b). Similarly to graphene oxide[32], this fluorescence quenching can be caused by the thermal reduction of oxygen-containing functional groups. The ability to controllably enhance or diminish fluorescence intensity either by ozone or

thermal treatment ensures the adjustment of NGQD optical response for potential optoelectronic applications.

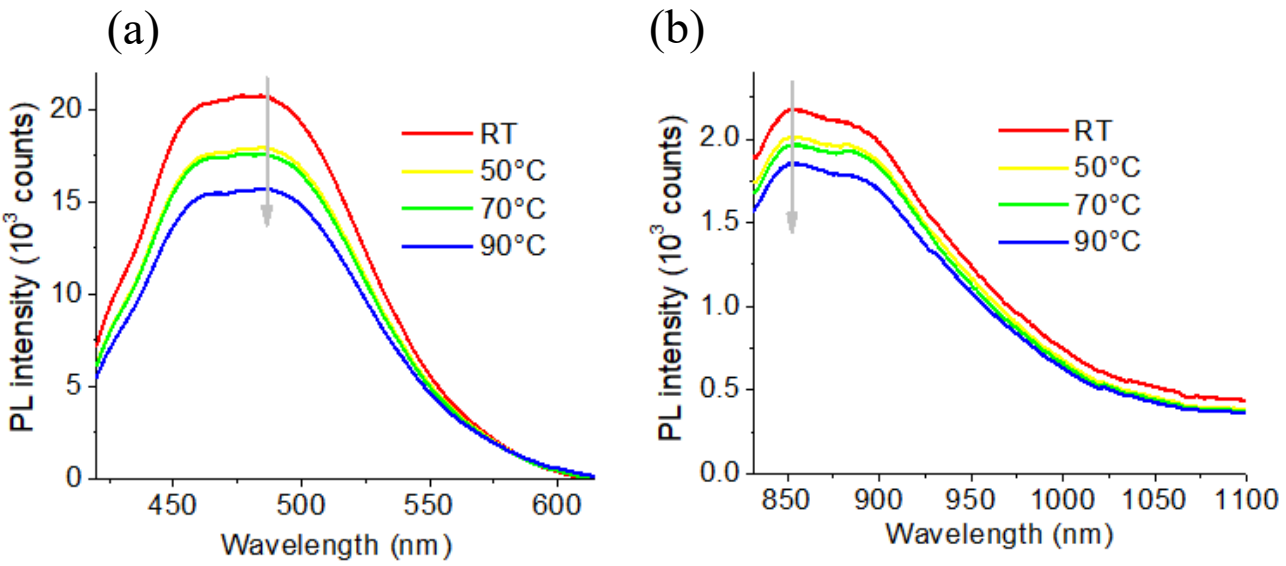

Figure 3.8: Emission of RT (room temperature) to 90°C temperature-treated NGQDs in (a) visible region at 400 nm excitation, (b) NIR region at 800 nm excitation.

The N-GQDs with optical properties optimized *via* controlled ozone treatment are further utilized as a photoactive layer for the fabrication of solar cells. As maximum visible emission intensity is observed for 16 min Oz-NGQDs followed by overoxidation, resulting in structural deterioration for more than 16 min ozone-treated N-GQDs, we consider 16 min-treated material as most suitable for an optimal emission-enhancement for NGQDs-based devices. Less oxidized and thermally reduced NGQDs are also utilized as an active layer to produce solar cells yielding lower photovoltaic performances similar to those of untreated NGQDs. Thus here we compare the devices developed with optimally (16 min) ozone-treated GQDs and untreated NGQDs.

Untreated and ozone-treated NGQDs are utilized further as a photoactive material to fabricate several prototypes of solar cell devices. In order to fabricate the device, we use a glass substrate

coated with fluorine-doped tin oxide (FTO) as an anode topped with TiO_2 (Titanium dioxide) layer and a layer of untreated-NGQDs or Oz-NGQDs deposited onto FTO/TiO_2 *via* spin-coating, and, finally, a conductive silver (Ag) paste contact as a cathode (Figure 3.9a). A multi-layered structure of the device is observed by the cross-sectional image (Figure 3.9b) captured by FESEM (field-emission scanning electron microscope) showing 150 nm FTO-coating, 100 nm-thick layer of TiO_2 followed by 45 nm of NGQDs or Oz-NGQDs, and a silver electrode. A schematic of the corresponding energy band diagram of the solar cell is shown in Figure 3.9c by taking into account the known value for the work function of FTO(anode)/Ag(cathode) and the predicted Fermi level of the GQDs[46] of similar type. The Fermi level of the GQDs assessed by Kwon et al.[90] *via* Kelvin probe analysis as 4.74 eV irrespective of GQDs sizes is utilized as a reference, while the values of HOMO and LUMO are calculated from the emission peak maxima. As a slight blue shift (~5 nm) in emission peak maxima is observed with prolonged ozone treatment, no significant changes in the optical band gap are expected. In this device NGQDs absorb photons in the visible region under AM (air mass) 1.5 G (global) at one full sun illumination generating photoinduced electrons and holes leading to electron migration to the TiO_2 film and then transfer to FTO, while the holes move toward the cathode.

Solar cells fabricated with untreated NGQDs as a photoactive layer provide J_{sc} (short circuit current density) of ~1.3 mA/cm^2, V_{oc} (open circuit voltage) of ~0.56 V, FF (fill factor) of 27.8 %, and PCE (power conversion efficiency) of 0.41 % (Figure 3.9e) which is comparable to the photovoltaic performances of the solar cells fabricated with GQDs as active layer reported previously[139-141]. However, solar cells made with ozone-treated NGQDs exhibit a significant boost in photovoltaic parameters including average J_{sc} ~2.0 mA/cm^2, V_{oc} ~ 0.83 V, FF ~86.40%

and PCE ~1.44 % (Figure 3.9f). This enhancement in photovoltaic performance with Oz-NGQDs-based devices can be correlated with higher intensity and broader range of visible absorption of the device with Oz-NGQDs as compared to such with untreated NGQDs (Figure 3.9d). Also, it is apparent that there is an additional absorption feature at 431 nm and a shoulder at 537 nm for the Oz-NGQD device, which could be either attributed to the red-shifted 407 and 485 nm peaks of TiO_2, or new absorbance features appearing due to the charge transfer between oxygen functionalities introduced to NGQDs by ozone treatment and TiO_2.

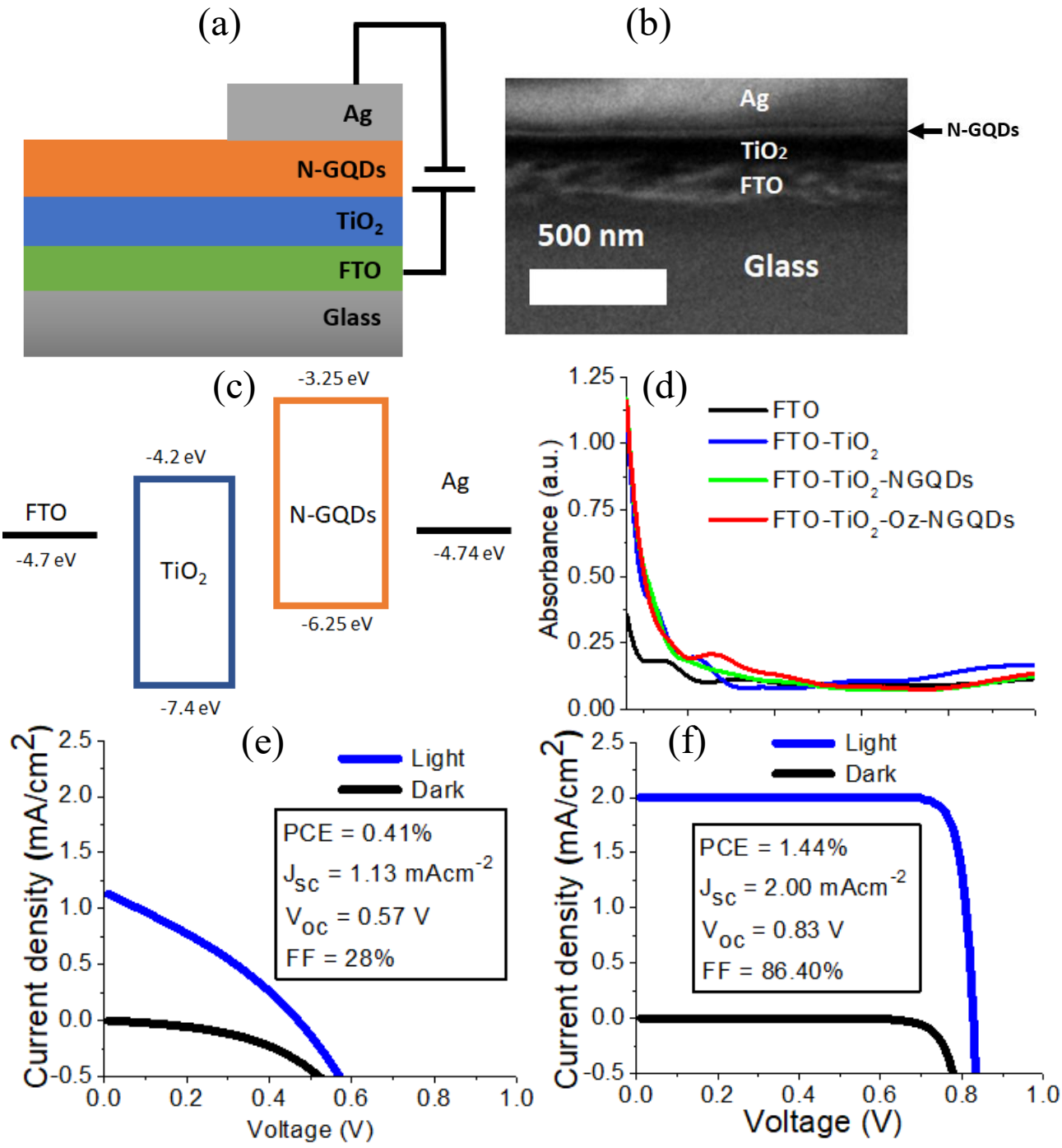

Figure 3.9: (a) Schematic of solar cell device structure, (b) Cross-section of solar cell captured by FESEM, (c) Band energy diagram of solar cell, (d) Layer by layer absorbance of the solar cell device. J_{sc}-V curve of solar cells fabricated with (e) Un-NGQDs and (f) Oz-NGQDs.

A box and whisker plot (Figure 3.10a,b) is used to describe the range of PCE (power conversion efficiency) parameter distribution of multiple solar cells fabricated with untreated and ozone-treated N-GQDs. Among all the fabricated devices, a maximum power conversion efficiency of 2.64% and a short circuit current density of 4.8 mA/cm^2 are obtained (Figure 3.10c) with a lower open-circuit voltage of ~0.65V and a fill factor of ~83.4% from the same solar cell, while the average PCE recorded considering all Oz-NGQDs-based devices is 1.36%.

Although much higher PCE can be achieved with dye-sensitized solar cells (DSCs) containing transition metal (ruthenium-based dyes) as sensitizers[142], or PbS[143]/CdS/CdSe[144] (Lead-Sulfide/Cadmium-Sulfide/Cadmium-Selenide) core-shell QD-based solar cells, their toxicity leading to potential environmental hazard/detrimental effects on the climate[145, 146] and complex fabrication process hamper the long-term practical use of these materials. On the other hand, organic structure and simple/scalable synthesis process of N-GQDs from a single low-cost bio-safe starting material shown in this work provide an eco-friendly alternative for the fabrication of solar cells. Unquestionably, the state of the art silicon[147] and GaAs-based[148] solar cells can also provide higher efficiencies; however, this work suggests that the photovoltaic performances of such and/or other solar cell models can be enhanced using ozone-treated NGQDs as a photoactive layer.

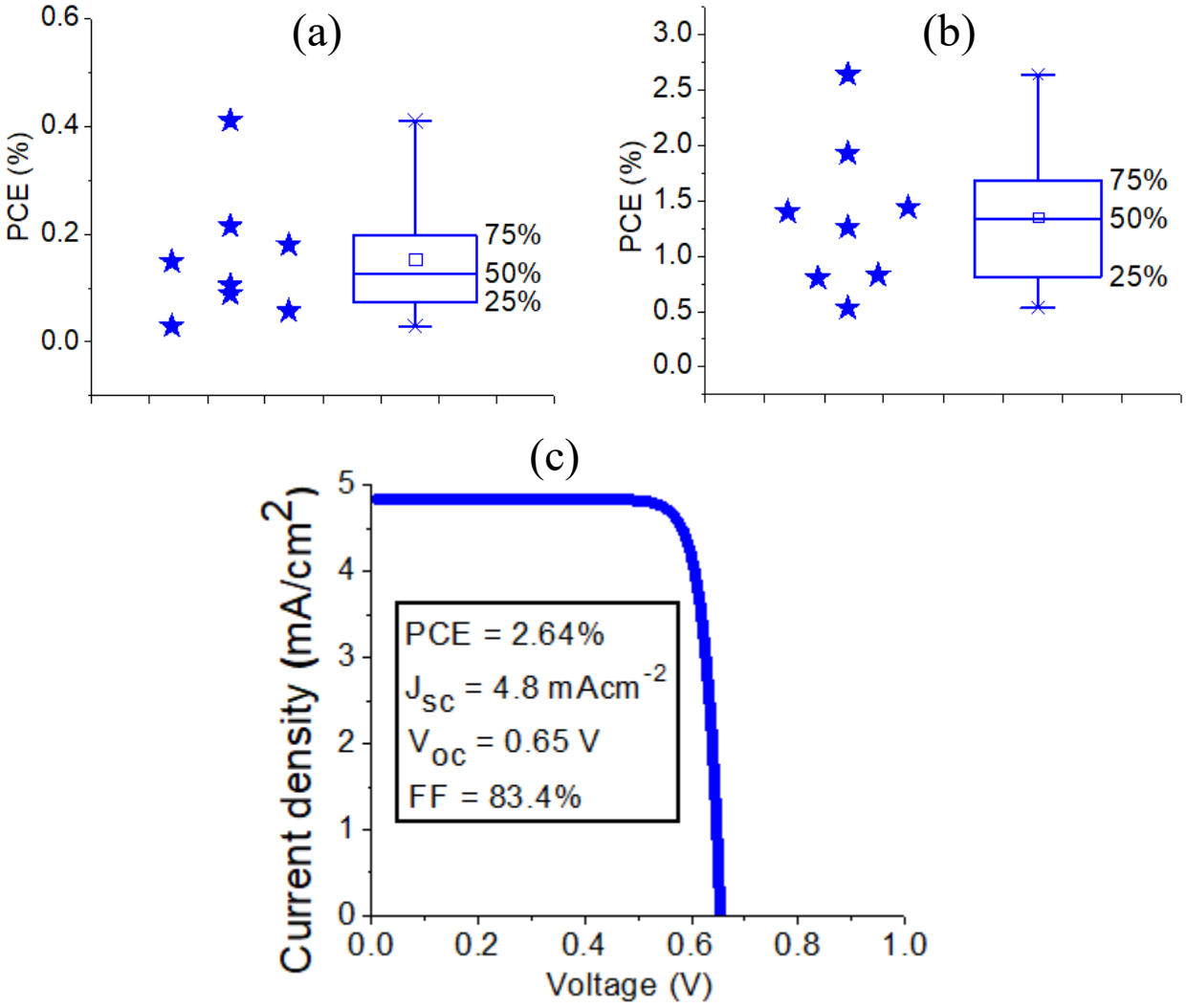

Figure 3.10: Box and Whisker plot of PCE distribution of a number of solar cells fabricated with (a) Un-NGQDs (b) 16 min-treated Oz-NGQDs. (c) J_{sc}-V plot of one solar cell showing maximum PCE of 2.64% and J_{sc} of 4.8 mA/cm^2 but with a lower V_{oc} of 0.65V and FF of 83.4% as compared to others.

3.4 Summary of chapter-3:

Nitrogen self-doped graphene quantum dots exhibiting bright/stable visible/NIR emission are synthesized *via* a simple, scalable, cost-effective, and eco-friendly method from a widely available single glucosamine precursor. As-prepared N-GQDs (6.01±0.22 nm average size) are modified further by controlled ozone/thermal treatment showing a significant alteration of their optical and structural properties suitable for solar cell applications. N-GQD emission increases with prolonged ozone treatment due to the introduction/rearrangement of oxygen-containing functional groups in N-GQDs on their surface, whereas thermal treatment, a reverse process, serves as a controllable avenue to decrease GQD emission via anticipated reduction of those functionalities. Oxidative ozone treatment results in the decrease of GQD average size down to 5.23±0.14 nm and a more disordered structure due to the introduction of the new functional groups detected by FTIR and ultimately leading to a slight deterioration of the carbon platform. The EDX measurements support the FTIR results by showing a significant increase in the atomic and the weight percentage of oxygen atoms. Besides this alteration of structural characteristics, ozone treatment also induces significant modification to NGQD optical properties showing a gradual decrease of the absorption peak intensity with treatment time and enhancement of the visible fluorescence intensity up to 16 min treatment followed by further intensity drop-off due to the overoxidation-induced non-radiative defect centers. On the contrary, the NIR emission potentially associated with defect states increases noticeably up to 45 min and only after extensive overoxidation decreases. These ozone treatment-induced variations allow fabrication of multiple Oz-NGQDs-based solar cells with superior photovoltaic performances as compared to the untreated NGQDs. We achieve PCE ~2.64%, V_{oc} ~0.83V, J_{sc} ~4.8 mA/cm^2, and 86.4% fill factor from Oz-NGQDs devices providing

>6 times enhancement in PCE and >3 times increase in fill factor/current density with respect to the devices fabricated with untreated N-GQDs and other GQD devices under AM 1.5 G one full sun illumination. This work suggests that ozone treatment is a simple yet versatile technique to modify the optoelectronic properties of scalably synthesized N-GQDs that can be successfully utilized to boost the photovoltaic performance of solar cells.

CHAPTER - 4

Variation of Optical Properties of Nitrogen-doped Graphene Quantum Dots with Short/Mid/Long-wave Ultraviolet for the Development of the UV Photodetector[149]

4.1 Overview:

In this work, we have utilized an eco-friendly microwave-assisted hydrothermal method for the synthesis of nitrogen-doped graphene quantum dots (N-GQDs) from a single glucosamine precursor yielding N-GQDs with an average size of 4.70±0.05 nm exhibiting visible and near-IR fluorescence with high quantum yield. We have further studied the optical/structural properties of N-GQDs under short (254 nm)/mid (302 nm)/long wave (365 nm) timed UV exposure showing a significant reduction of absorption up to 320 nm and appearance of new absorption peak/shoulder afterward. The fluorescence signal was also significantly affected by the UV exposure exhibiting gradual quenching of blue/near-IR emission intensity along with an exceptional increase of green/yellow fluorescence. The quenching of near-IR fluorescence can be attributed to the reduction of oxygen/nitrogen-containing functional groups detected as observed using FTIR, whereas the quenching of the blue and the increase of the green/yellow fluorescence can be potentially ascribed to the increase of N-GQD average size from 4.70±0.05 to 11.20±0.35 nm captured by HRTEM (high-resolution transmission electron microscope) with 0 to 60 min UV exposure. The size tuning of N-GQDs takes place due to the free-radical polymerization induced by controlled UV irradiation yielding lateral size increase of N-GQDs to that optimal for 500 nm

excitation and yellow emission, while concomitantly decreasing the number of N-GQDs responsible for blue emission with 350 nm excitation.

The significant change in the optical and structural properties of N-GQDs due to short/mid/long wave UV illumination discovered in this work lead to further development and fabrication of a UV photodetector devices based on an N-GQD photo-sensing layer. The UV photodetector device fabricated from N-GQDs showed fast photo-switching characteristics with 96, 87, and 38 ms rising time and 73, 119, and 74 ms decay time under 365, 302, and 254 nm UV illumination respectively. It conveniently exhibits no signal under room light condition whereas strong responsivity (up to 0.59 A/W) and excellent detectivity (up to $1.03X10^{11}$ Jones) were observed and calculated under short/mid/long wave UV exposure at 2V bias voltage. These calculated parameters are comparable and/or improved with respect to those previously reported for quantum dot devices which in combination with eco-friendly simple and scalable fabrication makes N-GQD-based UV photodetectors developed in this work a promising optoelectronic solution.

4.2 Experimental methods and procedures

4.2.1 Synthesis/Characterization of N-GQDs and UV treated N-GQDs

A 0.14M aqueous suspension of glucosamine-HCl (purchased from Sigma-Aldrich) was processed in a commercially available microwave (Hamilton Beach, model: HB-P90D23AP-ST) for 60 min at 450W (power level 3) to produce nitrogen-doped graphene quantum dots. As-prepared N-GQDs were purified using a dialysis bag (0.5–1 kDa MWCO) for seven days with DI water which was changed several times during the purification process. The purified N-GQDs are further processed under UV irradiation with a benchtop 3UV transilluminator (LMS-20, 8W) as UV light source for

the period of 0 to 60 min with a 5-10 min interval. High-resolution Transmission Electron Microscope (TEM JEOL JEM-2100) was used for the morphological characterization of untreated NGQDs and UV treated NGQDs. Samples for TEM were prepared on a carbon-coated 200-mesh copper grid under room temperature environment. Visible/NIR fluorescence spectra of untreated N-GQD and UV treated N-GQD samples was measured with a Horiba Scientific SPEX NanoLog Spectrofluorometer at 350, 400, 500, 730 nm excitation[46], and the absorbance spectra of these samples within the range of 200 to 800 nm was measured with a Cary 60 UV-Vis (Agilent Technologies) absorption spectrometer. A Virtis (Freezemobile 25 ES) lyophilizer was employed to freeze-dry the untreated N-GQD and UV treated N-GQD. These freeze-dried samples were used to measure the FTIR spectra via the attenuated total reflection (ATR) mode of a Thermo Nicolet Nexus 670 FTIR. In order to trace the sp^2 hybridized carbon structure and defects-induced disorders in untreated NGQDs and UV treated NGQDs a DeltaNu Raman spectrometer with 785 nm excitation at 100 mW maximum power was used. Solution-processed untreated-NGQDs and UV-treated-NGQDs were deposited on a silicon wafer via spin-coating at 1000 and 3000 rpm for 30s to prepare the samples for Raman and tapping mode AFM (NT-MDT nanosolver) measurements, respectively that provided a topological characterization of the materials.

4.2.2 Device fabrication

A 24x12 (LxW) mm Silicon substrate was used to fabricate UV photodetector devices, which was cleaned by submerging into 10% aqueous HCl for 1 hour with further ultrasonic bath in Acetone for 1 hour followed by drying with compressed nitrogen. Gold electrodes were deposited on the silicon substrate using an Anatech Hummer-VII (SL No: 2807002) gold

sputtering deposition system run for 50 min (each min yields 1 nm thick gold coating). The thickness of the deposited gold electrode was verified further with a scanning electron microscope (SEM, JEOL-JSM-7100F) by capturing the cross-section image of the device showing a 160 nm layer of SiO_2 and a 50 nm thick gold electrodes. A device channel with a length of 2 mm and a width of 12 mm was built in the middle of the substrate to deposit N-GQDs *via* a drop-coating method. After drop-casting the solution-processed NGQDs onto the device channel, it was annealed at 80°C for 20 min to evaporate the water. SEM was used to assess the layer-wise elemental distribution and morphological characterization of the device, whereas a Keithley 2420 source meter instrument was utilized to record the electrical response of UV photodetectors under three different wavelengths of UV irradiation.

4.3 Results and discussion

In order to synthesize the NGQDs, a single glucosamine-HCl precursor is used as a source of carbon/nitrogen and processed further in a commercially available microwave oven. The intermolecular and intramolecular dehydration takes place due to the hydrothermal reaction with prolonged microwave treatment creating polymers/aromatic clusters followed by the condensation and carbonization at a supersaturation condition along with the doping of nitrogen, resulting into subsequent formation of well-distributed NGQDs. As we successfully synthesized these materials before and performed extensive morphological characterization[46] in the previous chapter, therefore, in this chapter, we prioritize our focus on the UV-induced alteration of optical properties followed by the characterization of modified structural properties due to UV irradiation. Previous studies show that UV treatment can be utilized as a reduction pathway to produce reduced

graphene oxide (RGO) from graphene oxide (GO)[150-152] concomitantly tuning GO band structure and optical properties. Therefore, it is expected that UV irradiation might induce a characteristic variation in the optical/structural properties of graphene-based quantum dots as well.

Aqueous suspensions of pristine NGQDs are irradiated with short (254 nm), mid (302 nm), and longwave (365 nm) ultraviolet light for a period of 0 to 30 min with 5 min increments and 30 to 60 min with 10 min increments to modify their optical properties. UV treated sample shows a dramatic change in color from transparent to dark yellow (Figure 4.1), indicating significant variations of the visible absorption and potential alterations of NGQDs electronic structure. Absorbance measurements of 254 nm UV treated NGQDs show a slight change in π-π* electronic transition of C=C peaking at ~215 nm (Figure 4.2a) whereas a significant variation is observed in the intensity of three absorption peaks at 239, 283, ~317 nm (by the factor of ~3.25, ~1.22, ~1.8 respectively) that are attributed to the n-π* electronic transitions of C=C, C=O[115], and π-π* transition of C=N[116], respectively (Figure 4.2a). Additionally, new absorbance features appear within the range of 330 to 380 nm showing a monotonous increase in intensity (by a factor of ~4.65 at 60 min) along with red-shifted absorbance with prolonged short-wave UV exposure. The new peak position suggests the formation of shortwave UV-induced n-π* electronic transitions of oxygen/nitrogen-containing functional groups(Figure 4.2a). The variation of NGQD optical properties is monitored further by fluorescence measurements at four different excitation wavelengths (350, 400, 500, 730 nm). NGQD sample excited at 350/730 nm exhibits a gradual decrease (Figure 4.2b,f) in visible/NIR emission intensity along with a red/blue shift in peak maxima for visible/NIR emission, respectively.

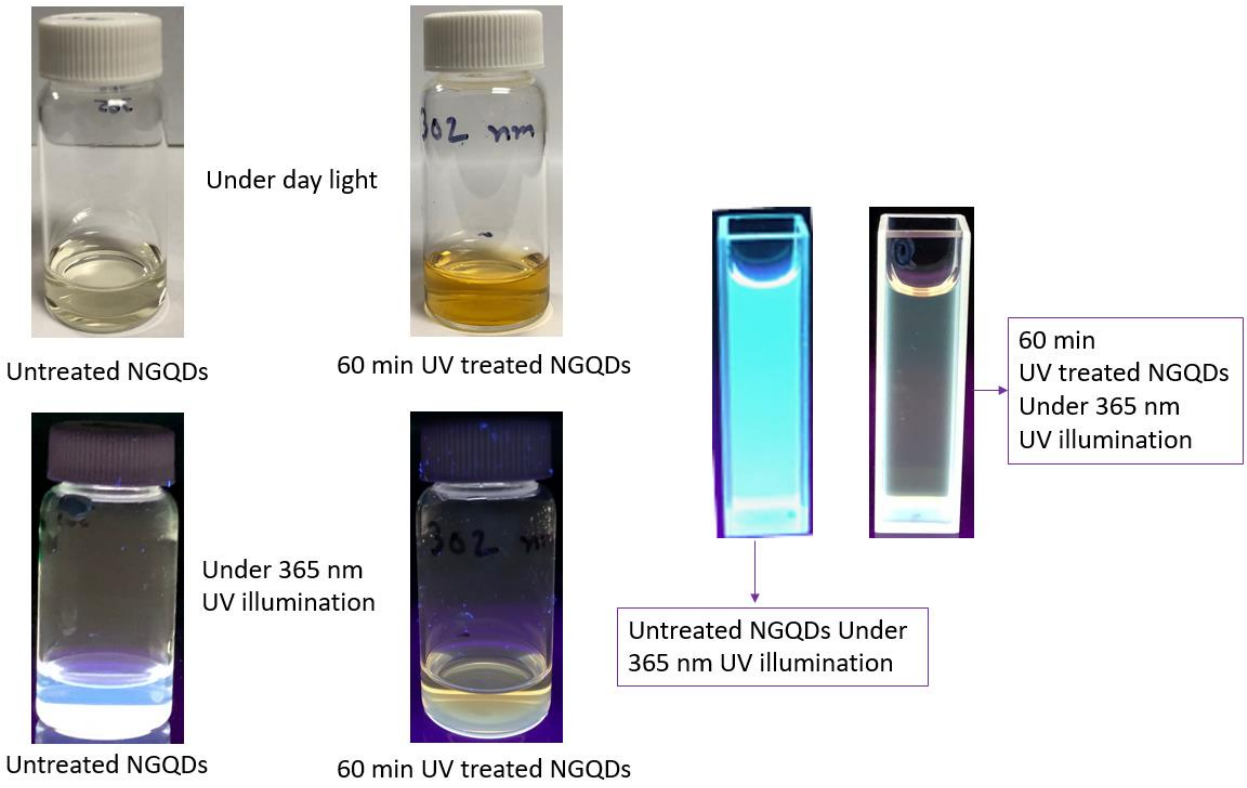

Figure 4.1: Sample color of untreated NGQDs (Un-NGQDs) and 60 min UV treated NGQDs (60 min UVT-NGQDs) under day light and 365 nm UV illumination.

However, for 50/60 min UV-treated samples at 400 nm excitation, the emission intensity decreases up to 40 min UV illumination and then increases slightly (Figure 4.2c,d). Interestingly, we also observe a significant increase in emission intensity in the yellow region with 500 nm excitation (Figure 1(e)). Since the origin of GQD visible emission is attributed to the quantum confinement effect, these excitation-dependent variations in fluorescence features may arise due to the UV-induced changes in the GQD structures and size distributions. The decrease of emission intensity with 350, 400 nm excitation and the corresponding increase of NGQD emission at 500 nm

excitation suggests two possible scenarios: (1) NGQDs size gets altered in a way that maximum emissive species can be excited most efficiently with 500 nm depleting or quenching all other structures leading to localization of NGQD fluorescence in the yellow, (2) similarly to sp^2 regions in GO[118], the size-tuning of GQD graphitic clusters to the diameter resonant with 500 nm excitation via selective functionalization of those (Figure 4.10, 4.11) potentially showing graphitic substructures in a single quantum dot. Moreover, the decrease in NIR emission intensity along with blue-shifted peak maxima can be related to potential passivation of defect states supporting the hypothesis of defects-associated[46] origin of NIR emission of GQDs described in Chapter 2.

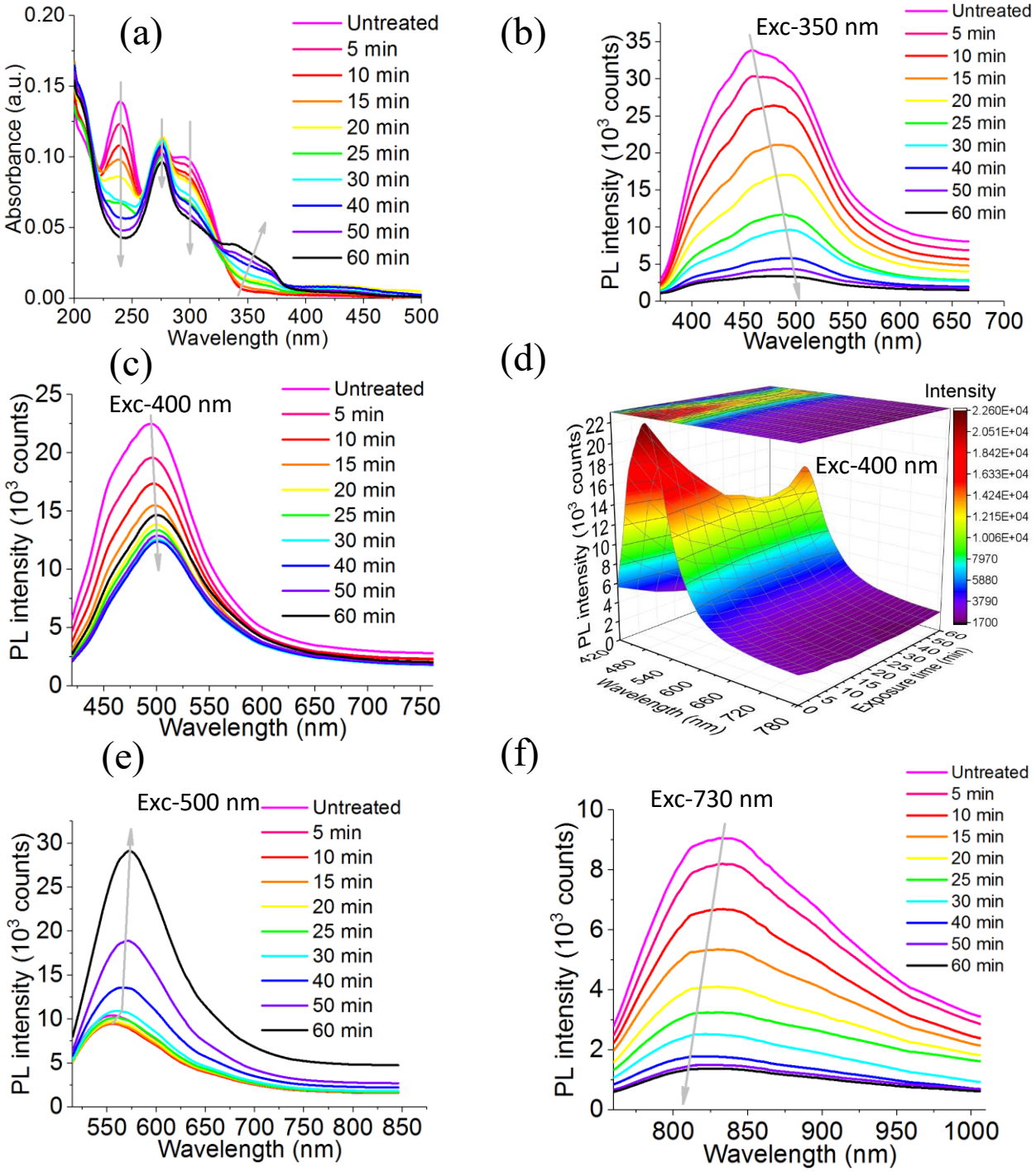

Figure 4.2: (a) Absorbance spectra of 0 to 60 min short-wave (254 nm) UV treated NGQDs. Fluorescence spectra of 0 to 60 min short-wave (254 nm) UV treated NGQDs excited at (b) 350 nm, (c) 400 nm, (d) 400 nm (corresponding 3-D plot), (e) 500 nm, and (f) 730 nm.

Although the treatment with 254 nm UV light (highest energy treatment for this work) is supposed to induce the maximum structural changes in GQD structure, we observe the most significant optical changes with 302 nm UV illumination. Compared to the 254 nm UV treatment, NGQDs treated with 302 nm UV light exhibit much higher reduction of absorption peaks at 239, 283, 317 nm (by a factor of ~3.65, ~1.57, ~2.00 respectively) and increase of absorbance shoulder ranging from 325 to 390 nm (by a factor of ~5.62) (Figure 4.3a). The similar fluorescence changes are observed for 302 nm UV treated NGQDs as for 254 nm UV treated ones: with 350/730 nm excitation, a gradual decrease of fluorescence intensity along with a slight red-shifted (Figure 4.3b)/blue-shifted (Figure 4.3f) peak maxima, are respectively observed. Unlike with 254 nm treatment, an initial decrease in fluorescence intensity at 400 nm excitation up to 20 min treatment followed by an intensity increase from 20 to 60 min UV irradiation along with the appearance of a shoulder at ~578 nm (Figure 4.3c,d) is observed. Moreover, a staggering (~90 fold) increase in fluorescence intensity showing peak maxima at ~578 nm with 500 nm excitation (Figure 4.3e, 4.4) occurs, suggesting that confinement-induced fluorescence emission localizes in the yellow region due to substantial size-tuning of NGQDs or their emissive clusters with 302 nm UV treatment.

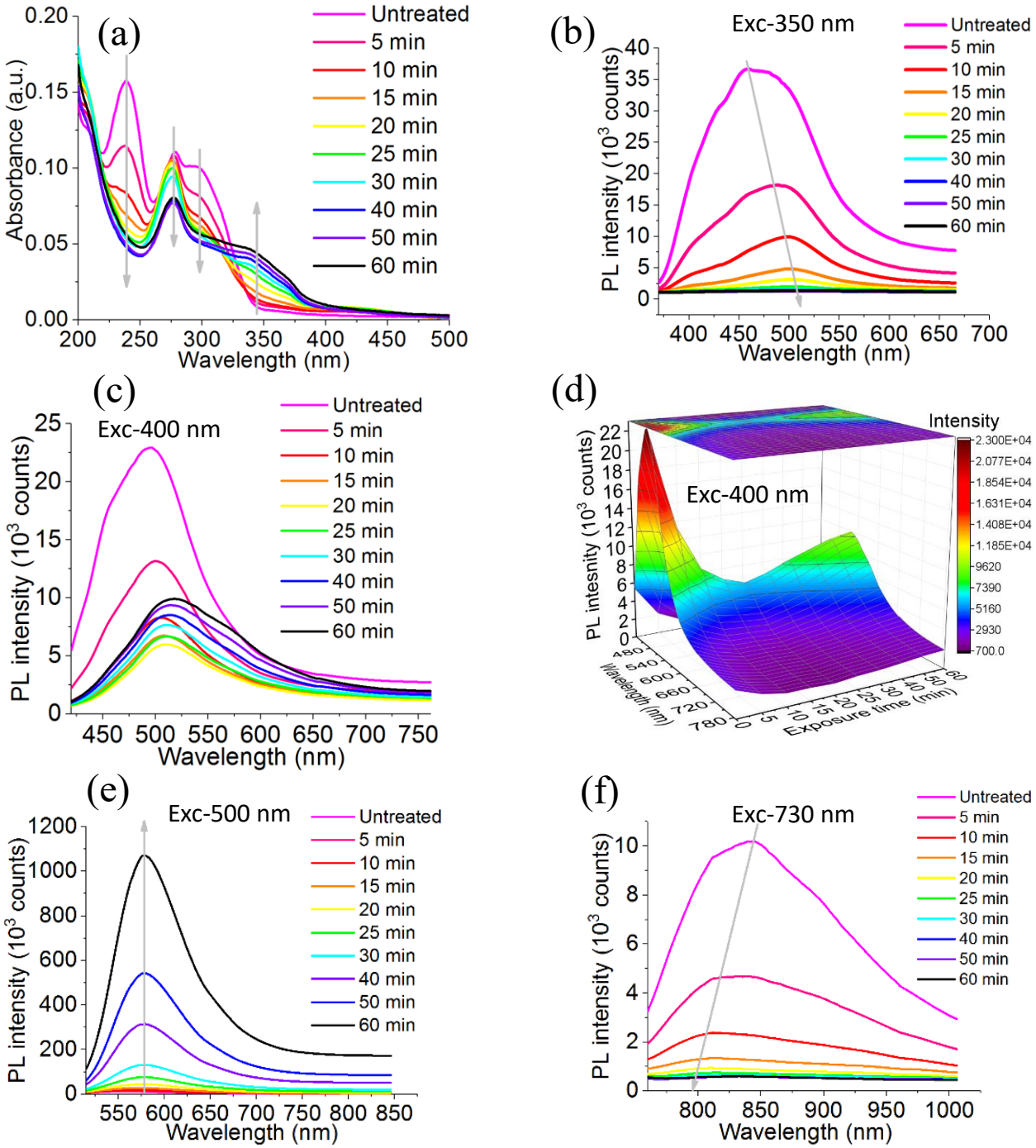

Figure 4.3: (a) Absorbance spectra of 0 to 60 min mid-wave (302 nm) UV treated NGQDs. Fluorescence spectra of 0 to 60 min mid-wave (302 nm) UV treated NGQDs excited at (b) 350 nm, (c) 400 nm, (d) 400 nm (corresponding 3-D plot), (e) 500 nm, and (f) 730 nm.

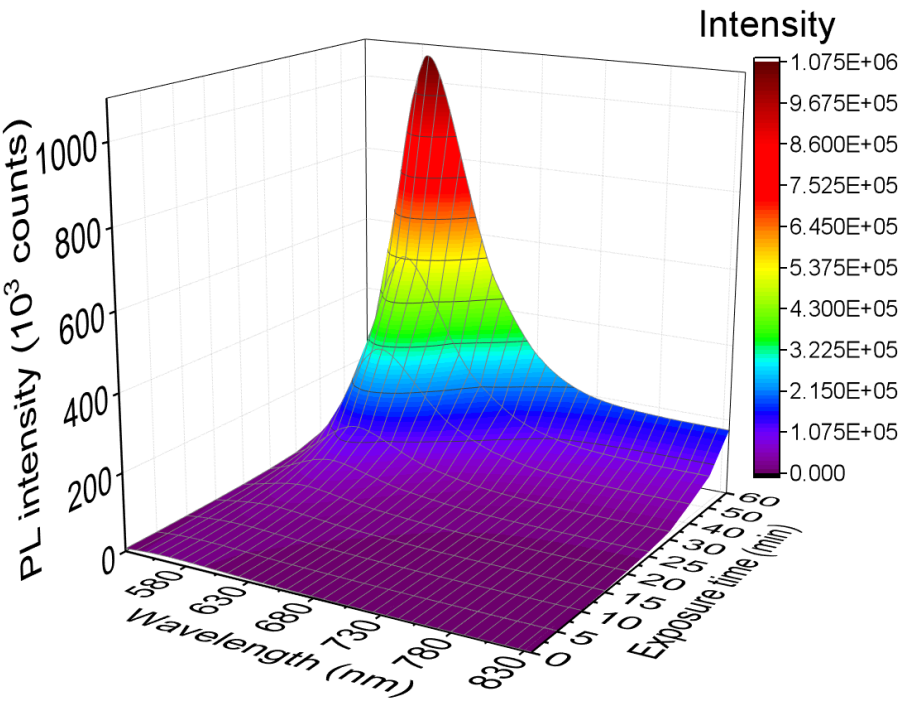

Figure 4.4: Corresponding 3-D plot of the fluorescence spectra of 0 to 60 min mid-wave (302 nm) UVT-NGQDs excited at 500 nm.

Finally, a 365 nm UV light is used to treat the pristine NGQDs throughout 0 to 60 min showing no significant change in absorbance intensity (Figure 4.5a) along with no new absorption peaks/shoulders indicating no UV-induced alteration of major absorbing species. The fluorescence intensity decreases gradually with 350, 400, and 730 nm excitation (Figure 4.5b,c,d,f) with no significant variation at 500 nm excitation (Figure 4.5e), indicating only a minor change of NGQDs physical/electronic configuration. These slight variations suggest that 365 nm long-wave UV (lowest energy used in this work) may trigger the depletion or reduction of less stable emissive species without any change to the fluorescing species responsible for the dramatic increase of yellow photoluminescence.

The UV-induced changes in NGQD are studied further through their morphological and structural characterization with timed UV irradiation. Since most pronounced changes of NGQDs' physical/optical features are observed with 302 nm (mid-wave) UV treatment, the mid-wave UV treated NGQDs are further utilized to investigate the potential structural modification.

High-resolution transmission electron microscopy (HRTEM) is employed to analyze the change in size distribution potentially responsible for excitation-dependent quantum confinement-induced emission and to assess the quality of the crystalline lattice structure that may elucidate the changes in the internal structure of GQDs affecting their emission with prolonged UV exposure. We consider more than 270 NGQDs for the size distribution analysis providing NGQD diameters ranging from 1 to 7.5 nm with an average size of 4.70±0.05 nm and a median of 4.61 nm (Figure 4.6a,b).

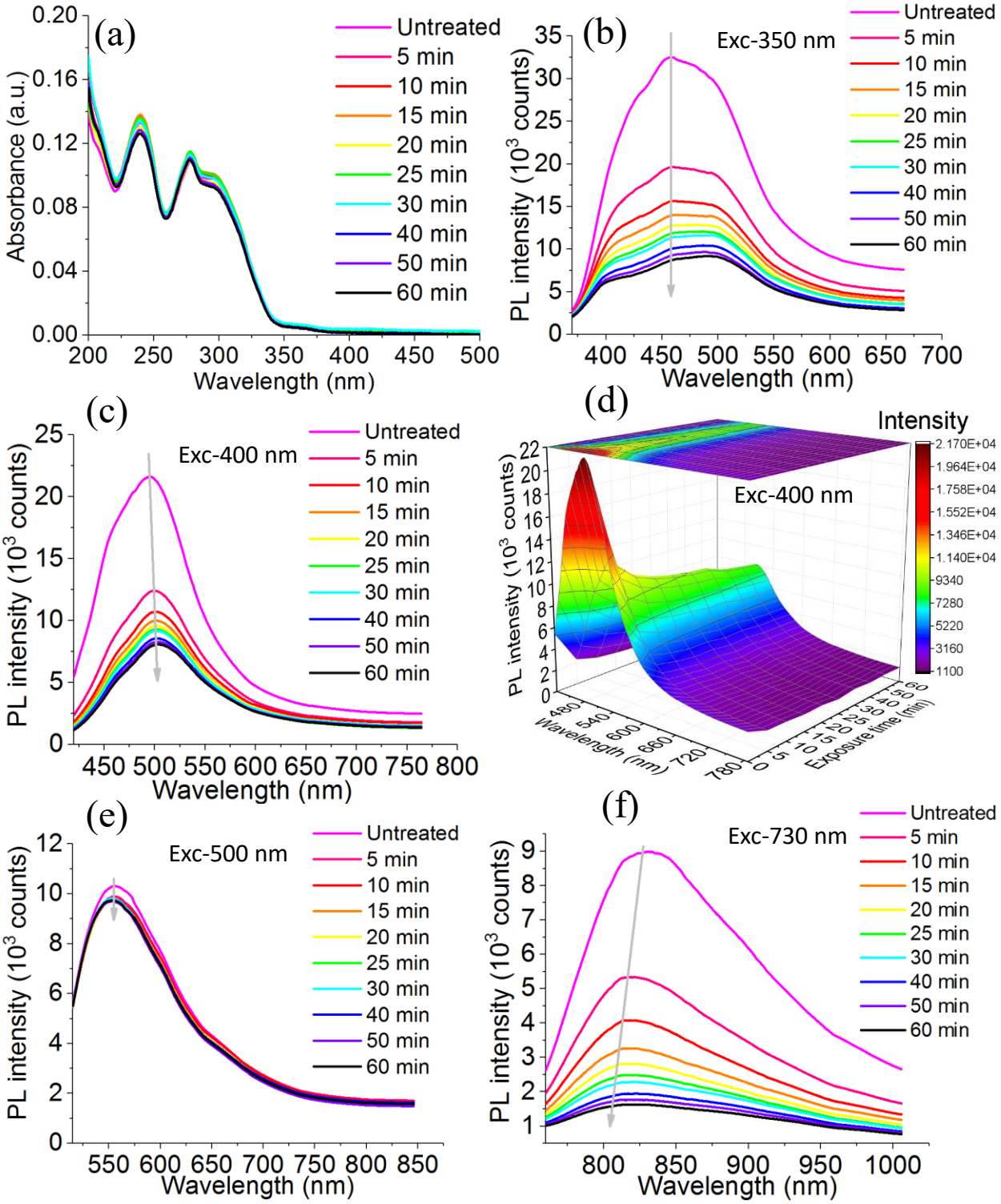

Figure 4.5: (a) Absorbance spectra of 0 to 60 min long-wave (365 nm) UV treated NGQDs. Fluorescence spectra of 0 to 60 min long-wave (365 nm) UV treated NGQDs excited at (b) 350 nm, (c) 400 nm, (d) 400 nm (corresponding 3-D plot), (e) 500 nm, and (f) 730 nm.

These NGQDs show a high crystalline lattice structure revealed by fast-Fourier-transform (FFT) images of a number of chosen areas captured by HRTEM (high-resolution transmission electron microscopy) and distinctive lattice fringes with 0.21 nm lattice spacing (Figure 4.7) assigned to the (100) plane of graphene[40]. The average diameter of NGQDs increases gradually with timed 302 nm UV illumination providing an average size of 5.01±0.07 nm for 10 min (Figure 4.6c,d), and 6.38±0.08 nm for 30 min (Figure 4.6e,f) treatment which are 1.06 and 1.35 times larger than untreated NGQDs, respectively. Interestingly, the 60 min (maximum treatment time used in this work) UV treated NGQDs show a bimodal distribution with two lobes: (1) with an average size of 6.94±0.12 nm (Figure 4.8a,b) which is still 1.48 times larger than that of untreated NGQDs and (2) with an average size of 18.32±0.31 nm (Figure 4.8c,d). The combined distribution of these two lobes provides an average size of 11.20±0.35 nm with a median of 8.40 nm (Figure 4.8e), which is much larger than untreated, or 10 to 30 min UV-treated NGQDs. Additionally, we assess the height profiles of NGQDs measured with AFM (atomic force microscopy) showing an increase in average thickness from 2.15 nm to 3.20 nm with 0 to maximum up to 60 minute UV treatment (Figure 4.13, 4.14) suggesting the formation of pseudospherical-shaped multilayer NGQDs.

This UV treatment-induced NGQDs size change can be potentially attributed to the free-radical polymerization[153] or fusing of the initial NGQDs mediated by high energy UV light irradiation.

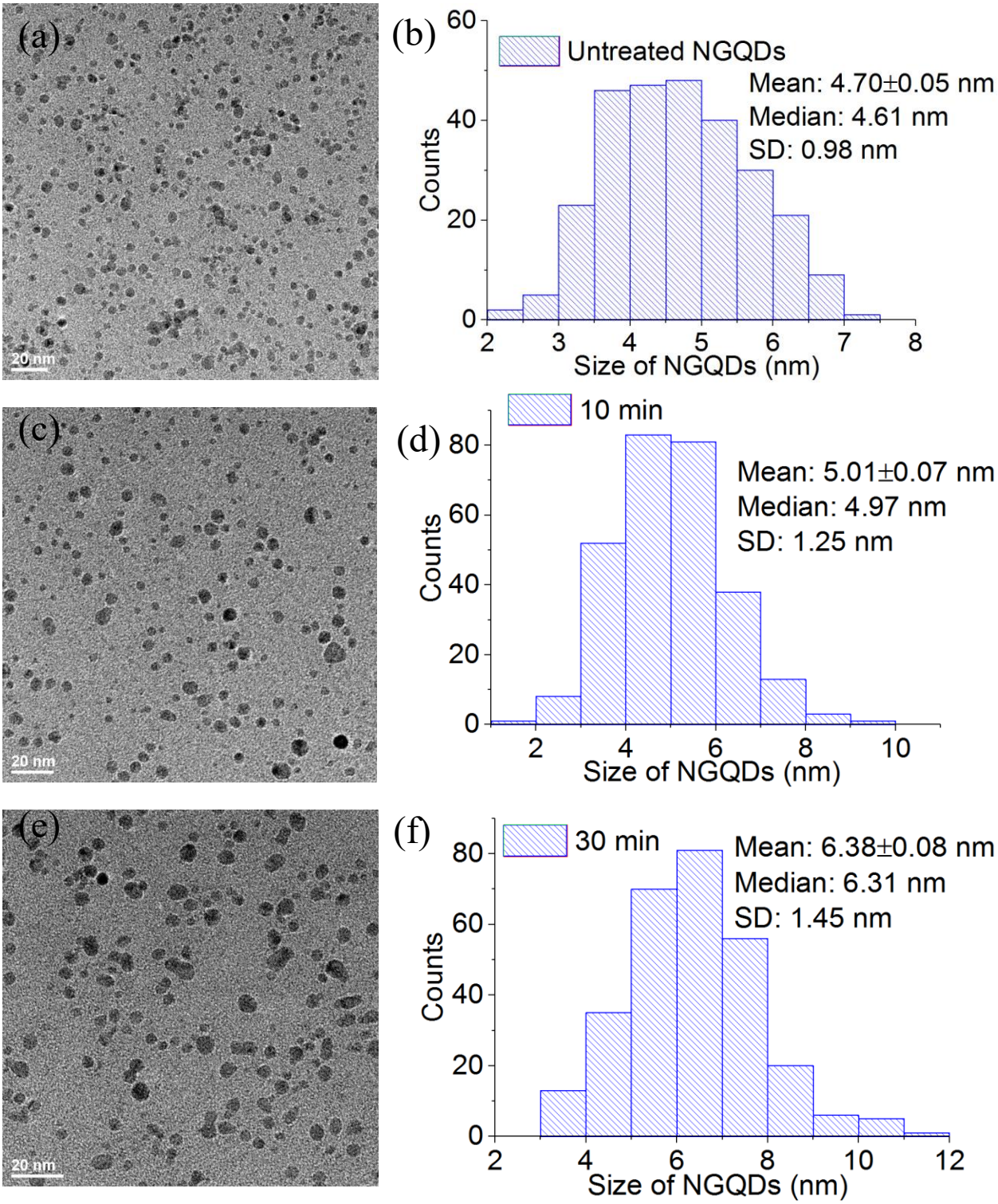

Figure 4.6: (a) TEM images showing the distribution of untreated NGQDS. (b) Size distribution of untreated NGQDs. (c) TEM images showing the distribution of NGQDS treated under 302 nm UV irradiation for 10 min. (d) Size distribution of 10 min UV treated NGQDs (e) TEM images showing the distribution of NGQDS treated under 302 nm UV illumination for 30 min. (f) Size distribution of 30 min UV treated NGQDs.

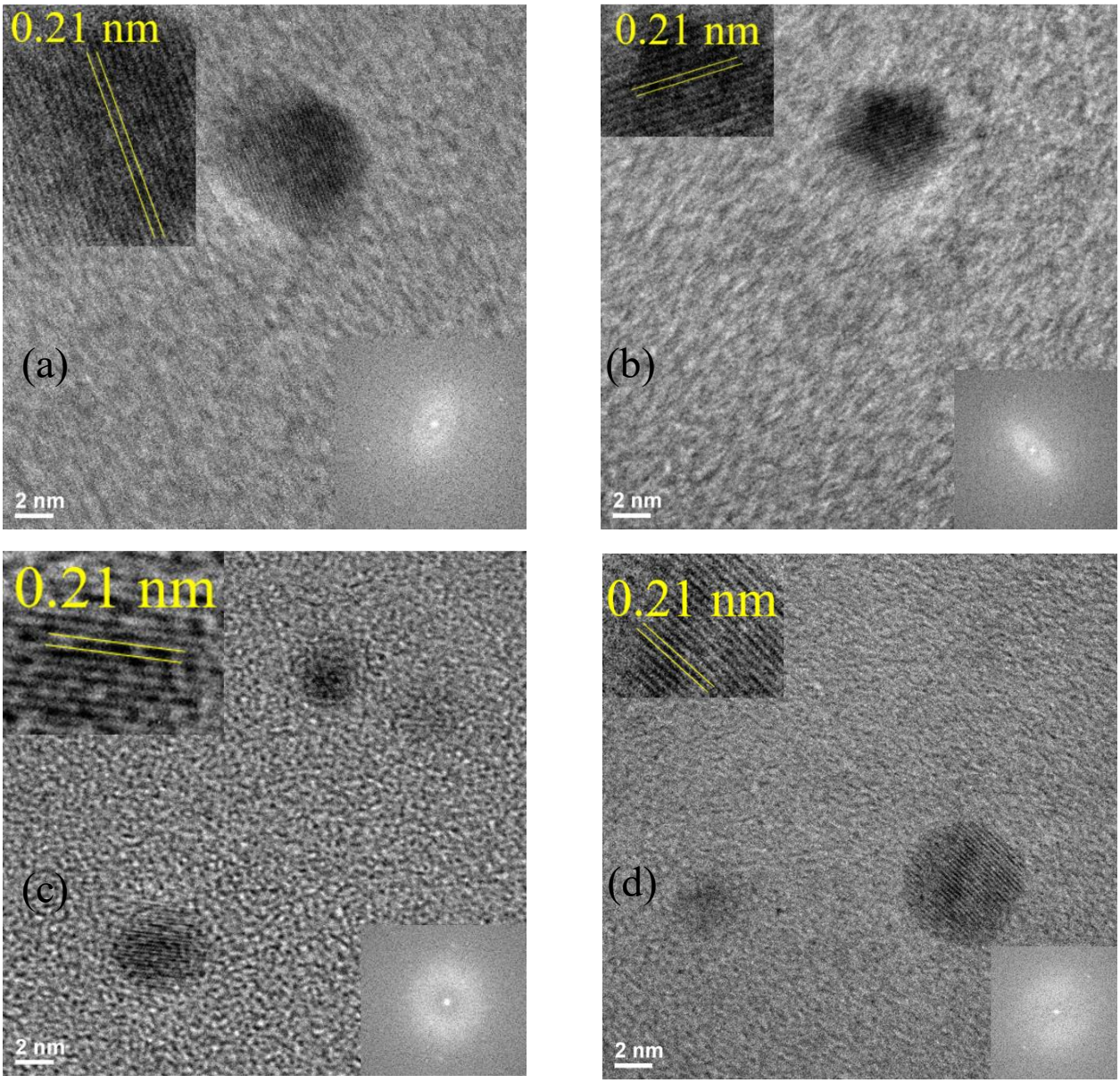

Figure 4.7: HRTEM images of (a) Un-NGQDS, (b) 10 min UVT-NGQDs, (c) 30 min UVT-NGQDs, (d) 60 min UVT-NGQDs. Inset: separation between lattice fringes (top left side) and FFT images of that selected area (bottom right side).

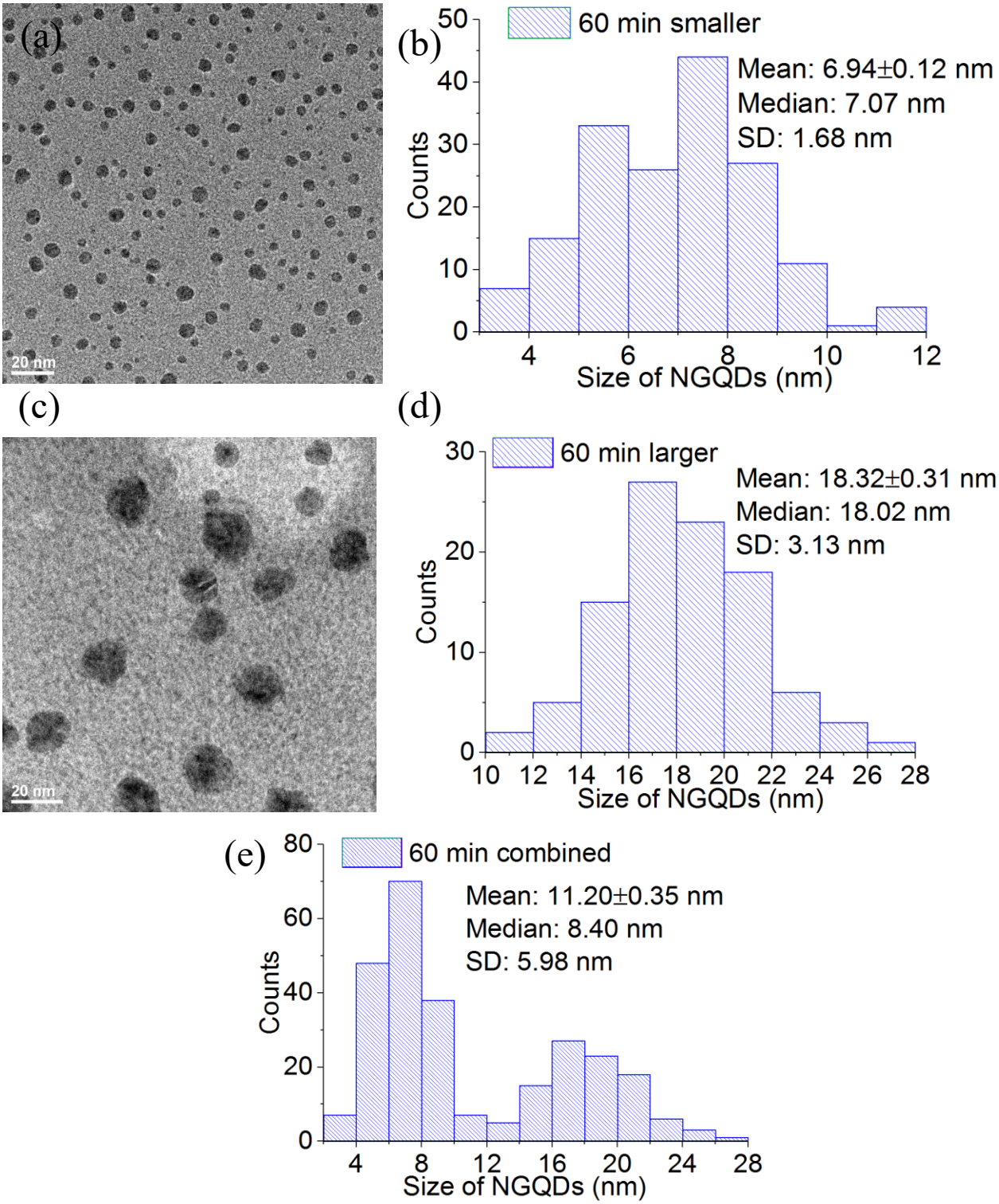

Figure 4.8: TEM images showing a bimodal distribution of NGQDS treated under 302 nm UV irradiation for 60 min. (a) Distribution of smaller-sized 60 min UV treated NGQDs (b) Size distribution analysis of smaller-sized 60 min UV treated NGQDs (c) Distribution of larger-sized 60 min UV treated NGQDs (d) Size distribution analysis of 60 min UV treated NGQDs (e) Combined size distribution of 60 min UV treated NGQDs.

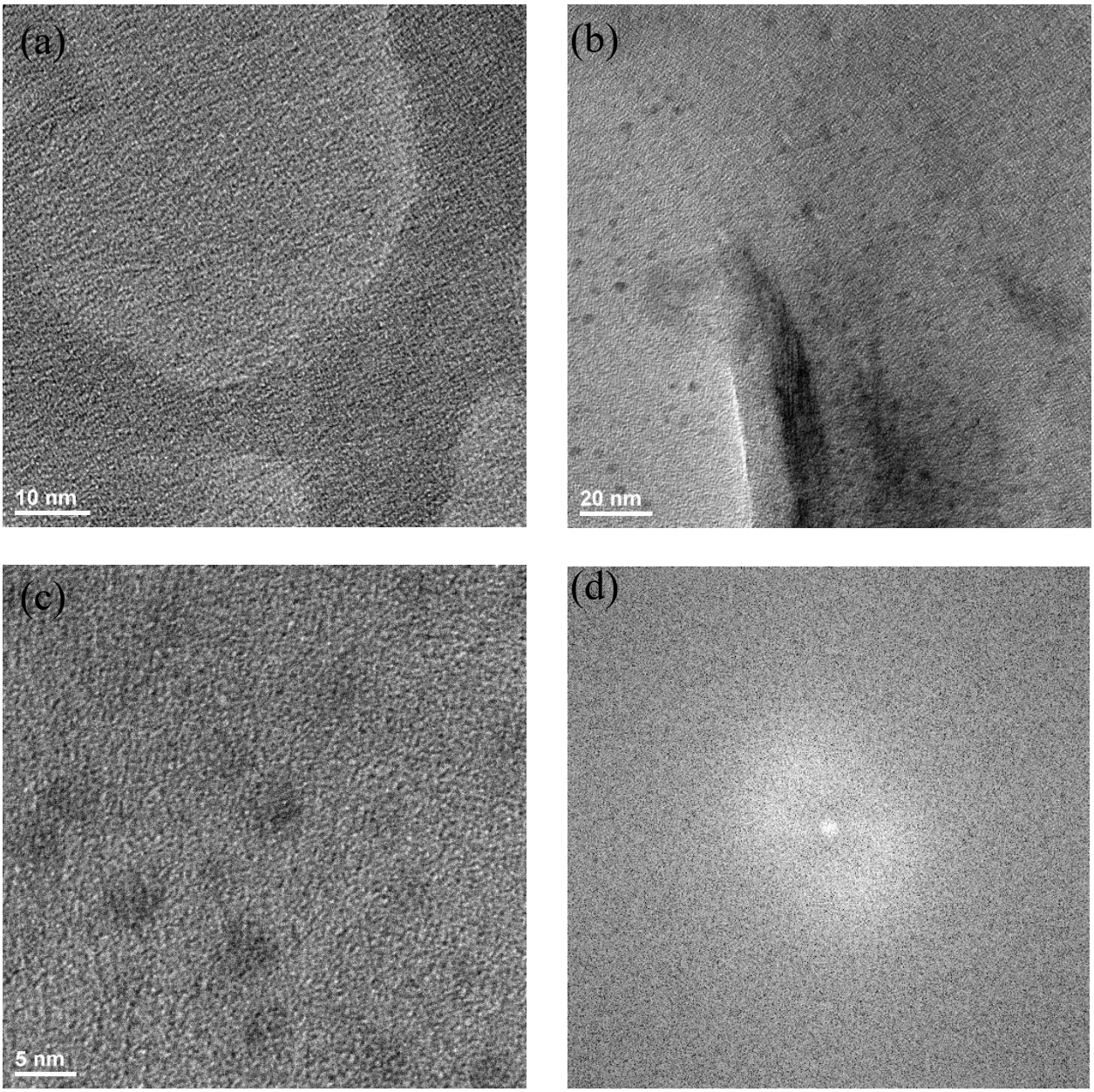

Figure 4.9: TEM images of (a) untreated glucosamine (b) 60 min UV treated glucosamine showing polymerized dots. HRTEM images of 60 min UV treated glucosamine (c) showing no distinguishable lattice fringes, (d) FFT images of the selected area showing no crystallinity.

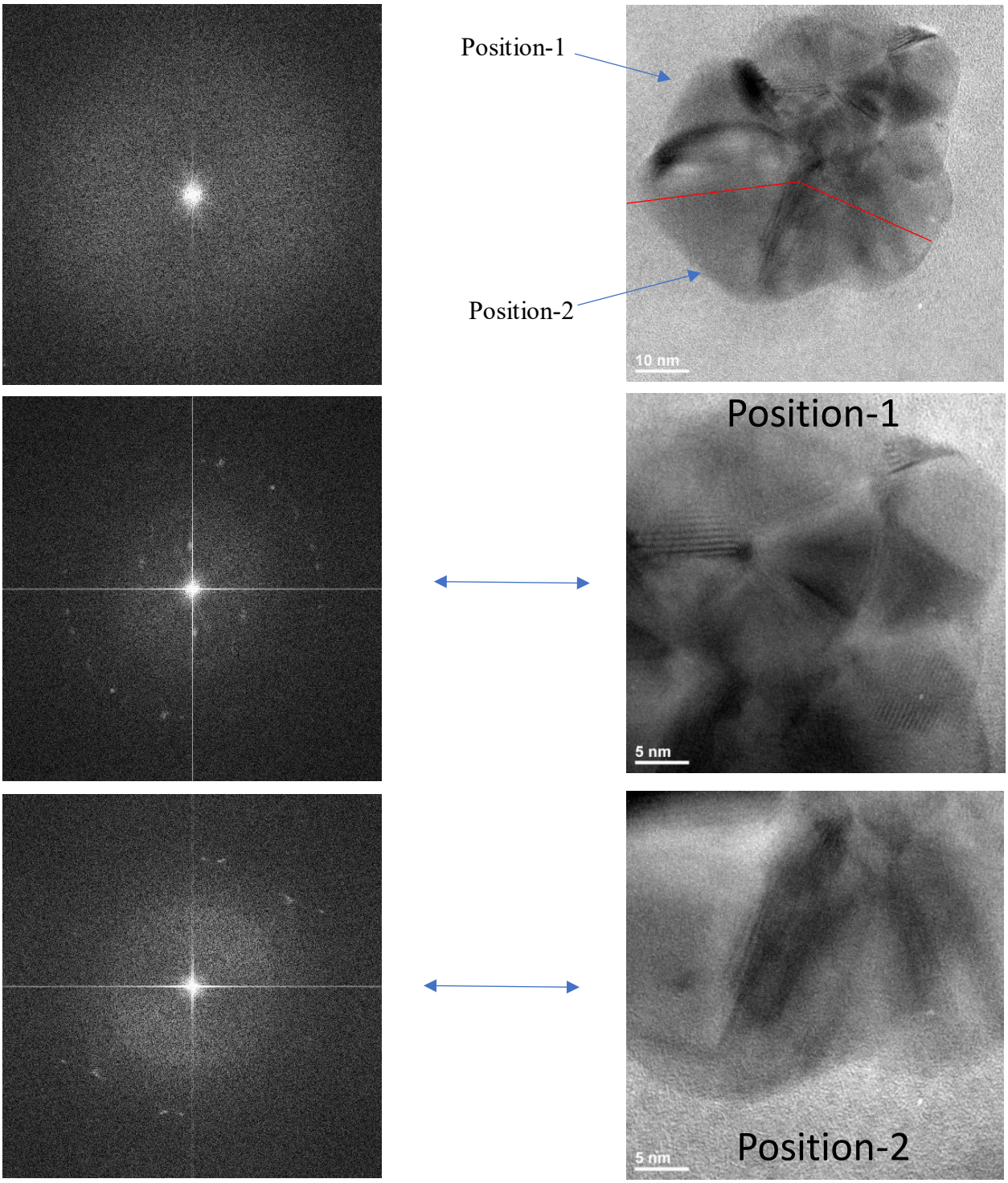

Figure 4.10: HRTEM images of larger sized NGQDs (Right side) and their corresponding FFT images (left side).

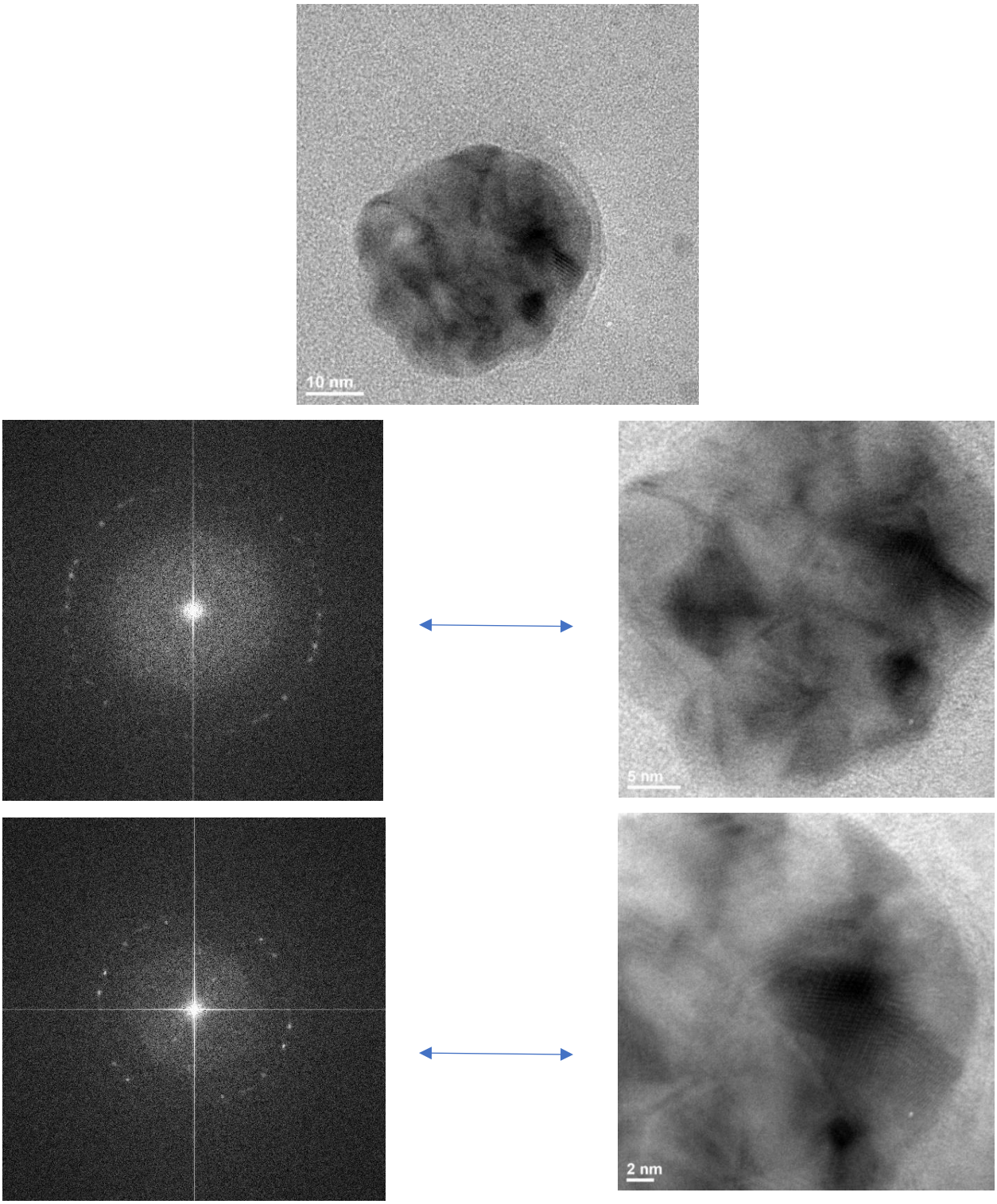

Figure 4.11: HRTEM images of larger sized NGQDs (Right side) and their corresponding FFT images (left side).

Since purified NGQDs are used for the UV treatment with low glucosamine impurity content, the formation of larger GQDs from unreacted glucosamine is improbable[46]. However, to explore that option, we irradiate the sole aqueous glucosamine precursor for 60 min with mid-wave UV light yielding few free-radical polymerized dots (Figure 4.9a,b) without any signs of crystallization and distinguishable lattice fringes (Figure 4.9c,d) indicating no growth of graphitic structures. Additionally, the fluorescence of UV treated glucosamine precursor shows no change (Figure 4.12) as compared to the untreated one indicating that no modification of optical properties takes place with only UV irradiation.

Besides the alteration of NGQDs size potentially due to polymerization, it is also expected that UV treatment may induce variations in NGQD chemical composition considering the observed profound changes in NGQD absorbance features. Fourier transform infrared (FTIR) spectroscopy is utilized to observe the UV-induced changes in NGQDs chemical composition showing a considerable decrease in 3275, 3090, and 2935 cm^{-1} vibrational transitions of O-H, N-H, and C-H groups, respectively (Figure 4.15) which can be attributed to the reduction of hydroxyl groups and potential lattice deterioration near nitrogen dopants with timed 302 nm UV irradiation. The absorbance intensity of the stretching vibrations of C=O of COOH, C=C, C-O-C, C-N/ N-H centered at 2935, 1602, 1530, 1412, and 1240 cm^{-1} also decreases significantly along with the stretching band at 1021 cm^{-1} (Figure 4.15) corresponding to the vibrational transition of C-O. Overall, these changes indicate the removal of the oxygen/nitrogen-containing functional groups[85, 111].

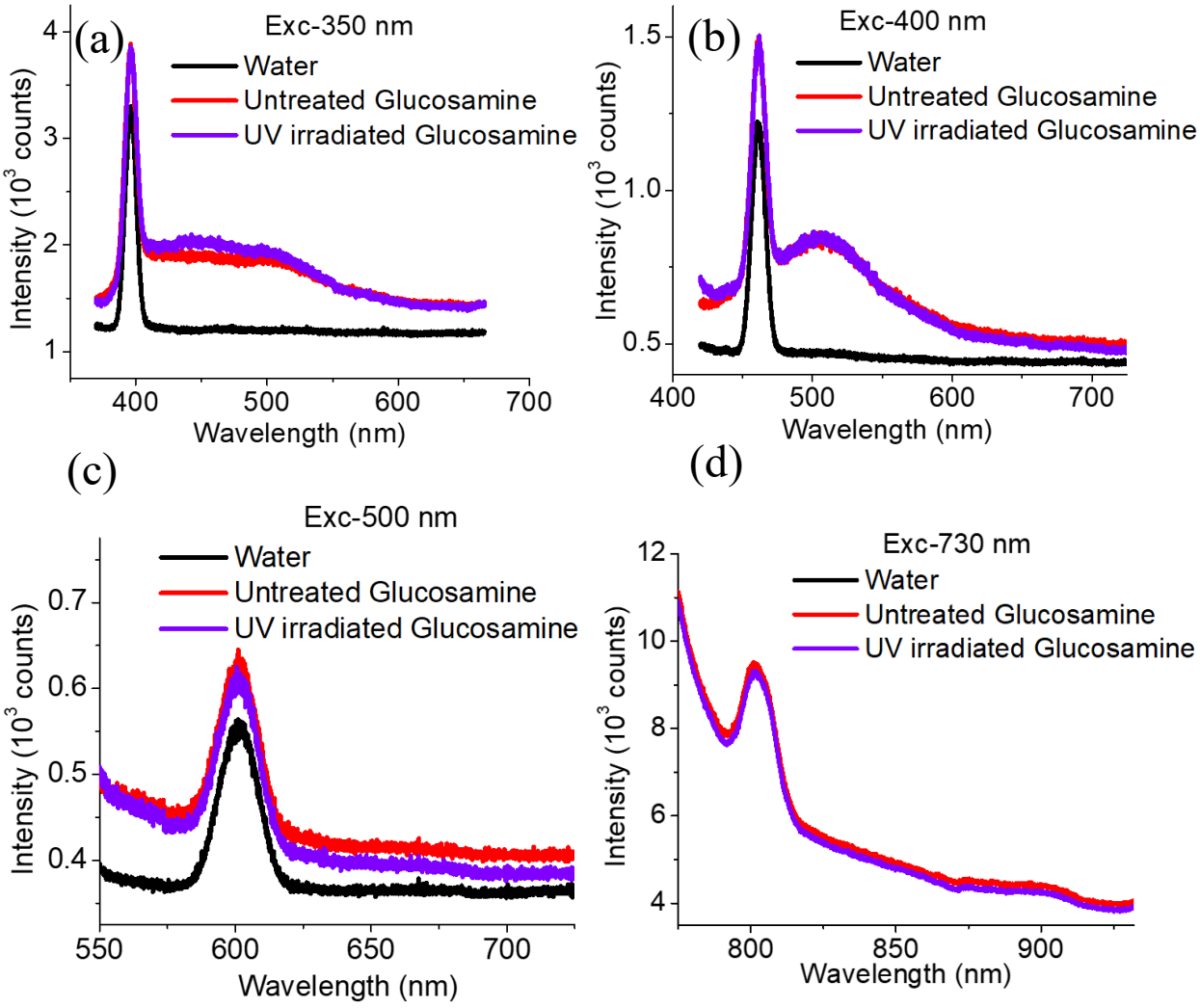

Figure 4.12: Fluorescence spectra of DI water control, untreated glucosamine, 60 min UV treated glucosamine excited with (a) 350 nm, (b) 400 nm, (c) 500 nm, (d) 730 nm excitation wavelength showing only a shoulder with no apparent emission peaks other than the water Raman peak.

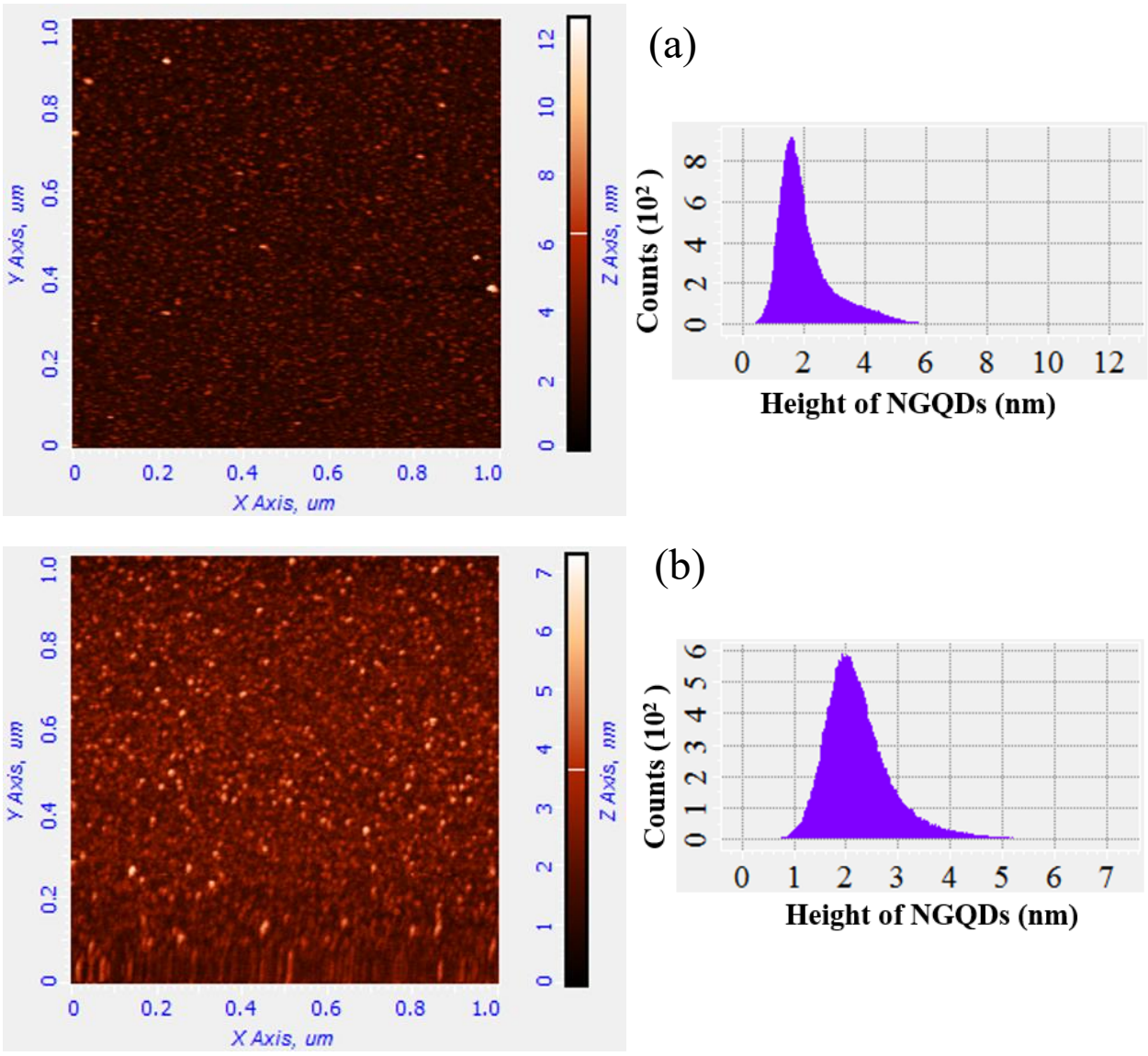

Figure 4.13: AFM images (left side) and height profiles (right side) of (a) untreated N-GQDs (b) 10 min UV treated N-GQDs.

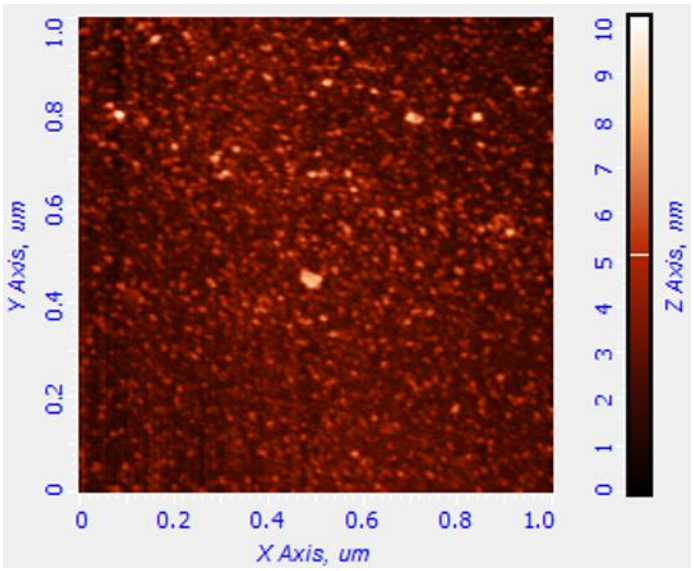

(a)

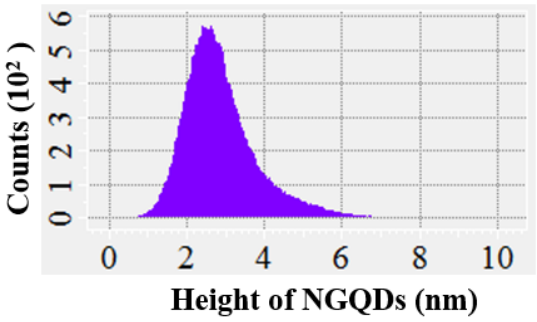

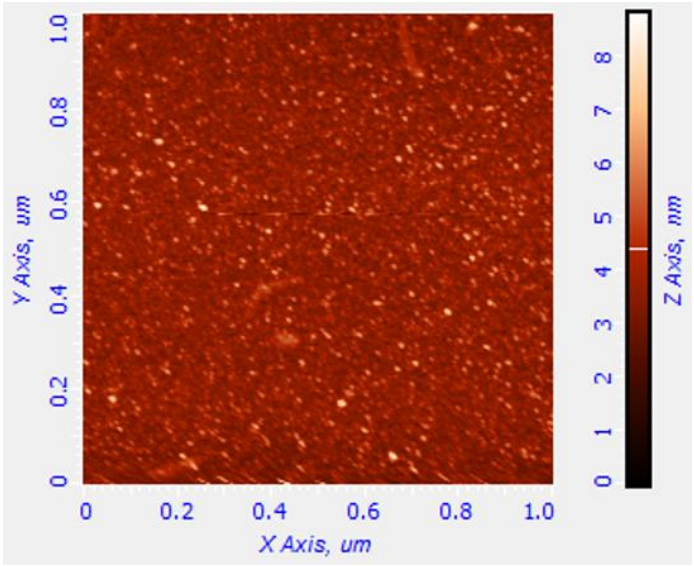

(b)

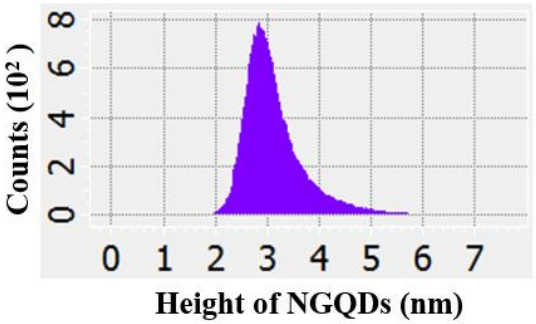

(c)

Treatment time (min)	Average thickness (nm)	SD (nm)
0	2.15	0.95
10	2.30	0.65
30	2.95	0.95
60	3.20	0.60

Figure 4.14: AFM images (left side) and height profile (right side) of (a) 30 min UVT-NGQDs, (b) 60 min UVT-NGQDs, (c) Table of average thickness of NGQDs with timed UV exposure.

The reduction mechanism of these NGQDs upon UV irradiation can be potentially similar to the UV-induced reduction of graphene oxide (GO) reported previously[151] which can be expressed as follows:

$$GQDs \xrightarrow{UV\ light} GQDs(h_{vb}^{+}) + e_{cb}^{-}$$

$$h_{vb}^{+} + H_2O(or\ OH^{-}) \rightarrow \bullet OH(+H^{+})$$

$$C-O-C(GQDs)or, other\ groups + 2H^{+} + 2e^{-} \rightarrow C-C(defect\ carbons) + H_2O$$

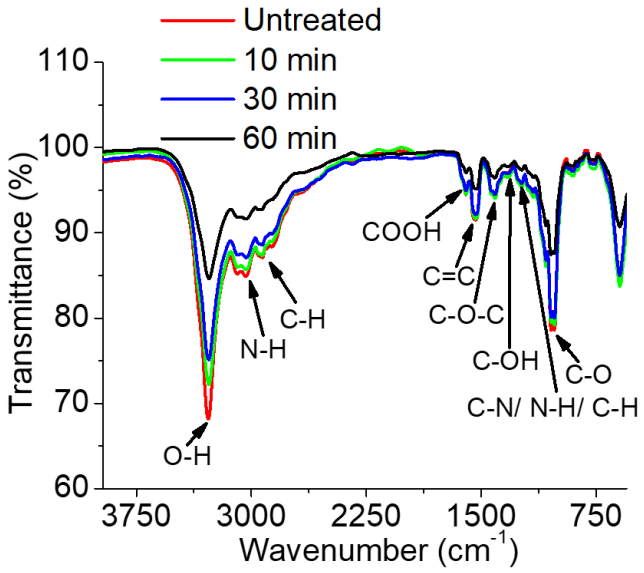

Figure 4.15: FTIR spectra of untreated, 10 min, 30 min and 60 min UV-irradiated NGQDs.

Raman measurements further support the UV-induced alteration of N-GQD structural properties, showing an increase in the intensity for D (sp^3 defect-related) band from UV-treated NGQDs along with an increase in I_D/I_G ratio from 0.80 (untreated) to 1.20 (30 min treatment) (Figure 4.16). This indicates the increased degree of disorder in the graphitic lattice potentially due to the defects left from the removal of functional groups. However, the I_D/I_G ratio for 60 min UV treated NGQDs

decreases down to 0.78 which could be related to the reduction-facilitated enhancement of the G-band known to occur in RGO as with further reduction defects can be cured and larger graphitic segments formed. EDX (Energy-dispersive X-ray Spectroscopy) measurements deliver the elemental distribution of untreated and 10, and 60 min UV treated NGQDs showing the presence of carbon/nitrogen/oxygen via EDX mapping (Figure 4.17) along with a moderate decrease in atomic/weight percentage of carbon atoms and considerable increase in nitrogen/oxygen content after UV exposure further confirming UV-facilitated reduction (Figure 4.18).

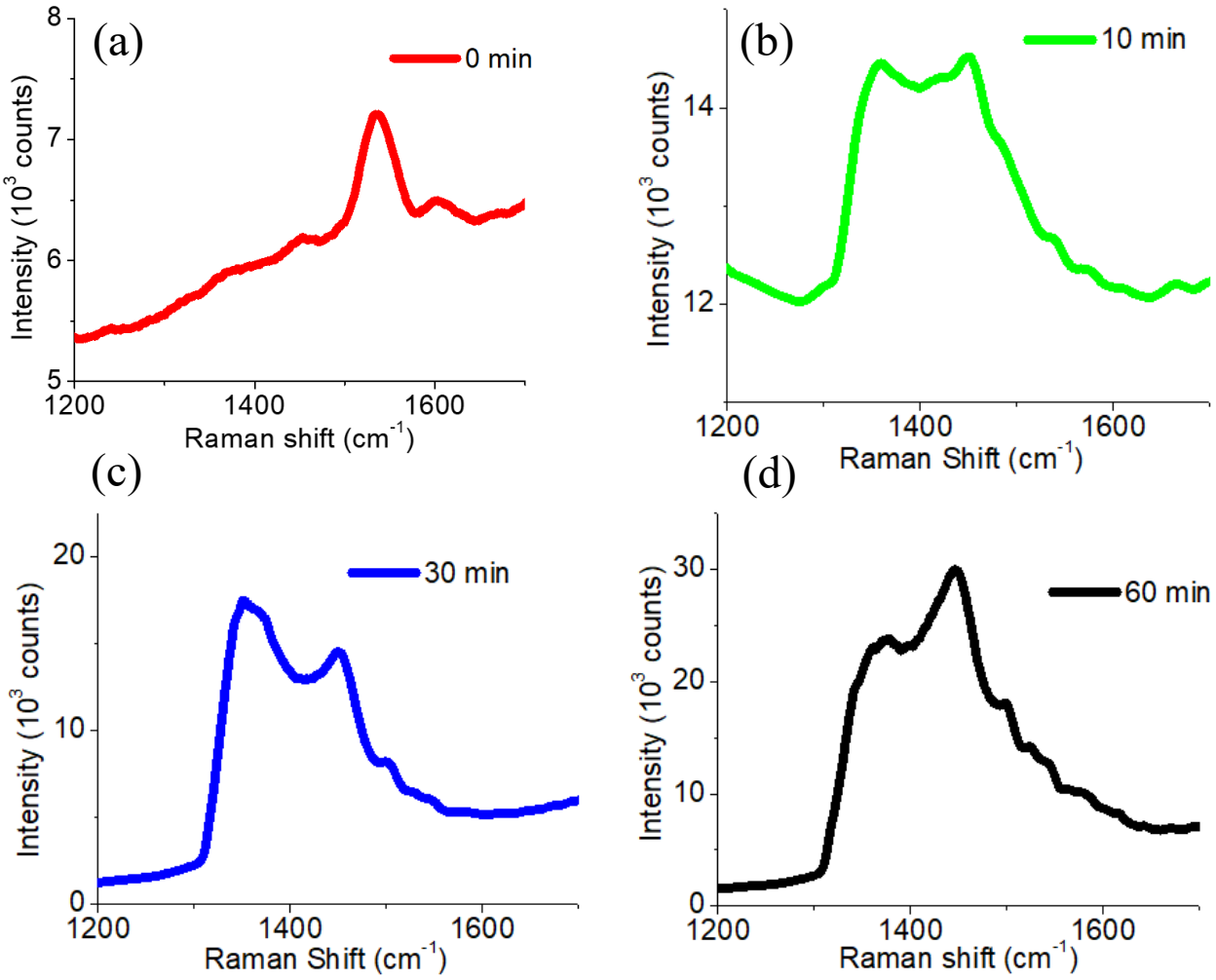

Figure 4.16: Raman spectra of (a) untreated NGQDs, (b) 10 min UVT-NGQDs (c) 30 min UVT-NGQDs (d) 60 min UVT-NGQDs.

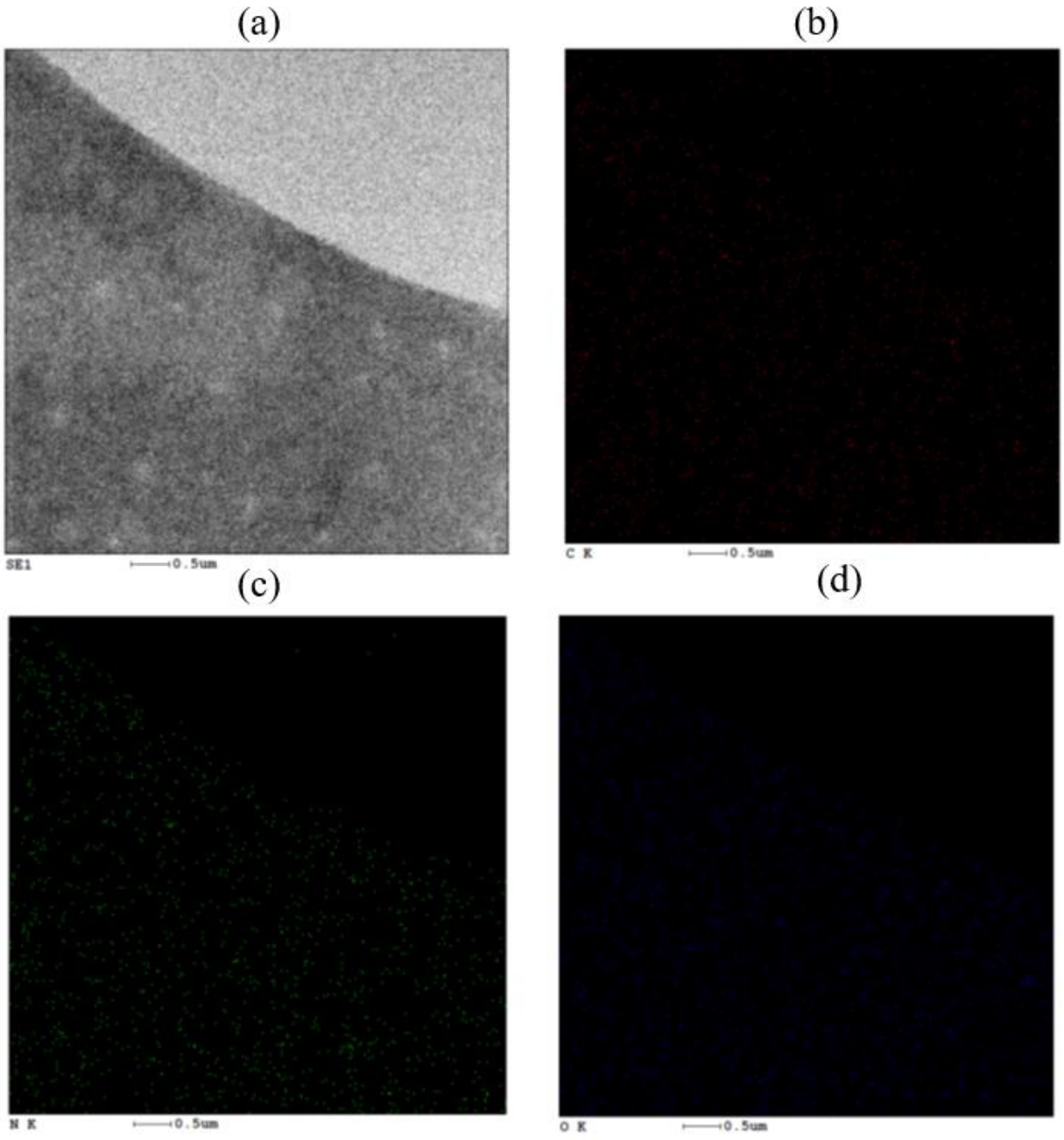

Figure 4.17: EDX mapping data of untreated NGQDs showing the (a) scan area, presence of (b) carbon, (c) nitrogen, (d) oxygen element.

(a)

Element name (Shell)	Untreated NGQDs (Wt%)	10 min UV-treated NGQDs (Wt%)	60 min UV-treated NGQDs (Wt%)	Untreated NGQDs (At%)	10 min UV-treated NGQDs (At%)	60 min UV-treated NGQDs (At%)
C(K)	83.89	67.45	65.27	86.64	72.02	69.82
N(K)	7.91	16.50	20.10	7.00	15.11	18.43
O(K)	8.20	16.05	14.63	6.36	12.87	11.75

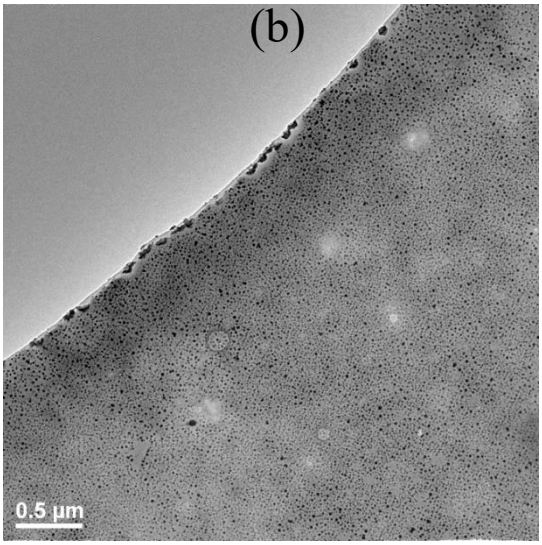

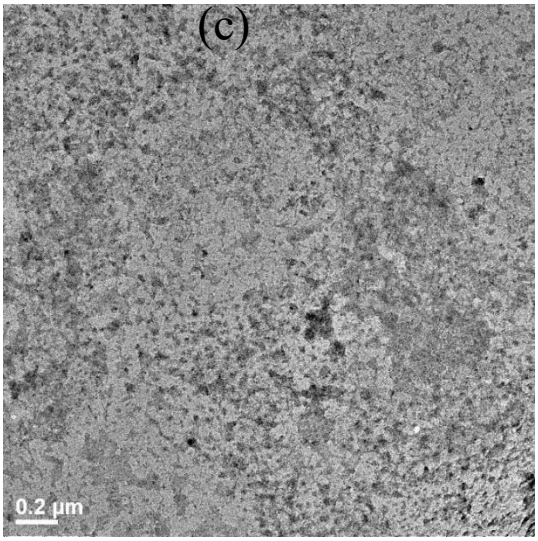

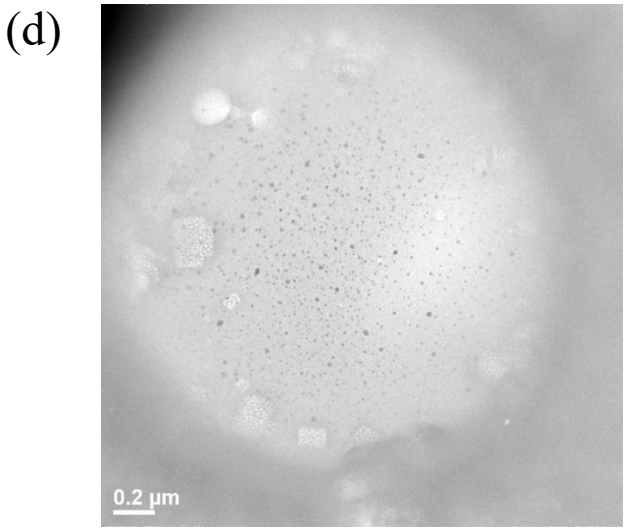

Figure 4.18: (a) Table of EDX quantitative results showing elemental weight and atomic percentages of untreated, 10, 60 min UV-treated NGQDs. Representative scan area for the EDX measurements of (b) untreated, (c) 10 min, (d) 60 min UV-treated NGQDs sample.

These UV wavelength-dependent alterations of GQD optical and structural properties suggest that such wavelength-dependent sensitivity could be utilized for UV detection by GQDs. This leads us to fabricate UV photodetectors utilizing 0, 30, 60 min UV-treated NGQDs as a photosensing layer. A silicon wafer of 24X12 (LXW) mm coated with a 160 nm SiO_2 layer is used as a substrate onto which 50 nm gold (Au) electrodes are deposited to serve as anode and cathode on the far sides of the substrate. This keeps 2X12 (LXW) mm space in the middle of the substrate as a device channel for drop-coating the solution-processed NGQDs (Figure 4.19b, 4.20). Drop-casted NGQDs are thermally annealed at 90°C for 20 min to evaporate the water. Figure 4.19a represents the schematic of the fabricated device that illustrates the device geometry envisioned based on the cross-sectional image of the photodetector captured by field-emission scanning electron microscope (FESEM). It shows a uniformly deposited ~2 μm layer of NGQDs and a 160 nm SiO_2 layer (Figure 4.19b). Additionally, the EDX mapping of this SEM cross-sectional image verifies the presence of layer-wise elemental composition showing Si/SiO_2 substrate in the bottom part and NGQD layer containing oxygen/nitrogen/carbon in the top part (Figure 4.20). Based on the known work function values of the gold electrodes (5.1 eV)[154] and Fermi level of the similar GQDs (4.74 eV) independent of GQD size (~2 to 10 nm) assessed *via* Kelvin probe analysis by Kwon et al[90], we design a schematic of the energy band diagram of the UV photodetector (Figure 4.19c). In the energy band diagram, the values of HOMO (highest occupied molecular orbital) as 6.23 eV and LUMO (lowest unoccupied molecular orbital) as 3.25 eV are calculated with the knowledge of Fermi energy utilizing the maximum emission wavelength. Based on the diagram the potential energy barrier of ~1.13 eV is expected in the junction of the metallic gold electrode and NGQDs. Excitons would be generated in NGQDs layer under 254/302/365 nm ultraviolet light

irradiation having energies higher than the optical band gap of the NGQDs. With small bias voltage, the electron-hole pairs may get dissociated at the NGQDs interface potentially due to the edge defects and defect-related trap-states of NGQDs, and the additional surface potential originated from adsorbed water/oxygen molecules. Therefore, the movement of the electrons and holes will be initiated toward the anode and cathode, respectively, producing the photocurrent under a built-in electric field. Small dark leakage current is observed *via* the typical current-voltage (I-V) characteristics (Figure 4.19d,e) of the device acquired by sweeping from -5 to +5 V potentially attributed to the thermionic emission at room temperature[155]. However, with 254/302/365 nm UV exposure, still a significant increase of the current is observed as expected, suggesting the successful generation of the photocurrent.

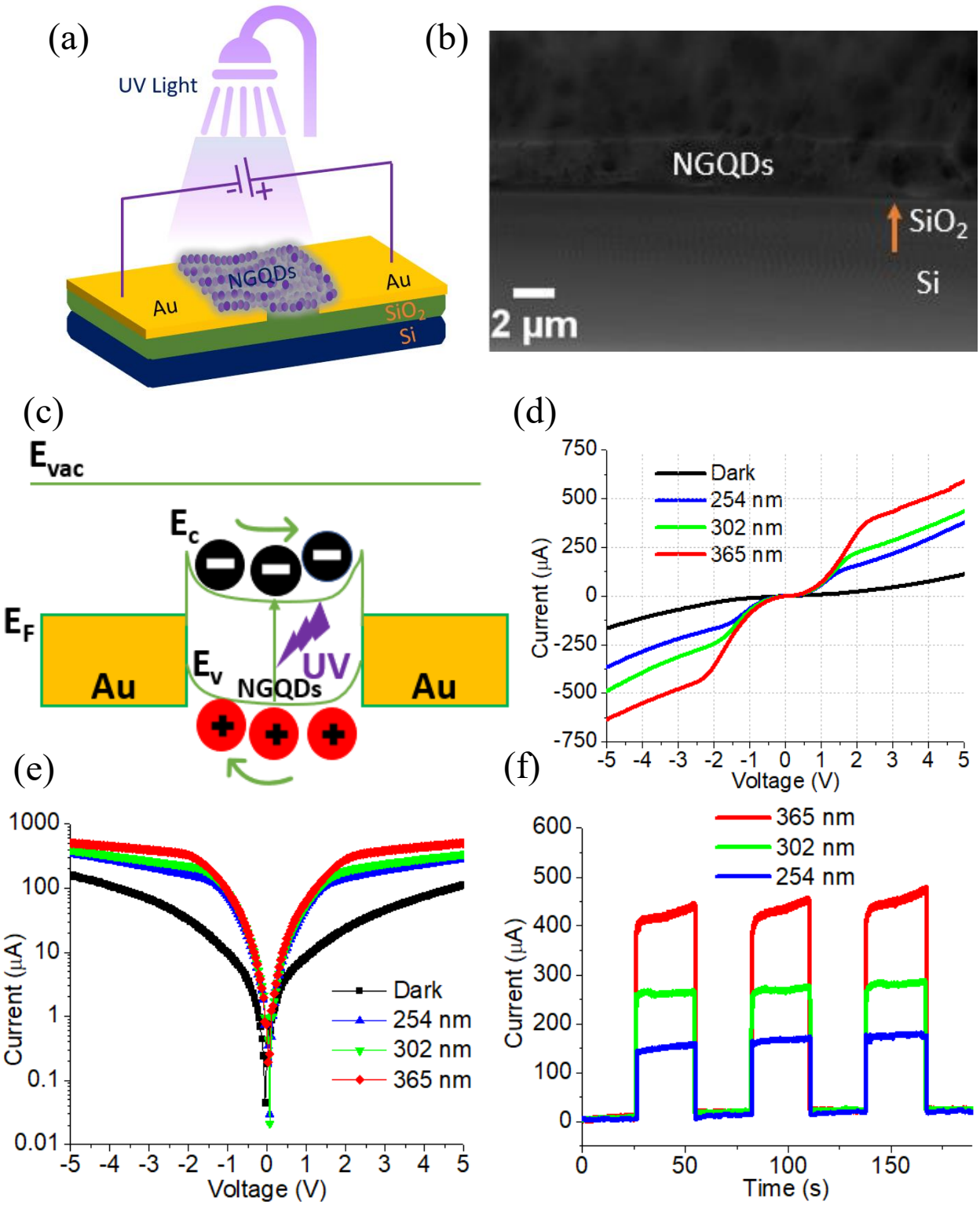

Figure 4.19: (a) Schematic of the UV photodetector device structure, (b) SEM Cross-section of the device, (c) Band energy diagram of the photodetector, (d) I-V characteristics of the fabricated device sweeping from -5 to 5 V, (e) semi-logarithmic plot of I-V curve and (f) stable and reproducible photo-switching response of the UV photodetector.

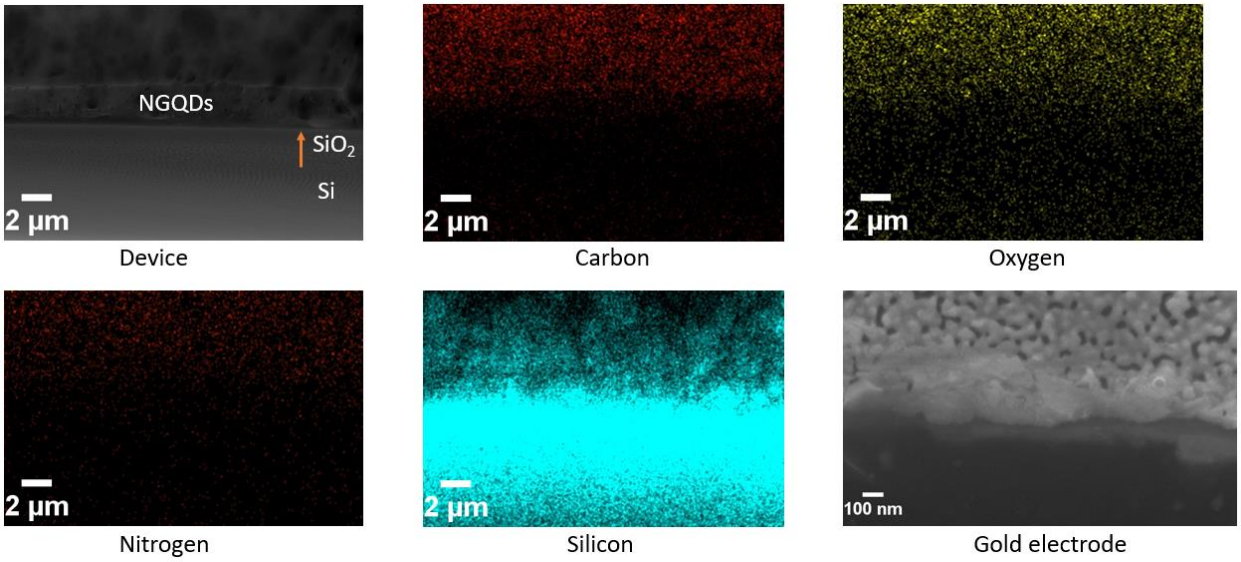

Figure 4.20: SEM cross-section image of the device showing Si/SiO_2/NGQDs layer and the corresponding layer-based (element-wise) EDX mapping data of carbon, oxygen, nitrogen and silicon. Bottom right: cross-section image of the device showing 50 nm thick gold electrode.

The lowest/highest photocurrent of ~150/~475 µA is obtained from the device fabricated with untreated (0 min) NGQDs as a photo-sensing layer at 5V bias voltage with 254/365 nm UV excitation (Figure 4.19f). Regardless of the current magnitude, the device shows reproducible characteristics of UV photodetectors. The maximum photocurrent generation is observed with 365 nm UV irradiation as compared to the 254/302 nm excitation which can be ascribed to the lower NGQD absorption of 254/302 nm UV light (Figure 4.2a,4.3a) as compared to no significant absorption in 365 nm range (Figure 4.5a). Moreover, we observe a much higher light to the dark current ratio (I_L/I_D) at a lower than higher bias voltage along with a non-linear dependence of I_L/I_D on bias voltage potentially due to the generation of more leakage current with the increase of bias voltage resulting in a decrease of the light to dark current ratio (Figure 4.21e).

The devices were tested further at 5V bias voltage with subsequent irradiation of 3 different wavelengths (365/302/254) followed by measurement under room light/dark conditions showing UV wavelength-dependent response with no effect in the room light or dark conditions (Figure 4.21a) suggesting excellent reproducibility and multiwavelength sensitivity. Also, the rise and decay response time of the UV photodetector analyzed using the fitting equations described in [156] providing a rise times of 96, 87 and 38 ms and fall times of 73, 119 and 74 ms considering 30s periodic irradiation with 365 nm, 302 nm, and 254 nm illumination respectively (Figure 4.21b,c,d) suggesting rapid photo-switching characteristics. These rise/decay times appear to be reproducible, as are the signal currents achieved for each wavelength.

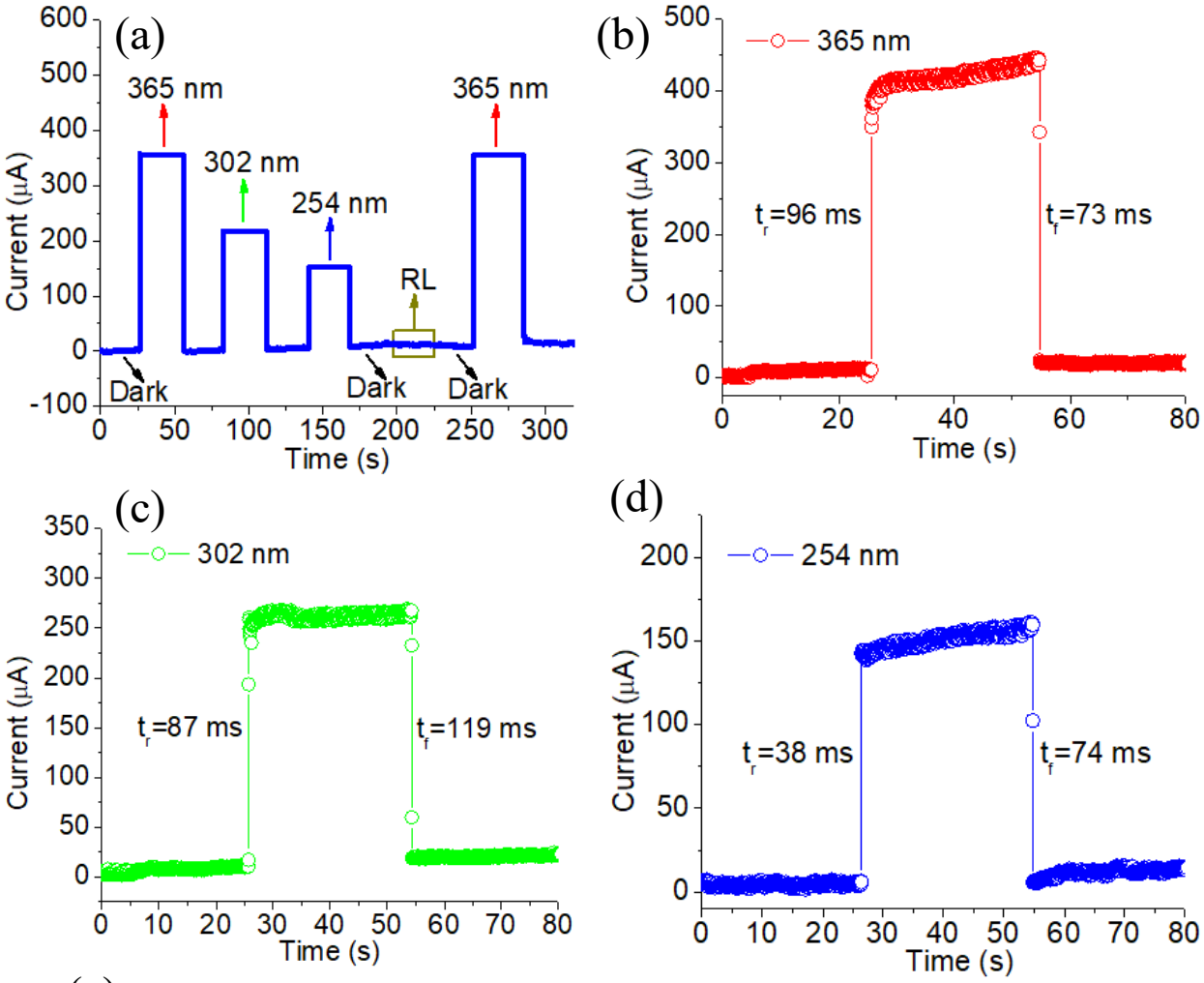

(e)

Bias voltage (V)	I_L/I_D (UVT-365)	I_L/I_D (UVT-302)	I_L/I_D (UVT-254)
1.50	12.70	8.50	8.45
1.75	13.10	10.65	7.60
2.00	14.10	9.50	6.70
5.00	5.20	3.85	3.35

Figure 4.21: (a) Photo-switching response of the device under dark/RL (room light) conditions and 365/302/254 nm UV illumination. Rise and fall time of the photo response illuminated with (b) 365 nm, (c) 302 nm, (d) 254 nm UV light, (e) Table of light to the dark current ratio (I_L/I_D) at different bias voltage.

We further compare the typical I-V characteristics, photo-switching behavior, and device parameters among the photodetectors fabricated with 0, 30 and 60 min UV-treated NGQDs as a photosensing layer. Those indicate a considerable (by a factor of ~1.38) increase of photocurrent with 365 nm UV light irradiation for the devices with 60 min UV treated NGQDs as compared to the untreated N-GQD-based devices (Figure 4.22a,b,c). The increase of photocurrent can be potentially attributed to the increasing/broadening of NGQDs absorbance intensity at ~365 nm (Figure 4.3a) with the increase of UV treatment time, leading to the absorption of more photons which allows producing higher photocurrent. On the other hand, with 302 nm UV excitation only a slight increase in photocurrent (~1.06 times) is observed for the devices made with 0 to 30 min UV treated NGQDs, while a significant decrease in photocurrent (~1.45 times) is seen for 30 to 60 min UV-treated NGQD-based devices (Figure 9d,e,f) (Figure 4.22d,e,f). Moreover, under 254 nm UV illumination, a gradual decrease of the photocurrent is observed for all the devices fabricated (Figure 4.22g,h,i). This observed decrease of photocurrent with 254/302 nm UV excitation can be explained by the significant decrease of GQD absorbance intensity as those are treated with short/mid-wave UV(Figure 4.3a).

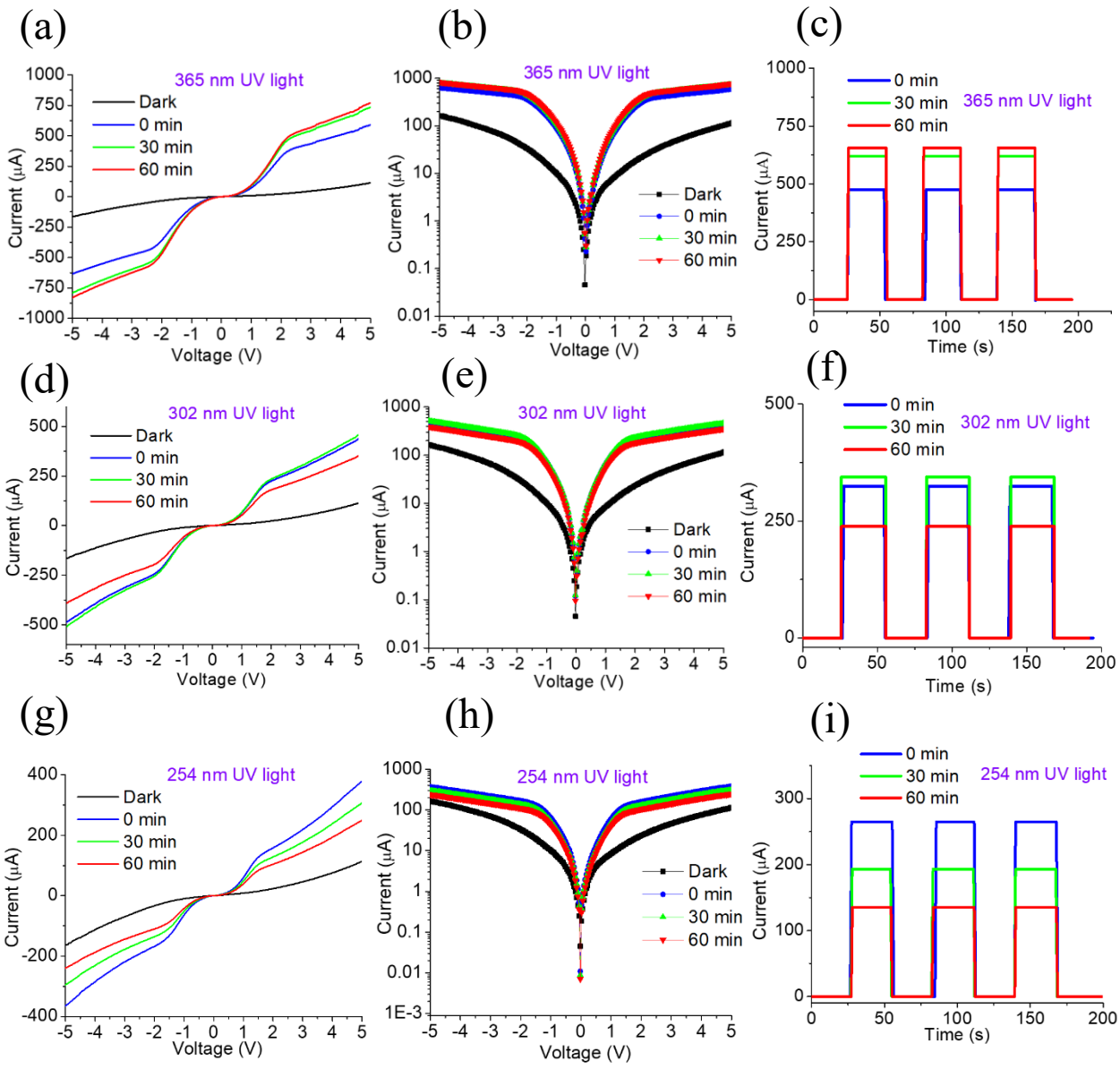

Figure 4.22: (a) I-V characteristics (sweeping from -5 to 5 V), (b) corresponding semi-logarithmic plot of I-V curve, (c) stable and reproducible photo-switching response (5V bias) of the devices fabricated with 0, 30, 60 min UV treated NGQDs under 365 nm UV irradiation ; (d) I-V characteristics (sweeping from -5 to 5 V), (e) corresponding semi-logarithmic plot of I-V curve, (f) stable and reproducible photo-switching response (5V bias) of the devices fabricated with 0, 30, 60 min UV treated NGQDs under 302 nm UV irradiation; (g) I-V characteristics (sweeping from -5 to 5 V), (h) corresponding semi-logarithmic plot of I-V curve, (i) stable and reproducible photo-switching response (5 V bias) of the devices fabricated with 0, 30, 60 min UV treated NGQDs under 254 nm UV irradiation.

Since responsivity (R), detectivity (D), and EQE (External Quantum Efficiency) are considered as three main parameters of a photodetector which define the quality and efficiency of the device, those are calculated in accordance with previous works[156-159] by using the following equations:

Photo-responsivity:

Responsivity can be expressed as:

$$R = \frac{I_{pc}}{I_{inc}} = \frac{Photogenerated\ current}{Incident\ power\ density\ \times Area\ of\ Active\ region}$$

Here, R=responsivity (Unit: A/W)

I_{pc} = Photogenerated current (Unit: A)

I_{inc} = Incident power intensity (Unit: W) = Incident power density X Area of the active region

Photo-detectivity:

Detectivity can be expressed as:

$$D = R\sqrt{\frac{A}{2 \times q \times I_d}}$$

Here,

D=Detectivity in Jones

R=responsivity in A/W

A=Area of the active region in cm^2

q = Charge of electron = $1.60X10^{-19}$ C

I_d = Dark current (under no illumination)

EQE (External Quantum Efficiency):

EQE can be defined as the number of carriers circulating through a photodetector per absorbed photon and per unit time. EQE can be calculated by using the following equation:

$$EQE = \frac{h \times c \times I_{pc}}{q \times \lambda \times I_{inc}} = \frac{(\sim 1243) \times R}{\lambda}$$

Here,

h=Planck's constant= ~ $6.63X10^{-34}$ J.s

c=Velocity of light=$3X10^{8}$ m/s

q = Charge of electron = $1.60X10^{-19}$ C

$R = \frac{I_{pc}}{I_{inc}}$ = Responsivity in A/W

$\frac{h \times c}{q} = \sim 1243$ ($Conversion\ of\ 1\ nm\ to\ 1 \times 10^{-9}\ m\ is\ included\ in\ this\ factor$)

λ=Excitation wavelength

This calculation provides maximum responsivities of 0.59, 0.31 and 0.22 A/W, detectivities of $1.03X10^{11}$, $5.48X10^{10}$ and $3.90X10^{10}$ Jones, and EQE of $2X10^{2}$, $1.24X10^{2}$, and $9.38X10^{1}$ % under the irradiation of 365, 302 and 254 nm UV light respectively at 2V bias, indicating highly responsive characteristics of the devices fabricated in this work. Additionally, the responsivity (Figure 4.23a), detectivity (Figure 4.32b), and EQE (Figure 4.32c) of the devices fabricated with 0, 30, 60 min UV-treated NGQDs tested under 254/302/365 nm UV excitation are plotted, showing the comparison of device parameters at different UV excitation and treatment times.

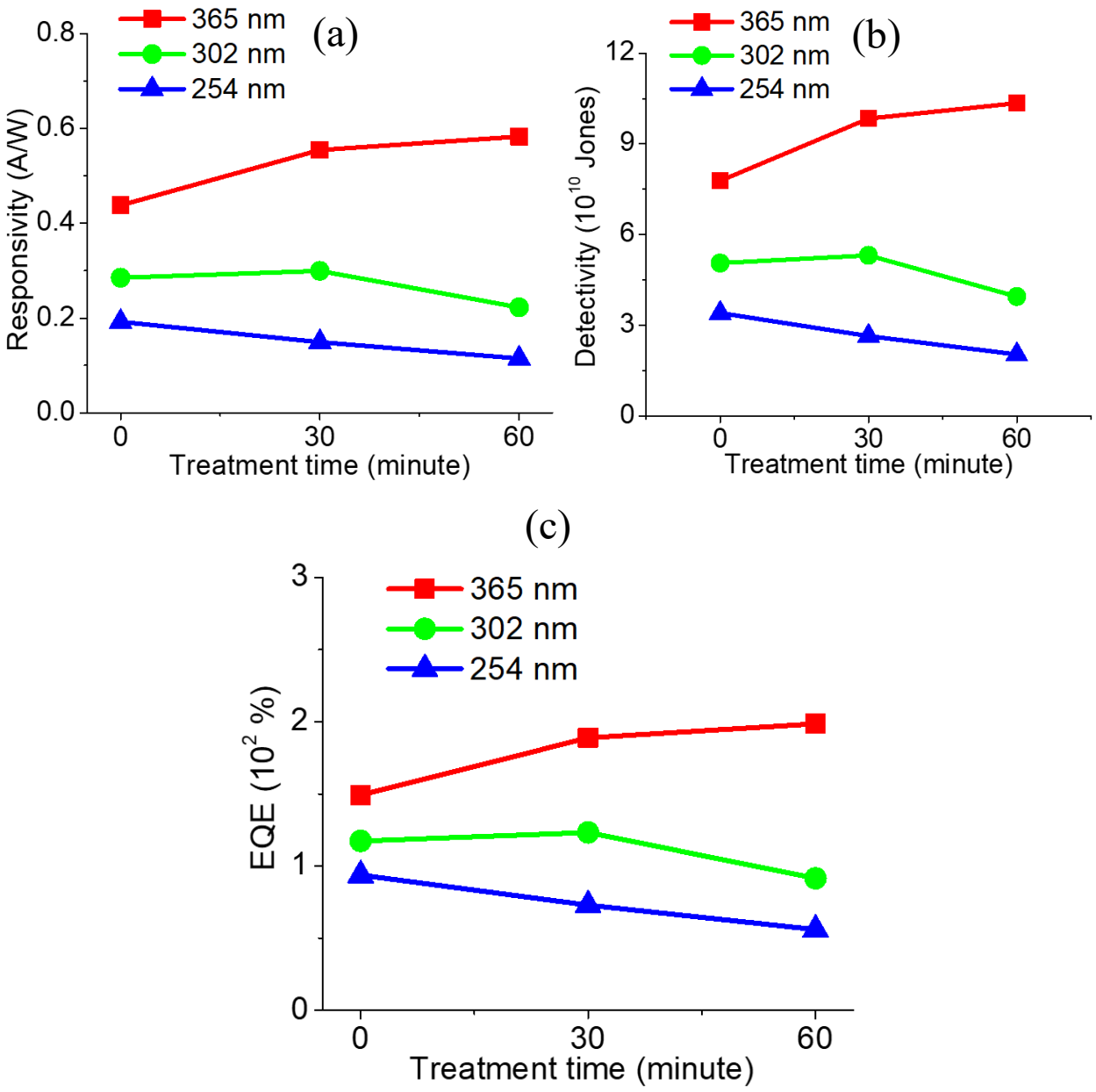

Figure 4.23: Comparison of device parameters among UV photodetectors fabricated with 0, 30, 60 min UV-treated NGQDs sample showing (a) responsivity, (b) detectivity, and (c) EQE under 365/302/254 nm UV excitation.

Evidently, maximum performance (responsivity/detectivity/EQE) in the longwave UV region can be achieved from the 60 min UV-treated NGQD-based devices with 365 nm UV excitation whereas untreated NGQDs are more suitable to obtain maximum performance in the short/mid-wave UV region with 254/302 nm excitation. Although it is hard to compare the performance of these devices with others due to the differences in device geometry/electrodes/types of materials, these calculated parameters are still well-comparable to the previously reported graphene quantum dot-based devices (Table-1), which in combination with eco-friendly/simple/scalable fabrication process makes NGQD-based UV photodetector developed in this work a promising optoelectronic solution. To be ahead of the counterparts, the device performance obtained in this work can be potentially enhanced further by decreasing the channel length from millimeter to micron-scale which may lead to more efficient carrier transport and much faster photoswitching behavior[154, 160].

Table-4.1: Comparison of device parameters fabricated with GQDs/NGQDs/carbon-based nanoparticles:

Material	Detection Range	Responsivity	Detectivity (Jones)	EQE (%)	References
CQDs	400-1100 nm	0.353 (A/W)	$>10^9$	-	[161]
NGQDs	365 nm	1.14 (V/W)	-	-	[162]
GQDs	UV/NIR	(0.2-0.5) A/W	$> 10^{11}$	-	[163]
CNDs	300-1100 nm	0.5 A/W	$> 10^{14}$	-	[164]
GQDs	DUV	0.1 A/W	$1.1X10^{13}$		[165]
RGO/CNPs	780 nm	0.4 A/W	-	$6.43X10^1$	[166]
CQDs	VIS	0.29 A/W	-	-	[167]
2D MoS2/CQDs	UV/VIS/NIR	0.018 A/W	-	-	[168]
GQDs decorated ZnO Nanorods/GaN Films	365 nm	0.034 A/W	$\sim10^{12}$	-	[169]
NGQDs	DUV (Au-GQDs-Au configuration)	$4.26X10^{-6}$ (A/W)	$1.95X10^9$	-	[154]
GQDs/WSe2	VIS/NIR	0.70 A/W	$4.51X10^9$	-	[170]
GQDs/SiNP	UV/NIR	0.31 A/W	-	-	[171]
GQDs/Si	VIS	1.02 A/W	$8X10^{11}$	-	[172]
GQDs/SiNW	UV/NIR	40.6 A/W	$11.9X10^{12}$	$8.15X10^3$	[173]
NGQDs	DUV/UV	0.59 (A/W)	$1.03X10^{11}$	$2X10^2$	Our Work

List of abbreviations for table-1:

CQDs: Carbon Quantum Dots; CNDs: Carbon Nanodots; DUV: Deep ultra-violet light; CNPs: Carbon nanoparticles; MoS_2: Molybdenum disulfide; ZnO: Zinc Oxide; GaN: Gallium Nitride; SiNP: Silicon Nanoparticle; SiNW: Silicon Nanowire

4.4 Summary of chapter-4:

In this chapter, an eco-friendly microwave-facilitated scalable hydrothermal method is used to produce NGQDs showing bright/stable photoluminescence in the visible and near-IR that are further utilized for the development of UV photodetectors. An extensive study is undertaken in order to assess the change in the optical properties of as-prepared NGQDs under short/mid/long wave UV irradiation. NGQDs irradiated with 254/302 nm UV light over 0 to 60 min exhibit a significant reduction in absorption, while 365 nm UV-irradiated NGQDs retain their spectral characteristics. All three UV ranges affect NGQD fluorescence inducing a gradual decrease in emission intensity recorded with 350, 400 and 730 nm excitation. However, a remarkable (~90 fold) increase in fluorescence intensity with 500 nm excitation is observed for NGQDs treated with 254 and 302 nm UV light. Considering the size-dependence of NGQD band gaps, these changes in optical properties can be attributed to the alteration of NGQD size distribution and the reduction in oxygen-containing functional groups. The observed redshift of the emission from blue to yellow with the dramatic enhancement of the yellow fluorescence feature detected with 500 nm excitation is likely to occur due to UV-induced NGQD polymerization increasing NGQD average size from 4.70±0.05 nm (untreated) to 11.20±0.35 nm (60 min UV irradiation). A significant reduction of the oxygen-containing functional groups detected *via* FTIR reveals the reason behind the quenching of the defect-attributed NGQD emission in the near-IR. Due to the high sensitivity to UV radiation, NGQDs developed in this work are utilized as a photosensitive layer in the novel UV photodetector devices. These devices show stable/reproducible photo-switching behavior at a low bias voltage under 254/302/365 nm UV illumination with high responsivity (up to 0.59 A/W) and detectivity (up to $1.03X10^{11}$ Jones) sufficient to fabricate highly sensitive UV photodetectors

(UVPD). Wavelength-specific highly reproducible response with no reaction to the visible light sets these UV photodetectors ahead of many other nanomaterials-based counterparts.

CHAPTER 5

Near-IR Emitting Graphene Quantum Dots Synthesized *via* Top-down Approach for Biological Imaging Applications

5.1 Overview:

Nanomaterials-based nano-formulations are getting more attention in recent years for drug/gene delivery and bioimaging applications due to their ability to effectively deliver therapeutic to biological cells and tissues, enhancing their efficacy and rendering some more biocompatibility. Nanomaterials provide a large platform for covalent/non-covalent functionalization of both drugs and targeting agents and often enable fluorescence tracking yielding a multifunctional alternative facilitating drug transport, biological imaging, and even biosensing. Most of the nanomaterials have high production costs, complex synthesis procedures, and as for fluorescence tracking, exhibit emission only in visible with UV/VIS excitation which suffers from high autofluorescence background from biological specimen and due to absorption and scattering has low penetration depth suitable only for *in vitro* applications. *In vivo* imaging usually requires attaching either MRI[174] or CT contrast agents[175] that add to the toxicity profile of the formulation[176]. There are some nanomaterials such as single-walled carbon nanotubes (SWCNTs) that are known to exhibit emission in the NIR-I/II region. The emission in this range yields a broader spectrum of potential applications as NIR light experiences substantially lower scattering and absorption in tissues, while the biological autofluorescence in that region is minimal[177] (Figure 5.1). Such NIR emissive nanomaterials can be utilized even for low/medium depth in vivo applications.

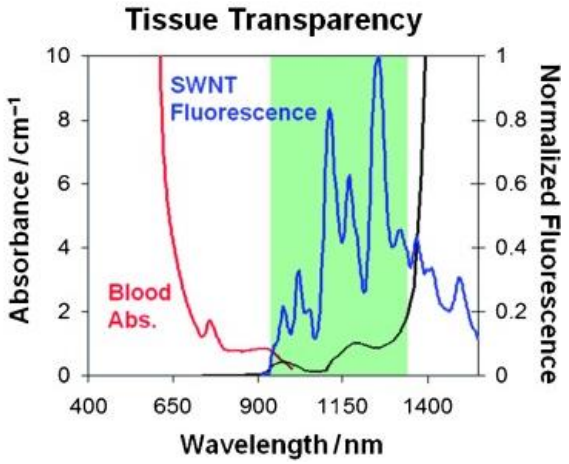

Figure 5.1: Photoluminescence of NIR emitting nanomaterials (SWCNTs) (blue) in 820–1600 nm regime, Absorbance of Blood (red) and water (black) mainly occur in the visible and infrared regions, respectively. The gap in tissue absorbance, which occurs in the near-infrared regime, ensures minimal tissue interference with NIR emitting nanomaterials. [177]

However, SWCNTs' biocompatibility is highly dependent on the coating and in some formulations they may lead to potential immunogenic responses and accumulation-derived toxicity[178], which is not ideal for the therapeutic delivery. NIR I/II emitting quantum dots such as PbS/CdS/CdSe[179-181] can also be used for *in-vitro/in-vivo* NIR fluorescence tracking, but their complex synthesis process along with detrimental effects on the environment and biotoxicity make them unsuitable for large scale biological imaging applications. Therefore, it is highly important to develop materials that will have low production costs, high production yield, simple/scalable synthesis process, excellent water solubility, and high biocompatibility. Moreover, these desired materials are expected to exhibit emission in the NIR region for bioimaging applications reducing autofluorescence background, possess large enough platform to attach drugs/genes for therapeutics, quickly accumulate in the targeted area followed by a fast excretion from the biological subject. In order to achieve these, we have worked on developing the material that would satisfy the aforementioned conditions: reduced graphene oxide (RGO)-derived graphene quantum dots (RGQDs) synthesized *via* top-down method using RGO as a carbon precursor and NaOCl

together with UV irradiation as scission/oxidizing treatments. To the best of our knowledge, this is the first-time discovery of NIR-emitting RGQDs (graphene quantum dots synthesized from RGO) produced via top-down method using RGO/NaOCl/UV light. These GQDs prepared via a simple and low cost/scalable synthetic route possess high biocompatibility, exhibit emission in the NIR I region and are in our work successfully utilized for *in vitro* and *in vivo* imaging in live animals.

5.2 Experimental Methods and Procedures:

5.2.1 *Synthesis of graphene quantum dots from reduced graphene oxide via a top-down approach:*

Commercially available high porosity reduced graphene oxide (RGO) (purchased from graphene supermarket, HP-RGO-0.5G) was suspended into water at a concentration of 0.20 mg/ml *via* direct probe ultrasonic treatment (QSonica, Q55) under ice-bath condition for one hour at 22 W. 1.5 ml of 5% w/v sodium hypochlorite (NaClO, CAS 7681-52-9) was mixed in 20 ml aqueous RGO suspension followed by two hours of ultraviolet (UV) irradiation at 302 nm utilizing a benchtop 3UV transilluminator (LMS-20, 8W) UV source. The NaClO will decompose at a higher rate under UV irradiation generating oxygen radicals [O] which are expected to react with the RGO surface facilitating its scission and oxidation into graphene quantum dots (RGQDs). These RGQDs were dialyzed in DI water using a molecular-weight-cutoff (MWCO) 1KDa bag for 24h in order to remove sodium ions and other low molecular weight unreacted materials. The DI water was changed every after 30 min for the first three hours followed by changing the water every seven hours. The dialyzed RGQDs were then further filtered using a 0.22 µm syringe filter to discard the bundles/large clusters of RGQDs.

5.2.2 *Structural/Optical Characterization:*

The morphological characterization of the RGQDs was performed using HRTEM (High-Resolution Transmission Electron Microscope, JEOL JEM-2100). For the TEM measurements, the samples were prepared on the carbon-coated 200-mesh copper grid under ambient conditions. The photoluminescence spectra of RGQDs were measured utilizing Horiba Scientific SPEX NanoLog. The absorbance of RGQDs samples was measured within the range of 200-1000 nm using Agilent Technologies (Cary 60 UV–vis) absorption spectrometer. RGQDs' graphitic structure was characterized using a DeltaNu Raman spectrometer with 785 nm excitation at 100 mW maximum power. The absolute quantum yield of the RGQDs was determined using a Newport 819C-SL integrating sphere (Spectralon coating) at 405, 637, and 808 nm laser excitation

5.2.3 *Cell Culture:*

HeLa cell lines were maintained in a Thermo-Scientific Midi 40 CO_2 Incubator at 37.1 °C with 5% carbon dioxide and 95% air. In order to prepare the cell-covered glass coverslips for microscopy imaging, they were placed at the bottom of 6-well plates followed by adding cells in the media. RGQDs were added at a concentration of 1 mg/mL in each well after 4 hours of cell attachment to the coverslips. 0.5 mL of PBS (phosphate-buffered saline) was used to wash the cells in order to remove any extracellular RGQDs, followed by fixing them with 4% paraformaldehyde at room temperature for 30 min. After that, the cell samples were washed again with 0.5 mL of PBS for the microscopy imaging. In order to analyze RGQD cellular internalization, the 3, 6, 12 and 24 h transfection points were used for imaging with 1 mg/mL of RGQDs added to each well.

5.2.4 *MTT Assays:*

MTT cytotoxicity assays were used to assess the cytotoxicity of RGQDs. We plated HeLa cells in a 96-well plate with 5000 cells per well (100 µL/well) and kept in an incubator overnight at 37.1 °C while maintaining the CO_2/air ratio of 1:19. After 24 h of incubation, the RGQDs were added into each well at different concentrations ranging from 0 to 70 µg/mL. After 24 h of incubation, the medium was replaced by 100 µL of 1 mg/mL thiazolyl blue tetrazolium bromide. After four hours of further incubation, MTT (3-(4–dimethylthiazol-2-yl)-2,5-diphenyltetrazolium bromide) was replaced with 100 µL of DMSO (dimethyl sulfoxide) to solubilize the precipitation. Reduction in MTT influences the metabolic activity of living cells, which can be assessed with absorbance measurements since living cells metabolize the MTT and form a highly absorbing purple-colored byproduct known as formazan. We measured the absorbance (essentially the cell viability) of the final sample at 540 nm wavelength using the FLUOstar Omega microplate reader.

5.2.5 *Fluorescence microscopy measurements*

In vitro fluorescence microscopy of RGQDs was performed using an Olympus IX73 fluorescence microscope with 60× (IR-corrected Olympus Plan Apo) water immersion objective coupled to two detectors: visible Hamamatsu Image EMCCD camera spectrally filtered by 10 filters throughout the visible and the NIR InGaAs Photon etc. (ZEPHIR^{TM} 1.7) camera connected to a hyperspectral fluorescence imager (Photon etc.) enabling spectrally-resolved imaging in the near-infrared: 900 – 1600 nm.

5.2.6 *Imaging in the visible*

Intracellular green (~532 nm) emission of RGQDs was measured with 460 ± 25 nm (lamp) excitation and 550 ± 20 nm emission filters. The integration time and lamp intensity settings were

chosen such to ensure zero autofluorescence emission from non-treatment control cells and the same settings were further used for RGQDs fluorescence imaging.

5.2.7 *Imaging in NIR region*

The NIR-I fluorescence of RGQDs was imaged with CW (continuous wave) 808 nm (150 mW output power) diode laser excitation in HeLa cells with InGaAs Photon etc. (ZEPHIR^{TM} 1.7) camera and near-IR hyperspectral imager (Photon etc. IMA-IR^{TM}) allowing to capture full spatial information and simultaneously utilize a Bragg grating imaging filter[182] collecting spectral information thus providing spectrally-resolved imaging in the region of 900 – 1600 nm. Control cell samples without RGQDs imaged with the same setup showed no emission in the near-IR region.

5.3 Results and discussion:

A top-down approach is utilized to produce nanometer-sized GQDs from commercially available over micron-sized RGO (Figure 5.2a,b). Upon adding sodium hypochlorite (NaOCl) into aqueous RGO, the decomposition of NaOCl takes place followed by the generation of highly oxidative free radical [$O^{\cdot}$]. The reaction rate can be increased significantly upon the irradiation of ultraviolet (UV) light since high energy UV illumination expedites the decomposition of NaOCl[183] yielding a higher number of free radicals [$O^{\cdot}$] at a much faster rate. As RGO is a reduced form of graphene oxide (GO), in the place of reduced GO oxygen functional groups RGO is expected to have a number of defects, which are likely to be the most favorable regions for the reaction. In the process of this chemical reaction, RGO surface oxidation cutting takes place yielding smaller-sized nicely dispersed, and well-distributed GQDs (Figure 5.2c,d) with an average diameter of 3.54±0.05 nm (Figure 5.2e) as assessed by high-resolution transmission

electron microscopy (HRTEM). GQDs also exhibit a well-defined crystalline lattice structure apparent from FFT (fast Fourier transform) images of the chosen area (Figure 5.2f,g) along with distinguishable lattice fringes with a spacing of 0.24 nm (Figure 5.2h) corresponding to graphite[184]. EDX (Energy-dispersive X-ray Spectroscopy) measurements performed with RGQDs and RGO parent material show a significant decrease of carbon atomic percentage from 97.76% (RGO) to 83% (RGQDs) and substantial increase of oxygen atomic percentage from 2.24% (RGO) to 17% (RGQDs) as assessed via elemental analysis (Figure 5.3a, 5.4a) along with elemental mapping of the scan area (Figure 5.3b,c,d and Figure 5.4b,c,d).

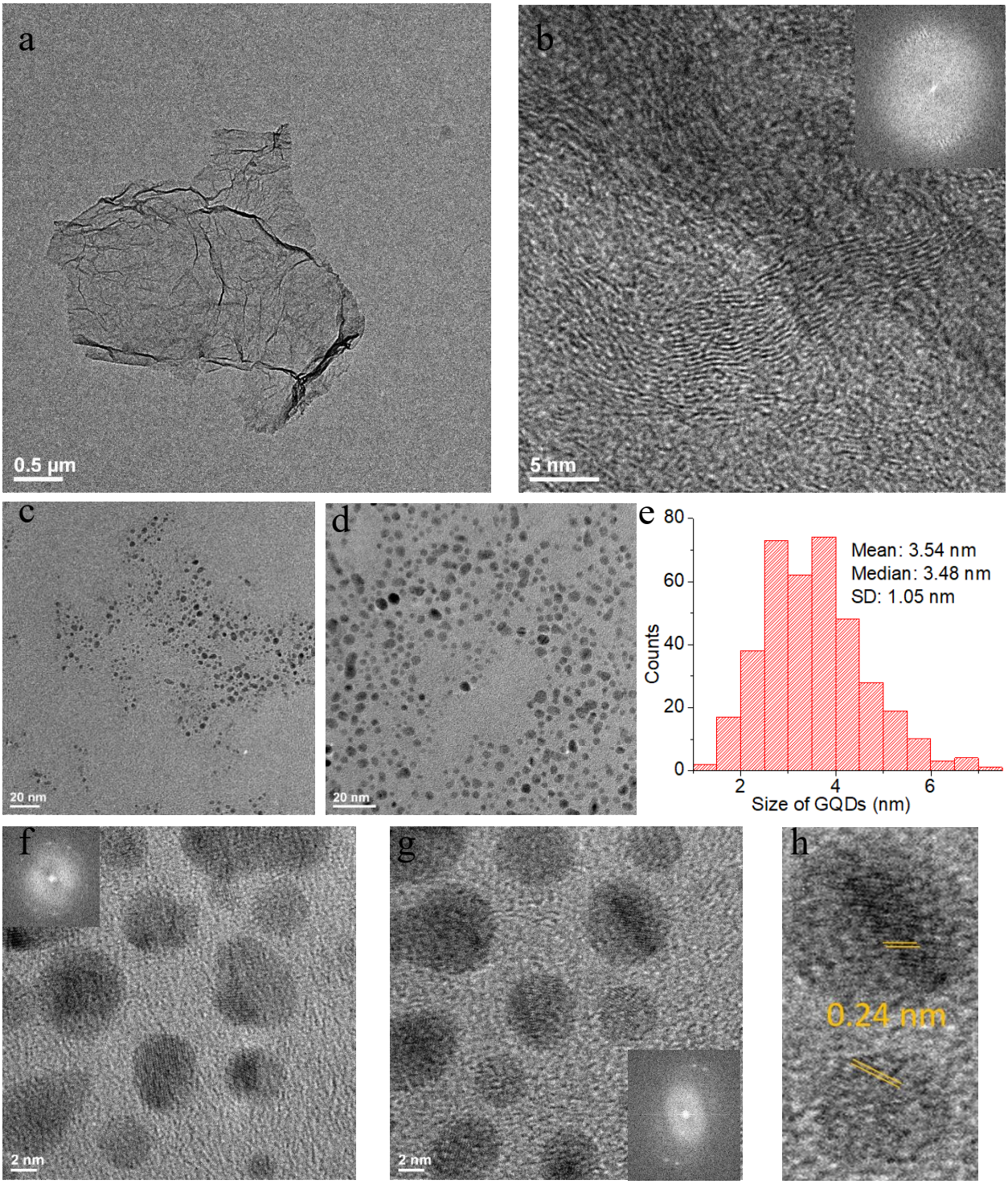

Figure 5.2: (a) TEM images of more than micron sized RGO (b) HRTEM images of RGO. Inset: FFT images of the chosen area. (c,d) TEM images showing the distribution of RGQDS, (e) Size distribution of RGQDs. (f,g) HRTEM images of RGQDs. Inset: FFT images of the chosen area (h) Separation between lattice fringes.

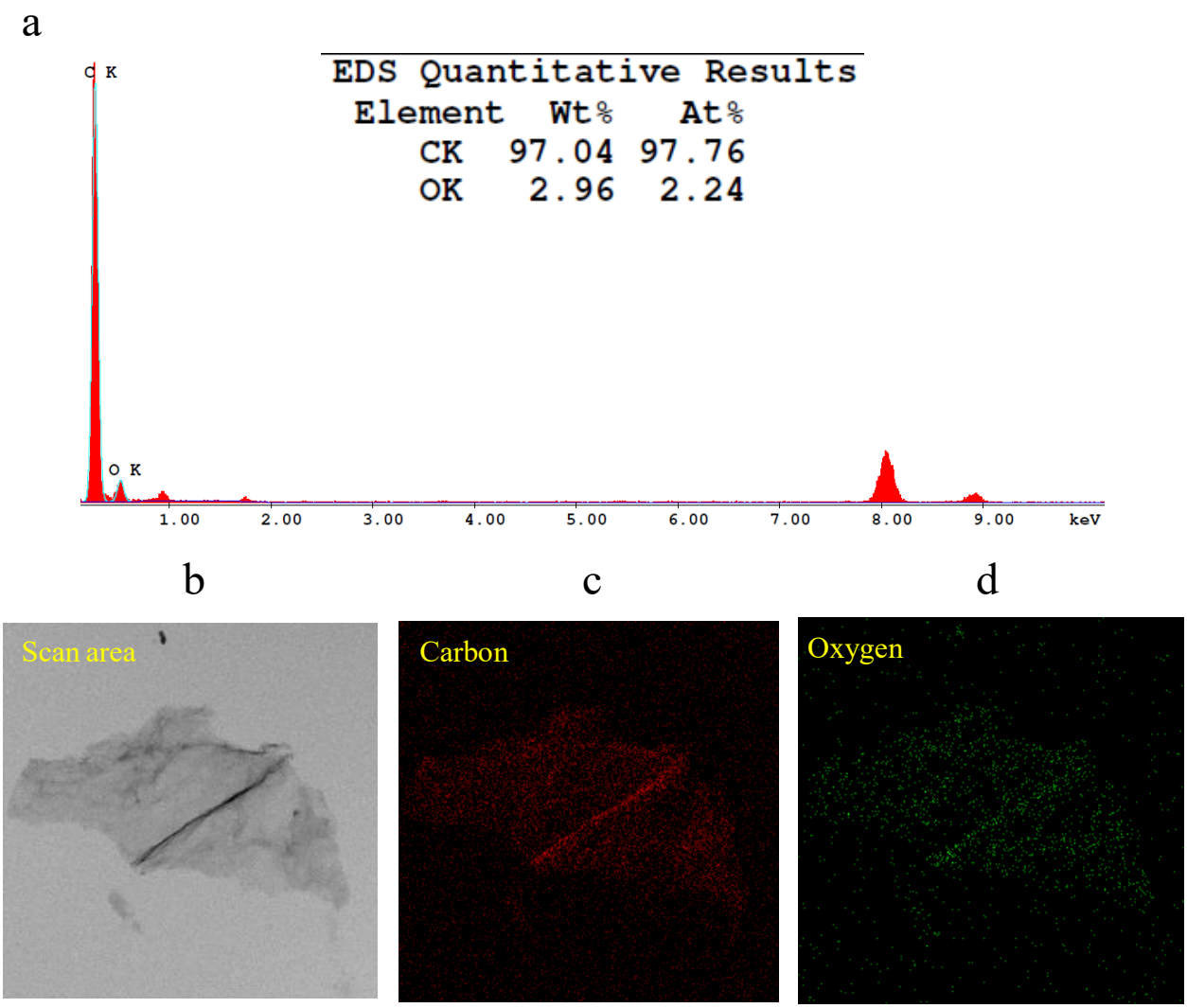

Figure 5.3: (a) EDX spectra of RGO. Inset: Atomic/weight percentage of Carbon and Oxygen. EDX mapping of RGO showing (b) scan area, the presence of (c) Carbon, (d) Oxygen.

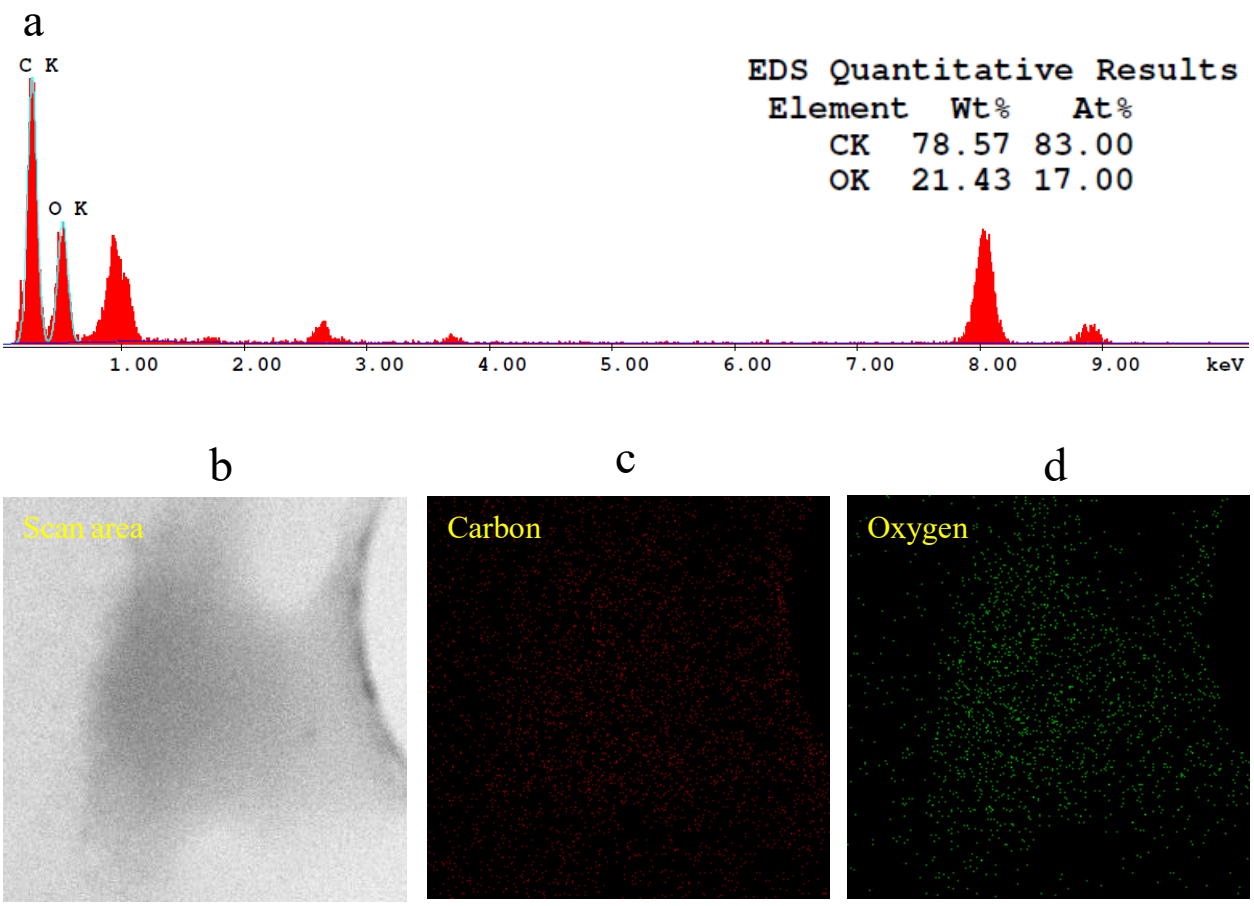

Figure 5.4: (a) EDX spectra of RGQDs. Inset: Atomic/weight percentage of Carbon and Oxygen. EDX mapping of RGQDs showing (b) scan area, the presence of (c) Carbon, (d) Oxygen.

Additionally, Raman spectroscopic measurements show the D-band at ~1330 cm^{-1} indicating the presence of disordered structure and G-band at ~1604 cm^{-1} (Figure 5.5a,b) corresponding to the SP^2 hybridized carbons on the surface of both RGO and RGQDs. The I_D/I_G ratio increased from ~1.50 (RGO) to ~1.74 (RGQDs) (1.16 times), suggesting the increase of defects in the RGQDs graphitic structure induced scission and oxidation in the synthetic process.

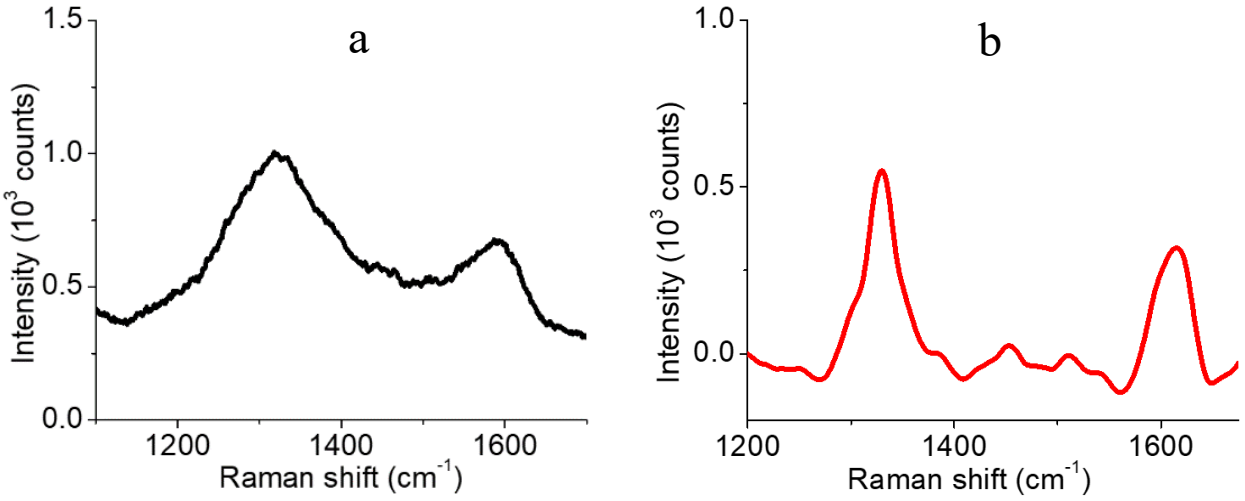

Figure 5.5: Raman spectra of (a) RGO, (b) RGQDs.

A dramatic change in color and solubility of the material was observed before and after the reaction (Figure 5.6a) indicating a substantial change in electronic and chemical structure. New oxo-functionalized RGQDs possess light yellow color in suspension and show high water suspension stability as opposed to water-insoluble and dark black/grey RGO. In order to verify those changes, the optical properties of RGO/RGQDs are explored using fluorescence and absorption spectroscopy. RGO shows an absorption peak at ~280 nm corresponding to π to π^* transition of SP^2 graphitic carbon (Figure 5.6b) whereas a blue-shifted peak at ~230 nm appears for RGQDs which is more similar to the π to π^* transition of C=C bonds in graphene oxide (GO). However, GO has a shoulder ~300 nm corresponding to C=O bond which is absent in RGQDs suggesting different types/arrangements of oxygen-containing functional groups in RGQDs (Figure 5.6b). Due to these changes in absorbance spectra, it is expected that the fluorescence properties of RGQDs materials will also be different from both the parent RGO and even GO. Although RGO did not exhibit any sign of fluorescence emission (Figure 5.6c), RGQDs show

excitation-independent fluorescence peaking at ~532 nm with an excitation range of 300 to 475 nm and excitation-dependent emission behavior at larger wavelengths (Figure 5.6d). This visible emission is most likely to be originated from quantum dot size-dependent strong quantum confinement effects,whereas its excitation dependence above 475 nm suggests the presence of different types/sizes of RGQDs emissive species. Most interestingly, these RGQDs exhibit excitation-independent emission in the near infrared-I region peaking at ~950 nm and showing maximum emission at 475 nm excitation with further emission intensity decrease as the excitation is shifted up to 800 nm (Figure 5.6e). However, even with 808 nm laser excitation, RGQDs still exhibit bright fluorescence in the near-IR region (Figure 5.6f) indicating their potential as near-IR excited and NIR-emitting fluorophore desirable for biological in-vitro/in-vivo/ex-vivo imaging applications. Considering the regions of NIR emission from GQDs discussed in previous chapters this observed NIR feature can be potentially attributed to the localized defect states created by the hypochlorite reaction.

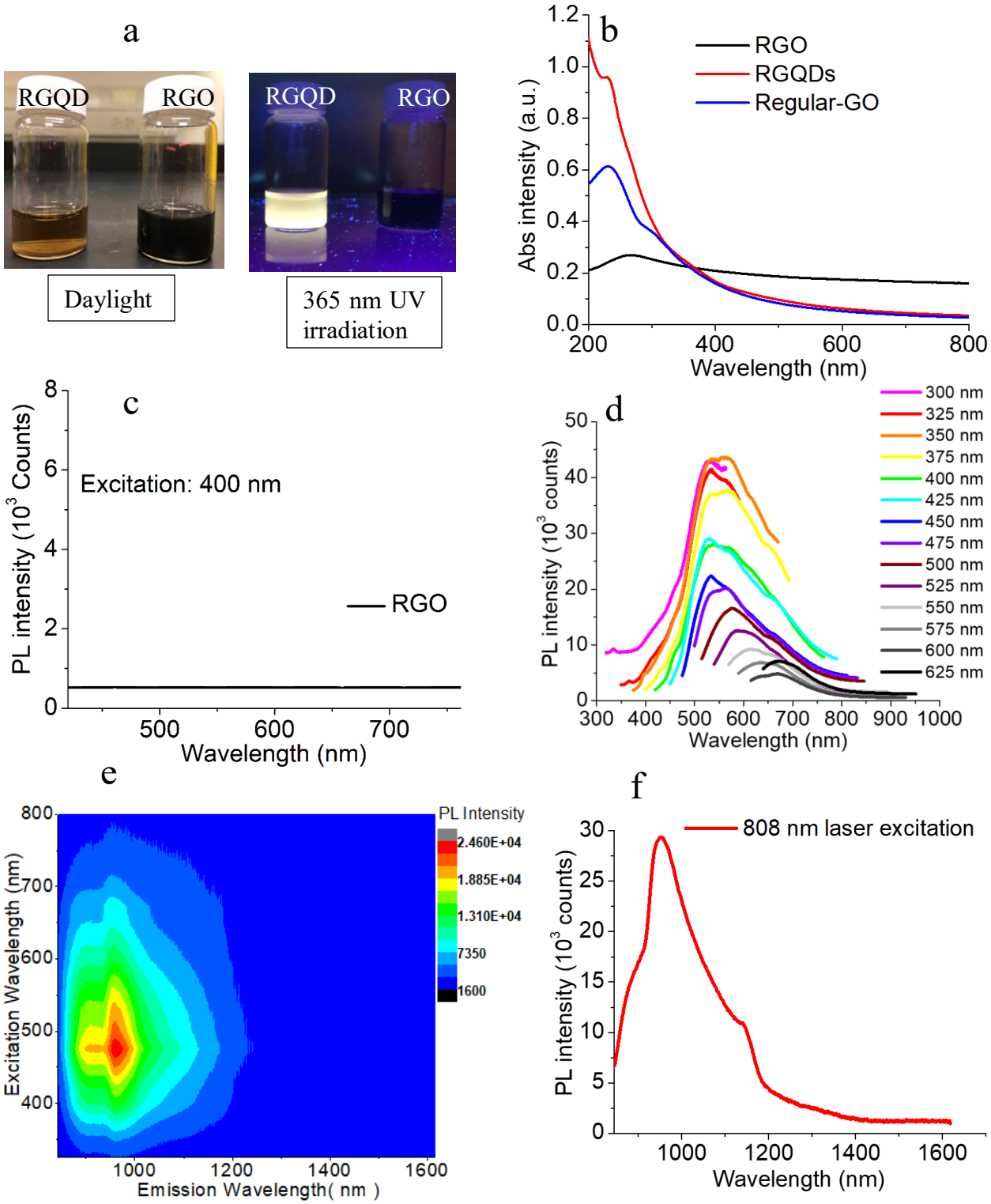

Figure 5.6: (a) Physical color of aqueous RGO/RGQDs under daylight and 365 nm UV excitation; (b) Absorbance spectra of RGO, GO, RGQDs; Fluorescence spectra of (c) RGO, (d) RGQDs in visible; (e) Photoluminescence excitation-emission map of RGQDs; (f) Near-IR emission from RGQDs at 808 nm laser excitation.

The absolute visible and NIR quantum yield (QY) of RGQDs was measured using an integrating sphere with Spectralon coating. Here, an example is provided to assess the QY of RGQDs in green with blue (405 nm) laser excitation providing a quantum yield of 7.13±0.85% (Figure 5.7).

$$Quantum\ Yield = \frac{Area\ of\ Peak\ C}{Area\ of\ Peak\ A - Area\ of\ Peak\ B} \times 100\%$$

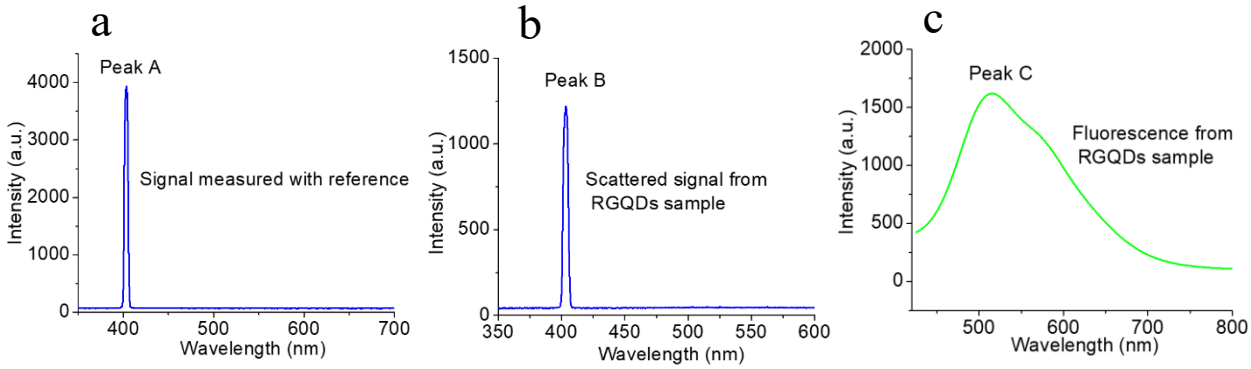

Figure 5.7: (a) Signal measured with reference (water only); (b) Scattered signal from aqueous RGQDs sample; (c) Enhanced fluorescence emission with RGQDs at 405 nm laser excitation.

By using this method, QY of RGQDs in NIR-I is also measured as 6.29±0.50% and 1.34±0.15% with 637 and 808 nm excitation, respectively. Additionally, QYs of some standard dyes are also measured to verify the measurement using this method providing good agreement with the values reported in the literature (Table 5.1).

Table – 5.1: Measurement of absolute QY of RGQDs/Rh-700/IR-140

Sample Name	Solvent	Excitation wavelength (nm)	Emitted wavelength range (nm)	QY reported in the literature (%)	Measured QY in this work (%)
RGQDs	Water	405	425-800	-	7.13±0.85
RGQDs	Water	637	800-1100	-	6.29±0.50
RGQDs	Water	808	900-1100	-	1.34±0.15
Rh-700	Ethanol	637	675-850	34.00±2.00[185]	32.70±2.50
IR-140	Ethanol	808	840-1100	16.70±1.00[186]	18.35±1.75

The aqueous RGQDs were further imaged using a NIR wavelength-resolved hyperspectral fluorescence microscopy allowing to collect wavelength-resolved images within 900-1600 nm spectral range. Under a microscope RGQDs and their clusters that are easy to trace showed bright emission at 950 nm with 808 nm laser excitation similar to the spectroscopic fluorescence measurements of RGQDs (Figure 5.8a,b) suggesting RGQDs as a potential nanomaterial for nanoscale imaging applications.

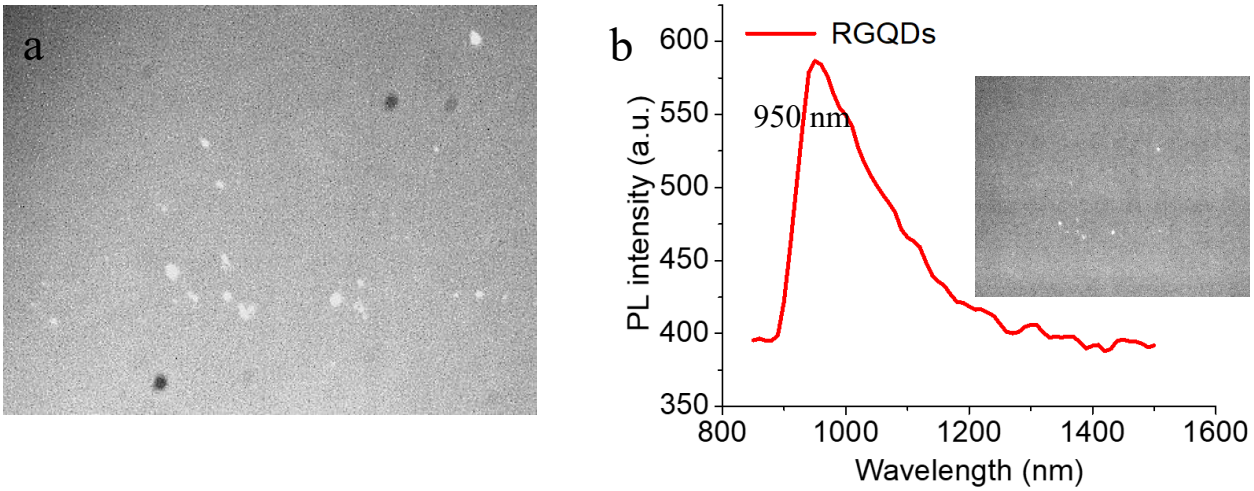

Figure 5.8: NIR hyperspectral fluorescence images of RGQDs utilizing the (a) broadband mode, (b) inset: bandpass mode at 950 nm. Recovery of the spectra from the fluorescence images showing NIR emission peaking at 950 nm.

Although RGQDs so far have exhibited high potential for bioimaging considering microscopically observable NIR emission with NIR excitation, further biological applications of RGQDs substantially depend on their biocompatibility. As that has been a common downfall of the majority of nanomaterials, we assess the biocompatibility of the RGQDs via two cytotoxicity assays: MTT and Luminescence-based assay. MTT cytotoxicity assay performed in HeLa cells shows significant cell viability (over 80%) at a maximum concentration of 68 µg/ml (Figure 5.9a) which could be sufficient for in-vitro imaging. As nanomaterials are known to interfere with the absorption-based MTT method[187, 188] the RGQDs are first only tested at low concentrations. To assess the maximum RGQD concentration that can be used for bioimaging we further perform Luminescence cytotoxicity assay (Figure 5.9b) that indicates high (with ~80% cell viability) biocompatibility for RGQDs at concentrations up to 1mg/mL. These concentrations were further used for *in vitro* and *in vivo* imaging experiments.

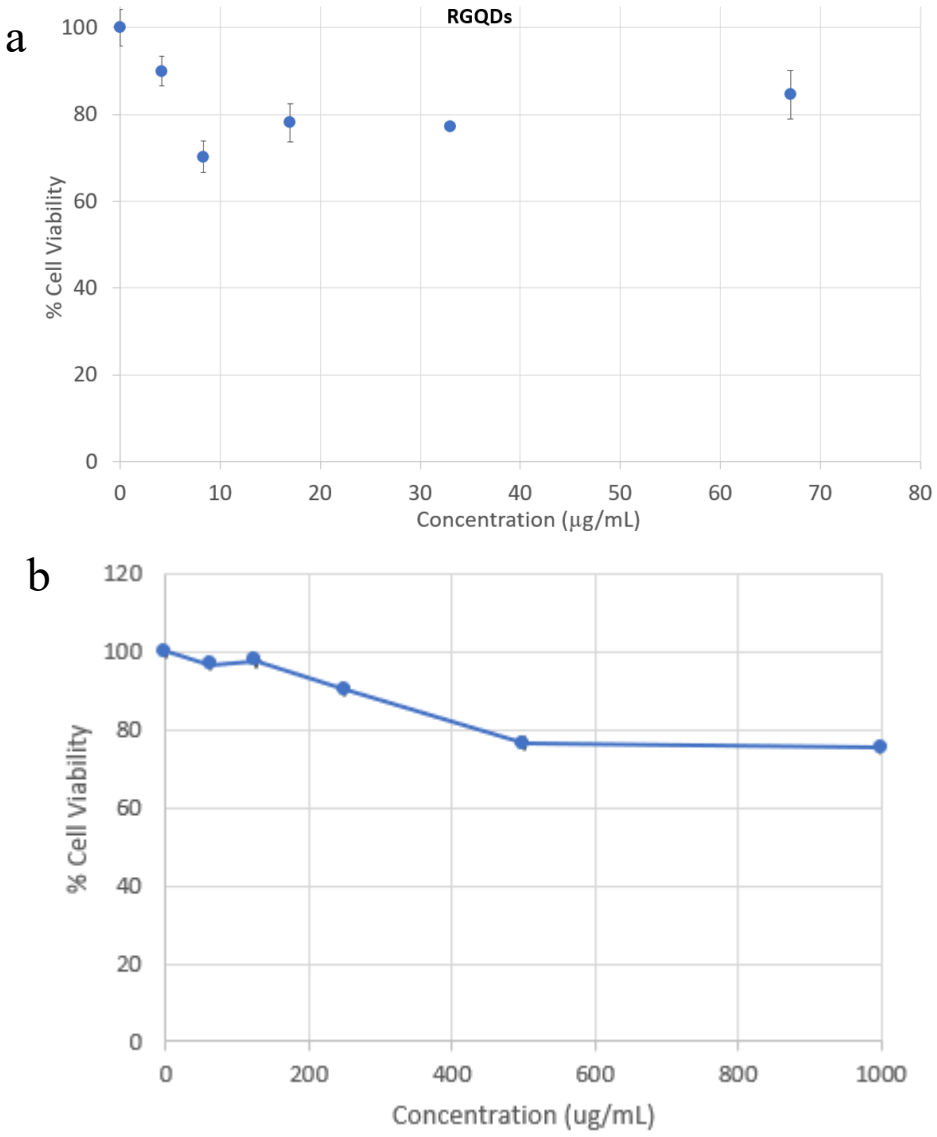

Figure 5.9: Cytotoxicity of RGQDs in HeLa cells showing percent cell viability at different RGQDs concentration assessed via (a) MTT assay (b) Luminescence-based assay (error bars are within the data points).

As visible and NIR emission of RGQDs has a high potential for biomedical imaging applications, it was fully characterized and tested with confocal fluorescence microscopy imaging in vitro showing a bright intracellular fluorescence emission in green (550±20 nm) with 460±20 nm excitation (Figure 5.10) and NIR-I (950 nm) with 808 nm laser excitation (Figure 5.11) indicating substantial cellular internalization of RGQDs at 3 and 12h time points.

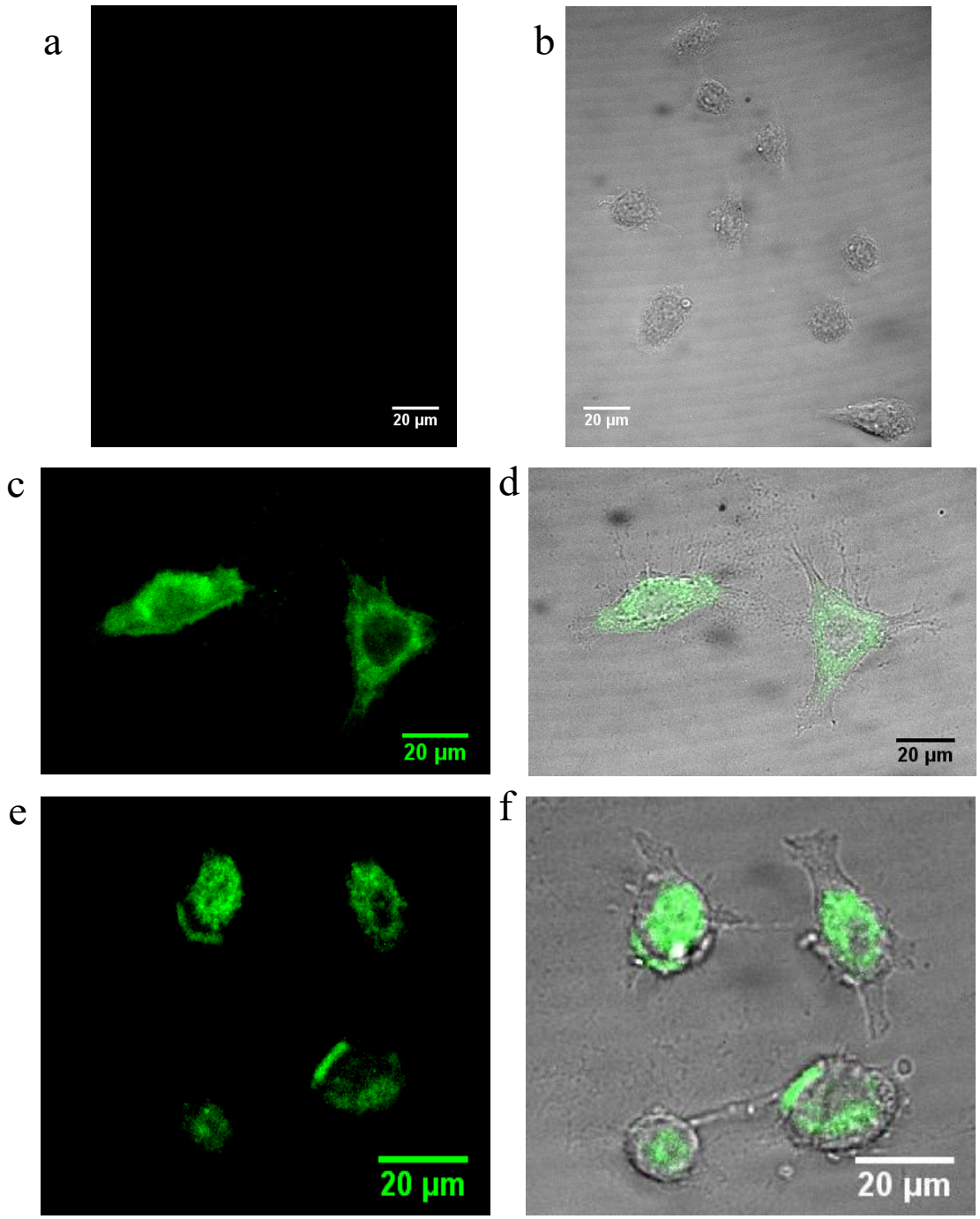

Figure 5.10: (a) No fluorescence from untreated control HeLa Cells. Brightfield/fluorescence (confocal) overlay images of (b) untreated control HeLa cells, and cellular uptake of RGQDs imaged with 460 nm excitation at (b,c) 3h, (d,e) 12h transfection points.

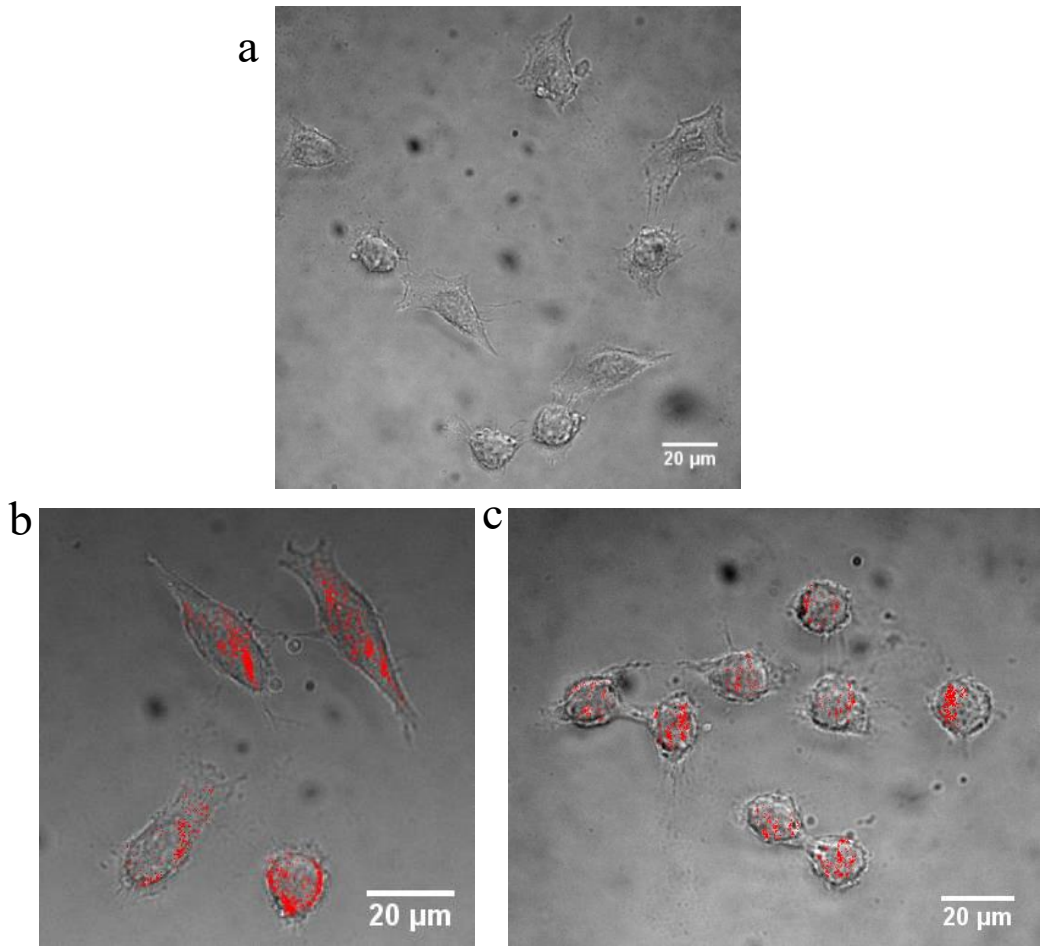

Figure 5.11: Brightfield/ NIR fluorescence overlay images of (a) untreated control HeLa cells and cellular uptake of RGQDs imaged with 808 nm laser excitation at (b) 3h, (c) 12h transfection points.

Additionally, the in-vivo/ex-vivo mouse imaging of RGQDs is done by collaboration with Professor Belcher's Lab at MIT (Massachusetts Institute of Technology) performed by Dr. Ching Wei Lin. The RGQDs were injected intravenously in mice through a tail vein and hours after injection imaged in live sedated animals with 808 nm laser excitation and 900 nm long-pass emission filter. Live animal NIR images exhibit little to no NIR fluorescence until six hours post-injection when they start showing substantial GQD emission mainly from the spleen with some less intense signal originating from the liver which is confirmed as the animal is sacrificed and

dissected (Figure 5.12a,b,c). However, the excised organs collected after sacrificing the animals show the distribution/accumulation of RGQDs mainly in spleen, kidney, liver, and intestine (Figure 5.12c,d) at 6h post-injection.

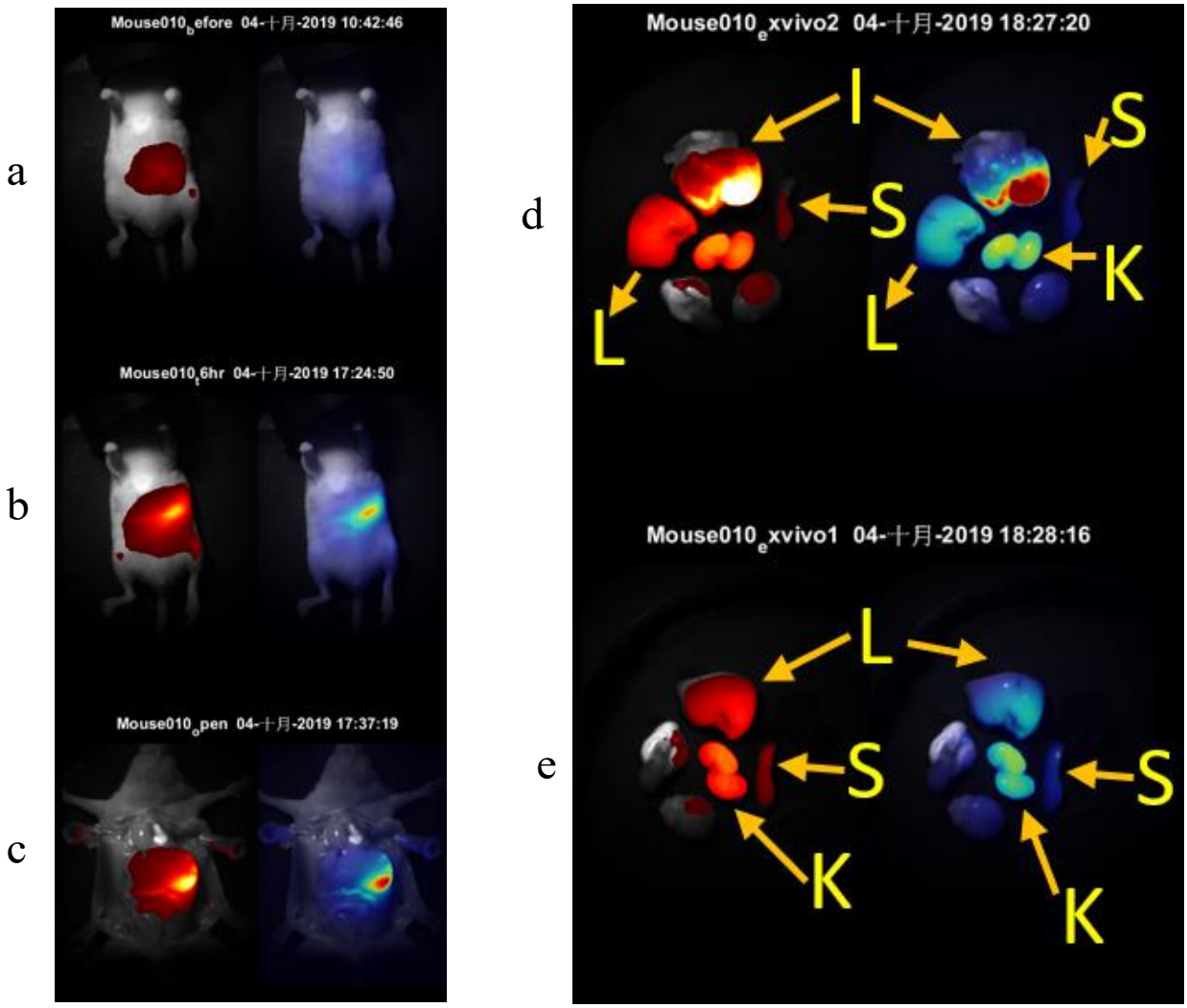

Figure 5.12: Brightfield/NIR fluorescence overlay images (left image) and color-coded (right image) images of a live sedated mouse in ventral position performed with 808 nm laser excitation and 900 nm long-pass filter (a) before the intravenous injection in mouse, (b) whole body distribution of RGQDs in mouse after 6h of injection (c) image of a treated and dissected sacrificed mouse (d,e) ex-vivo images showing the fluorescence of RGQDs in kidney (K), liver (L), intestine (I) and spleen (S) performed with 808 nm laser excitation and 900 nm long-pass filter.

5.4 Summary of chapter-5:

RGQDs were synthesized in this work with high production yield by using a simple, scalable, cost-effective, eco-friendly process show emission in visible and NIR-I with NIR quantum yields up to 8% indicating substantial potential for in-vitro/in-vivo/ex-vivo bioimaging. RGQDs are biocompatible with ~80% cell viability up to a maximum concentration of 1 mg/mL as determined by the MTT and Luminescence cytotoxicity assays. These RGQD concentrations were used for intracellular imaging in green and NIR showing bright intracellular emission from RGQDs at 3 and 12 h time points suggesting successful cellular uptake. Additionally, *in-vivo/ex-vivo* mouse imaging reveals the distribution of RGQDs in the spleen, kidney, liver, and intestine suggesting that RGQDs can be successfully utilized as NIR imaging agents in live animals. Finally, given a variety of functional addends for covalent and a graphitic platform for non-covalent functionalization, these materials have the potential to be used as a delivery vehicle for molecular and gene therapeutics.

CHAPTER 6

6.1 Summary:

In this work, we have developed two different synthetic routes (bottom-up/top-down) to synthesize novel graphene quantum dots. The bottom-up microwave-assisted hydrothermal approach allows us to synthesize nitrogen-doped and nitrogen/sulfur co-doped graphene quantum dots utilizing a method exhibiting excitation-dependent fluorescence emission with high quantum yield in the visible and near-infrared. These quantum dots are utilized further to fabricate electroluminescence LED, solar cells and UV photodetector devices. Additionally, in a separate work[189], these quantum dots have been utilized for multi-color intracellular bioimaging and pH-dependent fluorescence-based ratiometric *in-vitro* cancer sensing applications. The EL devices prepared with pristine NGQDs described in Chapter 2 show bright electroluminescence peaking at ~525 nm with moderate turn-on voltage (~7V) suggesting a high potential for low cost environmentally-friendly organic LEDs. The photovoltaic performances recorded from the solar cells fabricated with as-prepared NGQDs (Chapter 2) were comparable to the existing reports however turned out to be insufficient for practical applications. Therefore, to boost the photovoltaic performance of the solar cells, we tuned the optical/structural properties of as-prepared NGQDs via controlled ozone treatment (Chapter 3). Devices fabricated with OzNGQDs yielded excellent fill factor (28 to 86.40%) along with significant enhancement of power conversion efficiency (from 0.41 to 2.64%), short circuit current density (from 1.13 to 4.8mAcm^{-2}), and open-circuit voltage (from 0.57 to 0.83V). Further applications of NGQDs were enabled by the UV processing. Short (254 nm)/mid (302 nm)/long-wave (365 nm) UV treatment induced

significant variations in the optical response of NGQDs along with a considerable change in chemical composition, size, and shape. Such strong optical response with UV treatment leads us to the idea of fabricating UV photodetectors with untreated and UV-treated NGQDs as sensitizer (Chapter 3). These devices tested under 254/302/365 nm UV illumination yielded highly reproducible and fast photo-switching characteristics with high photosensitivity up to 0.59 A/W and excellent photodetectivity up to $1.03X10^{11}$ Jones. On par with previously reported graphene quantum dot-based devices (Table-4.1), NGQD-based UV photodetectors developed in this work due to the eco-friendly/simple/scalable NGQD fabrication process present a promising optoelectronic solution.

On the other hand, a separate UV-facilitated aqueous top-down approach was developed to synthesize novel GQDs (RGQDs) from optically inert reduced graphene oxide exhibiting partially excitation-independent emission in visible and NIR-I (~950 nm) region with quantum yields ranging from 1.4 to 8%. These well-distributed/dispersed RGQDs possess a smaller average size of 3.54±0.05 nm along with a highly crystalline lattice structure detected *via* high-resolution transmission electron microscopy. High biocompatibility of RGQDs with ~80% cell viability for up to a high 1mg/mL concentration is verified via both MTT and Luminescence cytotoxicity assays. Their 950 nm NIR emission was microscopically imaged using a wavelength-resolved hyperspectral NIR fluorescence microscopy setup with 808 nm laser excitation suggesting high potential for NIR-only biological imaging. Their small size, high water solubility, bright NIR emission, and high biocompatibility make these RGQDs a better candidate for biological applications than the majority of complex and costly nanomaterials. In the *in vitro* study, RGQDs exhibit effective cellular internalization with substantial intracellular NIR fluorescence compared

to the control at 3 and 12 h time points indicating successful internalization. Furthermore, *in-vivo/ex-vivo* mouse imaging of RGQDs was performed showing the accumulation of RGQDs mainly in spleen, kidney, liver, and intestine indicating the potential of RGQDs as NIR imaging agent in live mice and a potential vehicle for drug delivery.

6.2 Questions answered by this study:

i. Can we synthesize graphene quantum dots (GQDs) with superior optical properties using a simple/scalable/eco-friendly bottom-up approach?

   We utilize a simple, scalable, environmental-friendly hydrothermal approach to synthesize NGQDs/NS-GQDs from a widely available/inexpensive glucosamine/thiourea precursor. The hydrothermal reaction takes place inside a commercially available microwave oven suggesting no complex set-up is necessary for the successful synthesis process. This method yields well-distributed 3-5 nm mean diameter spherical GQDs showing fluorescence emission with high quantum yield in visible (up to 60%) and NIR region. This indicates the successful venture of producing GQDs with superior to current counterparts (complex in synthesis and exhibiting lower yield visible emission only) optical/structural properties.

ii. Can we utilize these solution-processable GQDs for optoelectronic device applications?

We have fabricated several prototypes of light-emitting devices with bright electroluminescence/moderate turn-on voltage, solar cells with excellent fill factor, considerable power conversion efficiency/open-circuit voltage/short circuit current density and UV photodetectors with high photosensitivity/excellent photodetectivity suggesting GQDs as a promising material for optoelectronic device applications.

iii. Can we utilize these GQDs for biological imaging applications?

In a separate work[189], it has also been shown that these GQDs can be utilized for multi-color *in-vitro* imaging and pH-dependent fluorescence-based ratiometric cancer sensing applications.

iv. Can we modify the optical properties of these GQDs for specific applications?

The optical/structural properties of these NGQDs are optimized further using a controlled ozone treatment leading to the enhancement of solar cell performances. Also, three different UV wavelengths (254/302/365) are utilized to controllably treat the as-prepared NGQDs showing a significant change in structural/optical properties which appeared to be optimal for the fabrication of UV photodetectors with high reproducibility and rapid photo-switching behavior.

v. Can we produce graphene quantum dots (GQDs) exhibiting visible/near-IR fluorescence using a simple/cost-effective top-down approach?

A top-down approach involving oxidative scission of micron-sized non-fluorescent RGO into nanometer-sized brightly fluorescent RGQDs was developed with the presence of UV/NaOCl. This method requires a simple instrumental setup which with very high production yield produces unique RGQDs exhibiting partially excitation-independent emission in visible and NIR-I region.

vi. Can these GQDs (prepared from a top-down approach) be used for biological imaging applications?

We exploit these RGQDs for in-vitro/in-vivo/ex-vivo biological imaging applications based on their minimal cytotoxicity and NIR imaging capability with both excitation and emission in the biologically-desired NIR I region.

6.3 Future work direction

Although extensive studies have been performed to characterize the GQDs and exploring their optoelectronic device/biological applications prepared from a bottom-up approach, more investigations are yet to be done. The unique properties of these N-GQDs and NS-GQDs offer substantial promising further research potential. We can propose using different device geometry along with varying the thickness of the GQDs or changing the types of electrodes for better band alignment, which may lead us to achieve much higher device performances. Also, separate *in-*

vivo biodistribution and bio-imaging studies exploring the potential of NGQDs as drug/gene-delivery carriers are expected and are highly anticipated.

Optoelectronic device applications of newly produced RGQDs synthesized with the top-down method are also yet to be delved. Currently, we are working on the *in-vivo* biodistribution studies and bioimaging applications of RGQDs. These materials also have the potential to be used in drug delivery and biosensing applications. Furthermore, because of their excellent optical properties, these materials (N-GQDs/NS-GQDs/RGQDs) can be used for metal (heavy/toxic or bio-friendly metals) ion sensing and fingerprinting applications.

REFERENCES:

(1) Castro Neto, A. H.; Guinea, F.; Peres, N. M. R.; Novoselov, K. S. and Geim, A. K., *The Electronic Properties of Graphene.* Reviews of Modern Physics, **2009**. *81*(1): p. 109-162.

(2) Boukhvalov, D. W.; Katsnelson, M. I. and Lichtenstein, A. I., *Hydrogen on Graphene: Electronic Structure, Total Energy, Structural Distortions and Magnetism from First-Principles Calculations.* Physical Review B, **2008**. *77*(3): p. 035427.

(3) Slonczewski, J. C. and Weiss, P. R., *Band Structure of Graphite.* Physical Review, **1958**. *109*(2): p. 272-279.

(4) Geim, A. K., *Graphene: Status and Prospects.* Science, **2009**. *324*(5934): p. 1530.

(5) Okigawa, Y.; Tsugawa, K.; Yamada, T.; Ishihara, M. and Hasegawa, M., *Electrical Characterization of Graphene Films Synthesized by Low-Temperature Microwave Plasma Chemical Vapor Deposition.* Applied Physics Letters, **2013**. *103*(15): p. 153106.

(6) Ma, X. and Zhang, H., *Fabrication of Graphene Films with High Transparent Conducting Characteristics.* Nanoscale Research Letters, **2013**. *8*(1): p. 440.

(7) Geim, A. K. and Novoselov, K. S., *The Rise of Graphene.* Nature Materials, **2007**. *6*: p. 183.

(8) Wassei, J. K. and Kaner, R. B., *Graphene, a Promising Transparent Conductor.* Materials Today, **2010**. *13*(3): p. 52-59.

(9) Schedin, F.; Geim, A. K.; Morozov, S. V.; Hill, E. W.; Blake, P.; Katsnelson, M. I. and Novoselov, K. S., *Detection of Individual Gas Molecules Adsorbed on Graphene.* Nature Materials, **2007**. *6*(9): p. 652-655.

(10) Eda, G.; Emrah Unalan, H.; Rupesinghe, N.; Amaratunga, G. A. J. and Chhowalla, M., *Field Emission from Graphene Based Composite Thin Films.* Applied Physics Letters, **2008**. *93*(23): p. 233502.

(11) Kim, K. S.; Zhao, Y.; Jang, H.; Lee, S. Y.; Kim, J. M.; Kim, K. S.; Ahn, J.-H.; Kim, P.; Choi, J.-Y. and Hong, B. H., *Large-Scale Pattern Growth of Graphene Films for Stretchable Transparent Electrodes.* Nature, **2009**. *457*(7230): p. 706-710.

(12) Wang, X.; Zhi, L. and Müllen, K., *Transparent, Conductive Graphene Electrodes for Dye-Sensitized Solar Cells.* Nano Letters, **2008**. *8*(1): p. 323-327.

(13) Novoselov, K.; Geim, A.; Morozov, S.; Jiang, D.; Zhang, Y. and Dubonos, S., *Electric Field Effect in Atomically Thin Carbon Films.* Science, **2004**. *306*.

(14) Paek, S.-M.; Yoo, E. and Honma, I., *Enhanced Cyclic Performance and Lithium Storage Capacity of Sno2/Graphene Nanoporous Electrodes with Three-Dimensionally Delaminated Flexible Structure.* Nano Letters, **2009**. *9*(1): p. 72-75.

(15) Somani, P. R.; Somani, S. P. and Umeno, M., *Planer Nano-Graphenes from Camphor by Cvd.* Chemical Physics Letters, **2006**. *430*(1): p. 56-59.

(16) Wang, J.; Zhu, M.; Outlaw, R. A.; Zhao, X.; Manos, D. M. and Holloway, B. C., *Synthesis of Carbon Nanosheets by Inductively Coupled Radio-Frequency Plasma Enhanced Chemical Vapor Deposition.* Carbon, **2004**. *42*(14): p. 2867-2872.

(17) Hass, J.; Heer, W. A. d. and Conrad, E. H., *The Growth and Morphology of Epitaxial Multilayer Graphene.* Journal of Physics: Condensed Matter, **2008**. *20*(32): p. 323202.

(18) Subrahmanyam, K. S.; Panchakarla, L. S.; Govindaraj, A. and Rao, C. N. R., *Simple Method of Preparing Graphene Flakes by an Arc-Discharge Method.* The Journal of Physical Chemistry C, **2009**. *113*(11): p. 4257-4259.

(19) Li, X.; Zhang, G.; Bai, X.; Sun, X.; Wang, X.; Wang, E. and Dai, H., *Highly Conducting Graphene Sheets and Langmuir–Blodgett Films.* Nature Nanotechnology, **2008**. *3*: p. 538.

(20) Paton, K. R.; Varrla, E.; Backes, C.; Smith, R. J.; Khan, U.; O'Neill, A.; Boland, C.; Lotya, M.; Istrate, O. M.; King, P.; Higgins, T.; Barwich, S.; May, P.; Puczkarski, P.; Ahmed, I.; Moebius, M.; Pettersson, H.; Long, E.; Coelho, J.; O'Brien, S. E.; McGuire, E. K.; Sanchez, B. M.; Duesberg, G. S.; McEvoy, N.; Pennycook, T. J.; Downing, C.; Crossley, A.; Nicolosi, V. and Coleman, J. N., *Scalable Production of Large Quantities of Defect-Free Few-Layer Graphene by Shear Exfoliation in Liquids.* Nature Materials, **2014**. *13*: p. 624.

(21) McAllister, M. J.; Li, J.-L.; Adamson, D. H.; Schniepp, H. C.; Abdala, A. A.; Liu, J.; Herrera-Alonso, M.; Milius, D. L.; Car, R.; Prud'homme, R. K. and Aksay, I. A., *Single Sheet Functionalized Graphene by Oxidation and Thermal Expansion of Graphite.* Chemistry of Materials, **2007**. *19*(18): p. 4396-4404.

(22) Eda, G.; Fanchini, G. and Chhowalla, M., *Large-Area Ultrathin Films of Reduced Graphene Oxide as a Transparent and Flexible Electronic Material.* Nature Nanotechnology, **2008**. *3*: p. 270.

(23) Gómez-Navarro, C.; Weitz, R. T.; Bittner, A. M.; Scolari, M.; Mews, A.; Burghard, M. and Kern, K., *Electronic Transport Properties of Individual Chemically Reduced Graphene Oxide Sheets.* Nano Letters, **2007**. *7*(11): p. 3499-3503.

(24) Bourlinos, A. B.; Gournis, D.; Petridis, D.; Szabó, T.; Szeri, A. and Dékány, I., *Graphite Oxide: Chemical Reduction to Graphite and Surface Modification with Primary Aliphatic Amines and Amino Acids.* Langmuir, **2003**. *19*(15): p. 6050-6055.

(25) Shin, H. J.; Kim Ki, K.; Benayad, A.; Yoon, S. M.; Park Hyeon, K.; Jung, I. S.; Jin Mei, H.; Jeong, H. K.; Kim Jong, M.; Choi, J. Y. and Lee Young, H., *Efficient Reduction of Graphite Oxide by Sodium Borohydride and Its Effect on Electrical Conductance.* Advanced Functional Materials, **2009**. *19*(12): p. 1987-1992.

(26) Li, D.; Müller, M. B.; Gilje, S.; Kaner, R. B. and Wallace, G. G., *Processable Aqueous Dispersions of Graphene Nanosheets.* Nature Nanotechnology, **2008**. *3*: p. 101.

(27) Wang, Y.; Chen, Y.; Lacey, S. D.; Xu, L.; Xie, H.; Li, T.; Danner, V. A. and Hu, L., *Reduced Graphene Oxide Film with Record-High Conductivity and Mobility.* Materials Today, **2018**. *21*(2): p. 186-192.

(28) El-Sayed, M. A., *Small Is Different: Shape-, Size-, and Composition-Dependent Properties of Some Colloidal Semiconductor Nanocrystals.* Accounts of Chemical Research, **2004**. *37*(5): p. 326-333.

(29) Li, L.-s. and Yan, X., *Colloidal Graphene Quantum Dots.* The Journal of Physical Chemistry Letters, **2010**. *1*(17): p. 2572-2576.

(30) Bacon, M.; Bradley, S. J. and Nann, T., *Graphene Quantum Dots.* Particle & Particle Systems Characterization, **2014**. *31*(4): p. 415-428.

(31) Loh, K. P.; Bao, Q.; Eda, G. and Chhowalla, M., *Graphene Oxide as a Chemically Tunable Platform for Optical Applications.* Nat Chem, **2010**. *2*(12): p. 1015-1024.

(32) Md Tanvir, H.; Brian, J. S.; Price, M.; Conor, R.; Hung, D.; Zygmunt, G. and Anton, V. N., *Modifying Optical Properties of Reduced/Graphene Oxide with Controlled Ozone and Thermal Treatment in Aqueous Suspensions.* Nanotechnology, **2017**. *28*(6): p. 065705.

(33) Tang, L.; Ji, R.; Cao, X.; Lin, J.; Jiang, H.; Li, X.; Teng, K. S.; Luk, C. M.; Zeng, S.; Hao, J. and Lau, S. P., *Deep Ultraviolet Photoluminescence of Water-Soluble Self-Passivated Graphene Quantum Dots.* ACS Nano, **2012**. *6*(6): p. 5102-5110.

(34) Peng, J.; Gao, W.; Gupta, B.; Liu, Z.; Romero-Aburto, R. and Ge, L., *Graphene Quantum Dots Derived from Carbon Fibers.* Nano Lett, **2012**. *12*.

(35) Lu, J.; Yang, J.-x.; Wang, J.; Lim, A.; Wang, S. and Loh, K. P., *One-Pot Synthesis of Fluorescent Carbon Nanoribbons, Nanoparticles, and Graphene by the Exfoliation of Graphite in Ionic Liquids.* ACS Nano, **2009**. *3*(8): p. 2367-2375.

(36) Senkovskiy, B. V.; Pfeiffer, M.; Alavi, S. K.; Bliesener, A.; Zhu, J.; Michel, S.; Fedorov, A. V.; German, R.; Hertel, D.; Haberer, D.; Petaccia, L.; Fischer, F. R.; Meerholz, K.; van Loosdrecht, P. H. M.; Lindfors, K. and Grüneis, A., *Making Graphene Nanoribbons Photoluminescent.* Nano Letters, **2017**. *17*(7): p. 4029-4037.

(37) Chen, J.-L.; Yan, X.-P.; Meng, K. and Wang, S.-F., *Graphene Oxide Based Photoinduced Charge Transfer Label-Free near-Infrared Fluorescent Biosensor for Dopamine.* Analytical Chemistry, **2011**. *83*(22): p. 8787-8793.

(38) Naumov, A.; Grote, F.; Overgaard, M.; Roth, A.; Halbig, C. E.; Nørgaard, K.; Guldi, D. M. and Eigler, S., *Graphene Oxide: A One- Versus Two-Component Material.* Journal of the American Chemical Society, **2016**. *138*(36): p. 11445-11448.

(39) Ye, R.; Peng, Z.; Metzger, A.; Lin, J.; Mann, J. A.; Huang, K.; Xiang, C.; Fan, X.; Samuel, E. L. G.; Alemany, L. B.; Martí, A. A. and Tour, J. M., *Bandgap Engineering of Coal-Derived Graphene Quantum Dots.* ACS Applied Materials & Interfaces, **2015**. *7*(12): p. 7041-7048.

(40) Wang, L.; Wang, Y.; Xu, T.; Liao, H.; Yao, C.; Liu, Y.; Li, Z.; Chen, Z.; Pan, D.; Sun, L. and Wu, M., *Gram-Scale Synthesis of Single-Crystalline Graphene Quantum Dots with Superior Optical Properties.* Nature Communications, **2014**. *5*: p. 5357.

(41) Ye, R.; Xiang, C.; Lin, J.; Peng, Z.; Huang, K.; Yan, Z.; Cook, N. P.; Samuel, E. L. G.; Hwang, C.-C.; Ruan, G.; Ceriotti, G.; Raji, A.-R. O.; Martí, A. A. and Tour, J. M., *Coal as an Abundant Source of Graphene Quantum Dots.* Nature Communications, **2013**. *4*: p. 2943.

(42) Zhu, S.; Song, Y.; Wang, J.; Wan, H.; Zhang, Y.; Ning, Y. and Yang, B., *Photoluminescence Mechanism in Graphene Quantum Dots: Quantum Confinement Effect and Surface/Edge State.* Nano Today, **2017**. *13*: p. 10-14.

(43) Sun, J.; Yang, S.; Wang, Z.; Shen, H.; Xu, T.; Sun, L.; Li, H.; Chen, W.; Jiang, X.; Ding, G.; Kang, Z.; Xie, X. and Jiang, M., *Ultra-High Quantum Yield of Graphene Quantum Dots: Aromatic-Nitrogen Doping and Photoluminescence Mechanism.* Particle & Particle Systems Characterization, **2015**. *32*(4): p. 434-440.

(44) Niu, F.; Xu, Y.; Liu, J.; Song, Z.; Liu, M. and Liu, J., *Controllable Electrochemical/Electroanalytical Approach to Generate Nitrogen-Doped Carbon Quantum Dots from Varied Amino Acids: Pinpointing the Utmost Quantum Yield and the Versatile Photoluminescent and Electrochemiluminescent Applications.* Electrochimica Acta, **2017**. *236*: p. 239-251.

(45) Liu, Q.; Guo, B.; Rao, Z.; Zhang, B. and Gong, J. R., *Strong Two-Photon-Induced Fluorescence from Photostable, Biocompatible Nitrogen-Doped Graphene Quantum Dots for Cellular and Deep-Tissue Imaging.* Nano Letters, **2013**. *13*(6): p. 2436-2441.

(46) Hasan, M. T.; Gonzalez-Rodriguez, R.; Ryan, C.; Faerber, N.; Coffer, J. L. and Naumov, A. V., *Photo-and Electroluminescence from Nitrogen-Doped and Nitrogen–Sulfur Codoped Graphene Quantum Dots.* Advanced Functional Materials, **2018**. *28*(42): p. 1804337.

(47) Nurunnabi, M.; Khatun, Z.; Huh, K. M.; Park, S. Y.; Lee, D. Y.; Cho, K. J. and Lee, Y.-k., *In Vivo Biodistribution and Toxicology of Carboxylated Graphene Quantum Dots.* ACS Nano, **2013**. *7*(8): p. 6858-6867.

(48) Zhou, L.; Geng, J. and Liu, B., *Graphene Quantum Dots from Polycyclic Aromatic Hydrocarbon for Bioimaging and Sensing of Fe3+ and Hydrogen Peroxide.* Particle & Particle Systems Characterization, **2013**. *30*(12): p. 1086-1092.

(49) Zhu, X.; Zhao, T.; Nie, Z.; Miao, Z.; Liu, Y. and Yao, S., *Nitrogen-Doped Carbon Nanoparticle Modulated Turn-on Fluorescent Probes for Histidine Detection and Its Imaging in Living Cells.* Nanoscale, **2016**. *8*(4): p. 2205-2211.

(50) Qiu, J.; Zhang, R.; Li, J.; Sang, Y.; Tang, W.; Rivera Gil, P. and Liu, H., *Fluorescent Graphene Quantum Dots as Traceable, Ph-Sensitive Drug Delivery Systems.* International Journal of Nanomedicine, **2015**. *10*: p. 6709-6724.

(51) Campbell, E.; Hasan, M. T.; Gonzalez Rodriguez, R.; Akkaraju, G. R. and Naumov, A. V., *Doped Graphene Quantum Dots for Intracellular Multicolor Imaging and Cancer Detection.* ACS Biomaterials Science & Engineering, **2019**.

(52) Coe, S.; Woo, W.-K.; Bawendi, M. and Bulović, V., *Electroluminescence from Single Monolayers of Nanocrystals in Molecular Organic Devices.* Nature, **2002**. *420*: p. 800.

(53) Tessler, N.; Medvedev, V.; Kazes, M.; Kan, S. and Banin, U., *Efficient near-Infrared Polymer Nanocrystal Light-Emitting Diodes.* Science, **2002**. *295*(5559): p. 1506.

(54) Son, D. I.; Kwon, B. W.; Park, D. H.; Seo, W.-S.; Yi, Y.; Angadi, B.; Lee, C.-L. and Choi, W. K., *Emissive Zno–Graphene Quantum Dots for White-Light-Emitting Diodes.* Nature Nanotechnology, **2012**. *7*: p. 465.

(55) Nozik, A. J., *Quantum Dot Solar Cells.* Physica E: Low-dimensional Systems and Nanostructures, **2002**. *14*(1): p. 115-120.

(56) Gur, I.; Fromer, N. A.; Geier, M. L. and Alivisatos, A. P., *Air-Stable All-Inorganic Nanocrystal Solar Cells Processed from Solution.* Science, **2005**. *310*(5747): p. 462.

(57) Li, Y.; Hu, Y.; Zhao, Y.; Shi, G.; Deng, L. and Hou, Y., *An Electrochemical Avenue to Green-Luminescent Graphene Quantum Dots as Potential Electron-Acceptors for Photovoltaics.* Adv Mater, **2011**. *23*.

(58) Alivisatos, A. P.; Gu, W. and Larabell, C., *Quantum Dots as Cellular Probes.* Annual Review of Biomedical Engineering, **2005**. *7*(1): p. 55-76.

(59) Zhu, S.; Zhang, J.; Qiao, C.; Tang, S.; Li, Y.; Yuan, W.; Li, B.; Tian, L.; Liu, F.; Hu, R.; Gao, H.; Wei, H.; Zhang, H.; Sun, H. and Yang, B., *Strongly Green-Photoluminescent Graphene Quantum Dots for Bioimaging Applications.* Chemical Communications, **2011**. *47*(24): p. 6858-6860.

(60) Fan, Z.; Li, S.; Yuan, F. and Fan, L., *Fluorescent Graphene Quantum Dots for Biosensing and Bioimaging.* RSC Advances, **2015**. *5*(25): p. 19773-19789.

(61) Xie, R.; Wang, Z.; Zhou, W.; Liu, Y.; Fan, L.; Li, Y. and Li, X., *Graphene Quantum Dots as Smart Probes for Biosensing.* Analytical Methods, **2016**. *8*(20): p. 4001-4016.

(62) Kumawat, M. K.; Thakur, M.; Gurung, R. B. and Srivastava, R., *Graphene Quantum Dots for Cell Proliferation, Nucleus Imaging, and Photoluminescent Sensing Applications.* Scientific Reports, **2017**. *7*(1): p. 15858.

(63) Wu, Z. L.; Gao, M. X.; Wang, T. T.; Wan, X. Y.; Zheng, L. L. and Huang, C. Z., *A General Quantitative Ph Sensor Developed with Dicyandiamide N-Doped High Quantum Yield Graphene Quantum Dots.* Nanoscale, **2014**. *6*(7): p. 3868-3874.

(64) Zeng, Z.; Chen, S.; Tan, T. T. Y. and Xiao, F.-X., *Graphene Quantum Dots (Gqds) and Its Derivatives for Multifarious Photocatalysis and Photoelectrocatalysis.* Catalysis Today, **2018**.

(65) Pan, D.; Xi, C.; Li, Z.; Wang, L.; Chen, Z.; Lu, B. and Wu, M., *Electrophoretic Fabrication of Highly Robust, Efficient, and Benign Heterojunction Photoelectrocatalysts Based on Graphene-Quantum-Dot Sensitized Tio2 Nanotube Arrays.* Journal of Materials Chemistry A, **2013**. *1*(11): p. 3551-3555.

(66) Ge, J.; Lan, M.; Zhou, B.; Liu, W.; Guo, L.; Wang, H.; Jia, Q.; Niu, G.; Huang, X.; Zhou, H.; Meng, X.; Wang, P.; Lee, C.-S.; Zhang, W. and Han, X., *A Graphene Quantum Dot Photodynamic Therapy Agent with High Singlet Oxygen Generation.* Nature Communications, **2014**. *5*: p. 4596.

(67) Tabish, T. A.; Scotton, C. J.; Ferguson, D. C. J.; Lin, L.; Veen, A. v. d.; Lowry, S.; Ali, M.; Jabeen, F.; Ali, M.; Winyard, P. G. and Zhang, S., *Biocompatibility and Toxicity of Graphene Quantum Dots for Potential Application in Photodynamic Therapy.* Nanomedicine, **2018**. *13*(15): p. 1923-1937.

(68) Wang, H.-J.; He, X.; Luo, T.-Y.; Zhang, J.; Liu, Y.-H. and Yu, X.-Q., *Amphiphilic Carbon Dots as Versatile Vectors for Nucleic Acid and Drug Delivery.* Nanoscale, **2017**. *9*(18): p. 5935-5947.

(69) Kim, S.; Choi, Y.; Park, G.; Won, C.; Park, Y.-J.; Lee, Y.; Kim, B.-S. and Min, D.-H., *Highly Efficient Gene Silencing and Bioimaging Based on Fluorescent Carbon Dots in Vitro and in Vivo.* Nano Research, **2017**. *10*(2): p. 503-519.

(70) Ding, H.; Du, F.; Liu, P.; Chen, Z. and Shen, J., *DNA–Carbon Dots Function as Fluorescent Vehicles for Drug Delivery.* ACS Applied Materials & Interfaces, **2015**. *7*(12): p. 6889-6897.

(71) Salinas-Castillo, A.; Ariza-Avidad, M.; Pritz, C.; Camprubí-Robles, M.; Fernández, B.; Ruedas-Rama, M. J.; Megia-Fernández, A.; Lapresta-Fernández, A.; Santoyo-Gonzalez, F.; Schrott-Fischer, A. and Capitan-Vallvey, L. F., *Carbon Dots for Copper Detection with Down and Upconversion Fluorescent Properties as Excitation Sources.* Chemical Communications, **2013**. *49*(11): p. 1103-1105.

(72) Ananthanarayanan, A.; Wang, X.; Routh, P.; Sana, B.; Lim, S.; Kim, D.-H.; Lim, K.-H.; Li, J. and Chen, P., *Facile Synthesis of Graphene Quantum Dots from 3d Graphene and Their Application for Fe3+ Sensing.* Advanced Functional Materials, **2014**. *24*(20): p. 3021-3026.

(73) Liu, R.; Wu, D.; Feng, X. and Müllen, K., *Bottom-up Fabrication of Photoluminescent Graphene Quantum Dots with Uniform Morphology.* Journal of the American Chemical Society, **2011**. *133*(39): p. 15221-15223.

(74) *One-Step Synthesis of Surface Passivated Carbon Nanodots by Microwave Assisted Pyrolysis for Enhanced Multicolor Photoluminescence and Bioimaging.* J. Mater. Chem., **2011**. *21*: p. 13163.

(75) *Highly Luminescent Carbon Nanodots by Microwave-Assisted Pyrolysis.* Chem. Commun., **2012**. *48*: p. 7955.

(76) Tao, H.; Yang, K.; Ma, Z.; Wan, J.; Zhang, Y.; Kang, Z. and Liu, Z., *In Vivo Nir Fluorescence Imaging, Biodistribution, and Toxicology of Photoluminescent Carbon Dots Produced from Carbon Nanotubes and Graphite.* Small, **2012**. *8*(2): p. 281-290.

(77) *One-Step and High Yield Simultaneous Preparation of Single- and Multi-Layer Graphene Quantum Dots from Cx-72 Carbon Black.* J. Mater. Chem., **2012**. *22*: p. 8764.

(78) Li, H.; He, X.; Kang, Z.; Huang, H.; Liu, Y.; Liu, J.; Lian, S.; Tsang, C. H. A.; Yang, X. and Lee, S.-T., *Water-Soluble Fluorescent Carbon Quantum Dots and Photocatalyst Design.* Angewandte Chemie International Edition, **2010**. *49*(26): p. 4430-4434.

(79) *An Electrochemical Avenue to Green-Luminescent Graphene Quantum Dots as Potential Electron-Acceptors for Photovoltaics.* Adv. Mater., **2011**. *23*: p. 776.

(80) Cheng, K.-Y.; Anthony, R.; Kortshagen, U. R. and Holmes, R. J., *High-Efficiency Silicon Nanocrystal Light-Emitting Devices.* Nano Letters, **2011**. *11*(5): p. 1952-1956.

(81) Askari, S.; Macias-Montero, M.; Velusamy, T.; Maguire, P.; Svrcek, V. and Mariotti, D., *Silicon-Based Quantum Dots: Synthesis, Surface and Composition Tuning with Atmospheric Pressure Plasmas.* Journal of Physics D: Applied Physics, **2015**. *48*(31): p. 314002.

(82) Shen, J.; Zhu, Y.; Chen, C.; Yang, X. and Li, C., *Facile Preparation and Upconversion Luminescence of Graphene Quantum Dots.* Chem Commun, **2011**. *47*.

(83) Shen, J.; Zhu, Y.; Yang, X.; Zong, J.; Zhang, J. and Li, C., *One-Pot Hydrothermal Synthesis of Graphene Quantum Dots Surface-Passivated by Polyethylene Glycol and Their Photoelectric Conversion under near-Infrared Light.* New Journal of Chemistry, **2012**. *36*(1): p. 97-101.

(84) Pan, D.; Zhang, J.; Li, Z. and Wu, M., *Hydrothermal Route for Cutting Graphene Sheets into Blue-Luminescent Graphene Quantum Dots.* Advanced Materials, **2010**. *22*(6): p. 734-738.

(85) Yang, Z.-C.; Li, X. and Wang, J., *Intrinsically Fluorescent Nitrogen-Containing Carbon Nanoparticles Synthesized by a Hydrothermal Process.* Carbon, **2011**. *49*(15): p. 5207-5212.

(86) Teng, C.-Y.; Yeh, T.-F.; Lin, K.-I.; Chen, S.-J.; Yoshimura, M. and Teng, H., *Synthesis of Graphene Oxide Dots for Excitation-Wavelength Independent Photoluminescence at High Quantum Yields.* Journal of Materials Chemistry C, **2015**. *3*(17): p. 4553-4562.

(87) Yeh, T.-F.; Huang, W.-L.; Chung, C.-J.; Chiang, I. T.; Chen, L.-C.; Chang, H.-Y.; Su, W.-C.; Cheng, C.; Chen, S.-J. and Teng, H., *Elucidating Quantum Confinement in Graphene Oxide Dots Based on Excitation-Wavelength-Independent Photoluminescence.* The Journal of Physical Chemistry Letters, **2016**. *7*(11): p. 2087-2092.

(88) Kellici, S.; Acord, J.; Power, N. P.; Morgan, D. J.; Coppo, P.; Heil, T. and Saha, B., *Rapid Synthesis of Graphene Quantum Dots Using a Continuous Hydrothermal Flow Synthesis Approach.* RSC Advances, **2017**. *7*(24): p. 14716-14720.

(89) Zhang, M.; Bai, L.; Shang, W.; Xie, W.; Ma, H.; Fu, Y.; Fang, D.; Sun, H.; Fan, L.; Han, M.; Liu, C. and Yang, S., *Facile Synthesis of Water-Soluble, Highly Fluorescent Graphene Quantum Dots as a Robust Biological Label for Stem Cells.* Journal of Materials Chemistry, **2012**. *22*(15): p. 7461-7467.

(90) Kwon, W.; Kim, Y.-H.; Lee, C.-L.; Lee, M.; Choi, H. C.; Lee, T.-W. and Rhee, S.-W., *Electroluminescence from Graphene Quantum Dots Prepared by Amidative Cutting of Tattered Graphite.* Nano Letters, **2014**. *14*(3): p. 1306-1311.

(91) Li, L.; Wu, G.; Yang, G.; Peng, J.; Zhao, J. and Zhu, J.-J., *Focusing on Luminescent Graphene Quantum Dots: Current Status and Future Perspectives.* Nanoscale, **2013**. *5*(10): p. 4015-4039.

(92) Parker, C. A. and Rees, W. T., *Correction of Fluorescence Spectra and Measurement of Fluorescence Quantum Efficiency.* Analyst, **1960**. *85*(1013): p. 587-600.

(93) Shahzad, A.; Köhler, G.; Knapp, M.; Gaubitzer, E.; Puchinger, M. and Edetsberger, M., *Emerging Applications of Fluorescence Spectroscopy in Medical Microbiology Field.* Journal of translational medicine, **2009**. *7*: p. 99-99.

(94) *The Applications of Fluorescence.* Nature, **1936**. *137*(3464): p. 489-489.

(95) Rost, F., *Fluorescence Microscopy, Applications,* in *Encyclopedia of Spectroscopy and Spectrometry*, J.C. Lindon, Editor. 1999, Elsevier: Oxford. p. 565-570.

(96) Shahzad, A.; Knapp, M.; Edetsberger, M.; Puchinger, M.; Gaubitzer, E. and Köhler, G., *Diagnostic Application of Fluorescence Spectroscopy in Oncology Field: Hopes and Challenges.* Applied Spectroscopy Reviews, **2010**. *45*(1): p. 92-99.

(97) Michels, K.; Heinke, R.; Schöne, P.; Kuipers, O. P.; Arnold, N. and Wessjohann, L. A., *A Fluorescence-Based Bioassay for Antibacterials and Its Application in Screening Natural Product Extracts.* The Journal of Antibiotics, **2015**. *68*(12): p. 734-740.

(98) Shea, J. J., *Electronic Materials and Processes Handbook, 3rd Edition [Book Review].* IEEE Electrical Insulation Magazine, **2004**. *20*(5): p. 45-46.

(99) Zhimin, L.; Guangqin, Q.; Keyu, C.; Min, Z.; Lihui, Y.; Xinwen, Z.; Wei, H. and Lianhui, W., *Microwave-Assisted Preparation of White Fluorescent Graphene Quantum Dots as a Novel Phosphor for Enhanced White-Light-Emitting Diodes.* Advanced Functional Materials, **2016**. *26*(16): p. 2739-2744.

(100) Hou, X.; Li, Y. and Zhao, C., *Microwave-Assisted Synthesis of Nitrogen-Doped Multi-Layer Graphene Quantum Dots with Oxygen-Rich Functional Groups.* Australian Journal of Chemistry, **2016**. *69*(3): p. 357-360.

(101) Kumar, S.; Aziz, S. K. T.; Girshevitz, O. and Nessim, G. D., *One-Step Synthesis of N-Doped Graphene Quantum Dots from Chitosan as a Sole Precursor Using Chemical Vapor Deposition.* The Journal of Physical Chemistry C, **2018**. *122*(4): p. 2343-2349.

(102) Eda, G.; Lin, Y.-Y.; Mattevi, C.; Yamaguchi, H.; Chen, H.-A.; Chen, I. S.; Chen, C.-W. and Chhowalla, M., *Blue Photoluminescence from Chemically Derived Graphene Oxide.* Advanced Materials, **2010**. *22*(4): p. 505-509.

(103) Wang, L.; Zhu, S.-J.; Wang, H.-Y.; Qu, S.-N.; Zhang, Y.-L.; Zhang, J.-H.; Chen, Q.-D.; Xu, H.-L.; Han, W.; Yang, B. and Sun, H.-B., *Common Origin of Green Luminescence in Carbon Nanodots and Graphene Quantum Dots.* ACS Nano, **2014**. *8*(3): p. 2541-2547.

(104) Wang, L.; Wang, H.; Wang, Y.; Zhu, S.; Zhang, Y. and Zhang, J., *Direct Observation of Quantum-Confined Graphene-Like States and Novel Hybrid States in Graphene Oxide by Transient Spectroscopy.* Adv Mater, **2013**. *25*.

(105) Xu, Q.; Zhou, Q.; Hua, Z.; Xue, Q.; Zhang, C.; Wang, X.; Pan, D. and Xiao, M., *Single-Particle Spectroscopic Measurements of Fluorescent Graphene Quantum Dots.* ACS Nano, **2013**. *7*(12): p. 10654-10661.

(106) Sung, J.-H.; Yang, J. S.; Kim, B.-S.; Choi, C.-H.; Lee, M.-W.; Lee, S.-G.; Park, S.-G.; Lee, E.-H. and O, B.-H., *Enhancement of Electroluminescence in Gan-Based Light-Emitting Diodes by Metallic Nanoparticles.* Applied Physics Letters, **2010**. *96*(26): p. 261105.

(107) Tordera, D.; Delgado, M.; Ortí, E.; Bolink, H. J.; Frey, J.; Nazeeruddin, M. K. and Baranoff, E., *Stable Green Electroluminescence from an Iridium Tris-Heteroleptic Ionic Complex.* Chemistry of Materials, **2012**. *24*(10): p. 1896-1903.

(108) Benedict, S. R., *The Determination of Sugar and Saccharoids, Nonfermentable Copper-Reducing Substances.* . Jour. Biol. Chem. , **1931**. *92*(141).

(109) Park, J.; Jeon, O. C.; Yun, J.; Nam, H.; Hwang, J.; Al-Hilal, T. A.; Kim, K.; Kim, K. and Byun, Y., *End-Site-Specific Conjugation of Enoxaparin and Tetradeoxycholic Acid Using Nonenzymatic Glycosylation for Oral Delivery.* Journal of Medicinal Chemistry, **2016**. *59*(23): p. 10520-10529.

(110) Hasan, M. T.; Bhalla, A. and Guo, R., *Investigation of Electrical, Optical and Structural Properties of Sputtered Indium Tin Oxide Thin Film*. Spie Optical Engineering + Applications. Vol. 9586. 2015: SPIE.

(111) Yang, Q.; Duan, J.; Yang, W.; Li, X.; Mo, J.; Yang, P. and Tang, Q., *Nitrogen-Doped Carbon Quantum Dots from Biomass Via Simple One-Pot Method and Exploration of Their Application.* Applied Surface Science, **2018**. *434*: p. 1079-1085.

(112) Ding, H.; Wei, J.-S. and Xiong, H.-M., *Nitrogen and Sulfur Co-Doped Carbon Dots with Strong Blue Luminescence.* Nanoscale, **2014**. *6*(22): p. 13817-13823.

(113) Do, S.; Kwon, W.; Kim, Y.-H.; Kang, S. R.; Lee, T.; Lee, T.-W. and Rhee, S.-W., *N,S-Induced Electronic States of Carbon Nanodots toward White Electroluminescence.* Advanced Optical Materials, **2016**. *4*(2): p. 276-284.

(114) Qu, D.; Zheng, M.; Du, P.; Zhou, Y.; Zhang, L.; Li, D.; Tan, H.; Zhao, Z.; Xie, Z. and Sun, Z., *Highly Luminescent S, N Co-Doped Graphene Quantum Dots with Broad Visible Absorption Bands for Visible Light Photocatalysts.* Nanoscale, **2013**. *5*(24): p. 12272-12277.

(115) Jian, G.; Xiaoping, Z.; Aimin, P. and Jun, Y., *Facile Synthesis and Photoluminescence Characteristics of Blue-Emitting Nitrogen-Doped Graphene Quantum Dots.* Nanotechnology, **2016**. *27*(16): p. 165704.

(116) Ben Aoun, S., *Nanostructured Carbon Electrode Modified with N-Doped Graphene Quantum Dots–Chitosan Nanocomposite: A Sensitive Electrochemical Dopamine Sensor.* Royal Society Open Science, **2017**. *4*(11): p. 171199.

(117) Pan, D.; Zhang, J.; Li, Z. and Wu, M., *Hydrothermal Route for Cutting Graphene Sheets into Blue-Luminescent Graphene Quantum Dots.* Adv Mater, **2010**. *22*.

(118) Hasan, M. T.; Senger, B. J.; Ryan, C.; Culp, M.; Gonzalez-Rodriguez, R.; Coffer, J. L. and Naumov, A. V., *Optical Band Gap Alteration of Graphene Oxide Via Ozone Treatment.* Scientific Reports, **2017**. *7*(1): p. 6411.

(119) Kozawa, D.; Zhu, X.; Miyauchi, Y.; Mouri, S.; Ichida, M.; Su, H. and Matsuda, K., *Excitonic Photoluminescence from Nanodisc States in Graphene Oxides.* The Journal of Physical Chemistry Letters, **2014**. *5*(10): p. 1754-1759.

(120) Bao, L.; Zhang, Z.-L.; Tian, Z.-Q.; Zhang, L.; Liu, C.; Lin, Y.; Qi, B. and Pang, D.-W., *Electrochemical Tuning of Luminescent Carbon Nanodots: From Preparation to Luminescence Mechanism.* Advanced Materials, **2011**. *23*(48): p. 5801-5806.

(121) Shang, J.; Ma, L.; Li, J.; Ai, W.; Yu, T. and Gurzadyan, G. G., *The Origin of Fluorescence from Graphene Oxide.* Scientific Reports, **2012**. *2*: p. 792.

(122) Li, X.; Zhang, S.; Kulinich, S. A.; Liu, Y. and Zeng, H., *Engineering Surface States of Carbon Dots to Achieve Controllable Luminescence for Solid-Luminescent Composites and Sensitive Be2+ Detection.* Scientific Reports, **2014**. *4*: p. 4976.

(123) Wu, X.; Tian, F.; Wang, W.; Chen, J.; Wu, M. and Zhao, J. X., *Fabrication of Highly Fluorescent Graphene Quantum Dots Using L-Glutamic Acid for in Vitro/in Vivo Imaging and Sensing.* Journal of materials chemistry. C, Materials for optical and electronic devices, **2013**. *1*(31): p. 4676-4684.

(124) Hasan, M. T.; Gonzalez-Rodriguez, R.; Ryan, C.; Pota, K.; Green, K.; Coffer, J. L. and Naumov, A. V., *Nitrogen-Doped Graphene Quantum Dots: Optical Properties Modification and Photovoltaic Applications.* Nano Research, **2019**. *12*(5): p. 1041-1047.

(125) Mirtchev, P.; Henderson, E. J.; Soheilnia, N.; Yip, C. M. and Ozin, G. A., *Solution Phase Synthesis of Carbon Quantum Dots as Sensitizers for Nanocrystalline Tio2 Solar Cells.* Journal of Materials Chemistry, **2012**. *22*(4): p. 1265-1269.

(126) Zhang, Y.-Q.; Ma, D.-K.; Zhang, Y.-G.; Chen, W. and Huang, S.-M., *N-Doped Carbon Quantum Dots for Tio2-Based Photocatalysts and Dye-Sensitized Solar Cells.* Nano Energy, **2013**. *2*(5): p. 545-552.

(127) Briscoe, J.; Marinovic, A.; Sevilla, M.; Dunn, S. and Titirici, M., *Biomass-Derived Carbon Quantum Dot Sensitizers for Solid-State Nanostructured Solar Cells.* Angewandte Chemie International Edition, **2015**. *54*(15): p. 4463-4468.

(128) Kwon, W.; Lee, G.; Do, S.; Joo, T. and Rhee, S. W., *Size-Controlled Soft-Template Synthesis of Carbon Nanodots toward Versatile Photoactive Materials.* Small, **2014**. *10*(3): p. 506-513.

(129) Narayanan, R.; Deepa, M. and Srivastava, A. K., *Förster Resonance Energy Transfer and Carbon Dots Enhance Light Harvesting in a Solid-State Quantum Dot Solar Cell.* Journal of Materials Chemistry A, **2013**. *1*(12): p. 3907-3918.

(130) Qian, F.; Li, X.; Tang, L.; Lai, S. K.; Lu, C. and Lau, S. P., *Potassium Doping: Tuning the Optical Properties of Graphene Quantum Dots.* AIP Advances, **2016**. *6*(7): p. 075116.

(131) Dong, Y.; Zhang, S.; Shi, L.; Chen, Y.; Ma, J.; Guo, S.; Chen, X. and Song, H., *The Photoluminescence of Step-Wise Reduced Graphene Oxide Quantum Dots.* Materials Chemistry and Physics, **2018**. *203*: p. 125-132.

(132) Jin, S. H.; Kim, D. H.; Jun, G. H.; Hong, S. H. and Jeon, S., *Tuning the Photoluminescence of Graphene Quantum Dots through the Charge Transfer Effect of Functional Groups.* ACS Nano, **2013**. *7*(2): p. 1239-1245.

(133) Tista, B. and Tushima, B., *Effect of Carrier Doping and External Electric Field on the Optical Properties of Graphene Quantum Dots.* IOP Conference Series: Materials Science and Engineering, **2018**. *310*(1): p. 012014.

(134) Hai, X.; Feng, J.; Chen, X. and Wang, J., *Tuning the Optical Properties of Graphene Quantum Dots for Biosensing and Bioimaging.* Journal of Materials Chemistry B, **2018**. *6*(20): p. 3219-3234.

(135) Zhao, M., *Direct Synthesis of Graphene Quantum Dots with Different Fluorescence Properties by Oxidation of Graphene Oxide Using Nitric Acid.* Applied Sciences, **2018**. *8*(8): p. 1303.

(136) Yu, P.; Wen, X.; Toh, Y.-R. and Tang, J., *Temperature-Dependent Fluorescence in Carbon Dots.* The Journal of Physical Chemistry C, **2012**. *116*(48): p. 25552-25557.

(137) Tian, Y.; Li, L.; Guo, X.; Wójtowicz, A.; Estevez, L.; Krysmann, M. J. and Kelarakis, A., *Dramatic Photoluminescence Quenching in Carbon Dots Induced by Cyclic Voltammetry.* Chemical Communications, **2018**. *54*(65): p. 9067-9070.

(138) Gao, F.; Liu, F.; Bai, X.; Xu, X.; Kong, W.; Liu, J.; Lv, F.; Long, L.; Yang, Y. and Li, M., *Tuning the Photoluminescence of Graphene Oxide Quantum Dots by Photochemical Fluorination.* Carbon, **2019**. *141*: p. 331-338.

(139) Carolan, D.; Rocks, C.; Padmanaban, D. B.; Maguire, P.; Svrcek, V. and Mariotti, D., *Environmentally Friendly Nitrogen-Doped Carbon Quantum Dots for Next Generation Solar Cells.* Sustainable Energy & Fuels, **2017**. *1*(7): p. 1611-1619.

(140) Wang, H.; Sun, P.; Cong, S.; Wu, J.; Gao, L.; Wang, Y.; Dai, X.; Yi, Q. and Zou, G., *Nitrogen-Doped Carbon Dots for "Green" Quantum Dot Solar Cells.* Nanoscale Research Letters, **2016**. *11*(1): p. 27.

(141) Guo, X.; Zhang, H.; Sun, H.; Tade, M. O. and Wang, S., *Green Synthesis of Carbon Quantum Dots for Sensitized Solar Cells.* ChemPhotoChem, **2017**. *1*(4): p. 116-119.

(142) Vougioukalakis, G. C.; Philippopoulos, A. I.; Stergiopoulos, T. and Falaras, P., *Contributions to the Development of Ruthenium-Based Sensitizers for Dye-Sensitized Solar Cells.* Coordination Chemistry Reviews, **2011**. *255*(21): p. 2602-2621.

(143) Lu, K.; Wang, Y.; Liu, Z.; Han, L.; Shi, G.; Fang, H.; Chen, J.; Ye, X.; Chen, S.; Yang, F.; Shulga, A. G.; Wu, T.; Gu, M.; Zhou, S.; Fan, J.; Loi, M. A. and Ma, W., *High-Efficiency Pbs Quantum-Dot Solar Cells with Greatly Simplified Fabrication Processing Via "Solvent-Curing".* Advanced Materials, **2018**. *30*(25): p. 1707572.

(144) Huang, F.; Zhang, L.; Zhang, Q.; Hou, J.; Wang, H.; Wang, H.; Peng, S.; Liu, J. and Cao, G., *High Efficiency Cds/Cdse Quantum Dot Sensitized Solar Cells with Two Znse Layers.* ACS Applied Materials & Interfaces, **2016**. *8*(50): p. 34482-34489.

(145) Derfus, A. M.; Chan, W. C. W. and Bhatia, S. N., *Probing the Cytotoxicity of Semiconductor Quantum Dots.* Nano Letters, **2004**. *4*(1): p. 11-18.

(146) Bottrill, M. and Green, M., *Some Aspects of Quantum Dot Toxicity*. Chemical Communications, **2011**. *47*(25): p. 7039-7050.

(147) Ba, L.; Liu, H. and Shen, W., *Perovskite/C-Si Tandem Solar Cells with Realistic Inverted Architecture: Achieving High Efficiency by Optical Optimization.* Progress in Photovoltaics: Research and Applications, **2018**. *26*(11): p. 924-933.

(148) Shahrjerdi, D.; Bedell, S. W.; Bayram, C.; Lubguban, C. C.; Fogel, K.; Lauro, P.; Ott, J. A.; Hopstaken, M.; Gayness, M. and Sadana, D., *Ultralight High-Efficiency Flexible Ingap/(in)Gaas Tandem Solar Cells on Plastic.* Advanced Energy Materials, **2013**. *3*(5): p. 566-571.

(149) Hasan, M. T.; Gonzalez-Rodriguez, R.; Ryan, C.; Coffer, J. L. and Naumov, A. V., *Variation of Optical Properties of Nitrogen-Doped Graphene Quantum Dots with Short/Mid/Long-Wave Ultraviolet for the Development of the Uv Photodetector*. ACS Applied Materials & Interfaces, **2019**.

(150) Ji, T.; Hua, Y.; Sun, M. and Ma, N., *The Mechanism of the Reaction of Graphite Oxide to Reduced Graphene Oxide under Ultraviolet Irradiation.* Carbon, **2013**. *54*: p. 412-418.

(151) Yuan, X.; Peng, D.; Jing, Q.; Niu, J.; Cheng, X.; Feng, Z. and Wu, X., *Green and Effective Removal of Aqueous Graphene Oxide under Uv-Light Irradiation.* Nanomaterials, **2018**. *8*(9): p. 654.

(152) Flyunt, R.; Knolle, W.; Kahnt, A.; Halbig, C. E.; Lotnyk, A.; Häupl, T.; Prager, A.; Eigler, S. and Abel, B., *High Quality Reduced Graphene Oxide Flakes by Fast Kinetically Controlled and Clean Indirect Uv-Induced Radical Reduction.* Nanoscale, **2016**. *8*(14): p. 7572-7579.

(153) Zhu, J.; Tang, Y.; Wang, G.; Mao, J.; Liu, Z.; Sun, T.; Wang, M.; Chen, D.; Yang, Y.; Li, J.; Deng, Y. and Yang, S., *Green, Rapid, and Universal Preparation Approach of Graphene Quantum Dots under Ultraviolet Irradiation.* ACS Applied Materials & Interfaces, **2017**. *9*(16): p. 14470-14477.

(154) Zhang, Q.; Jie, J.; Diao, S.; Shao, Z.; Zhang, Q.; Wang, L.; Deng, W.; Hu, W.; Xia, H.; Yuan, X. and Lee, S.-T., *Solution-Processed Graphene Quantum Dot Deep-Uv Photodetectors.* ACS Nano, **2015**. *9*(2): p. 1561-1570.

(155) Reddy, A. G.; Aggarwal, N.; C., S. K. T.; Singh, M.; Rakshit, R. and Gupta, G., *Correlation of Current–Voltage–Temperature Analysis with Deep Level Defects in Epitaxial Gan Films.* Applied Physics Letters, **2015**. *106*(23): p. 233501.

(156) Sharma, A.; Bhattacharyya, B.; Srivastava, A. K.; Senguttuvan, T. D. and Husale, S., *High Performance Broadband Photodetector Using Fabricated Nanowires of Bismuth Selenide.* Scientific Reports, **2016**. *6*: p. 19138.

(157) Aggarwal, N.; Krishna, S.; Sharma, A.; Goswami, L.; Kumar, D.; Husale, S. and Gupta, G., *A Highly Responsive Self-Driven Uv Photodetector Using Gan Nanoflowers.* Advanced Electronic Materials, **2017**. *3*(5): p. 1700036.

(158) Hu, L.; Yan, J.; Liao, M.; Wu, L. and Fang, X., *Ultrahigh External Quantum Efficiency from Thin Sno2 Nanowire Ultraviolet Photodetectors.* Small, **2011**. *7*(8): p. 1012-1017.

(159) Li, L.; Lee, P. S.; Yan, C.; Zhai, T.; Fang, X.; Liao, M.; Koide, Y.; Bando, Y. and Golberg, D., *Ultrahigh-Performance Solar-Blind Photodetectors Based on Individual Single-Crystalline In2ge2o7 Nanobelts.* Advanced Materials, **2010**. *22*(45): p. 5145-5149.

(160) Sharma, A.; Kaur, M.; Bhattacharyya, B.; Karuppiah, S.; Singh, S. P.; Senguttuvan, T. D. and Husale, S., *Channel Length Specific Broadspectral Photosensitivity of Robust Chemically Grown Cds Photodetector.* AIP Advances, **2015**. *5*(4): p. 047116.

(161) Xie, C.; Nie, B.; Zeng, L.; Liang, F.-X.; Wang, M.-Z.; Luo, L.; Feng, M.; Yu, Y.; Wu, C.-Y.; Wu, Y. and Yu, S.-H., *Core–Shell Heterojunction of Silicon Nanowire Arrays and Carbon Quantum Dots for Photovoltaic Devices and Self-Driven Photodetectors.* ACS Nano, **2014**. *8*(4): p. 4015-4022.

(162) Tang, L.; Ji, R.; Li, X.; Bai, G.; Liu, C. P.; Hao, J.; Lin, J.; Jiang, H.; Teng, K. S.; Yang, Z. and Lau, S. P., *Deep Ultraviolet to near-Infrared Emission and Photoresponse in Layered N-Doped Graphene Quantum Dots.* ACS Nano, **2014**. *8*(6): p. 6312-6320.

(163) Kim, C. O.; Hwang, S. W.; Kim, S.; Shin, D. H.; Kang, S. S.; Kim, J. M.; Jang, C. W.; Kim, J. H.; Lee, K. W.; Choi, S.-H. and Hwang, E., *High-Performance Graphene-Quantum-Dot Photodetectors.* Scientific Reports, **2014**. *4*: p. 5603.

(164) Maiti, R.; Mukherjee, S.; Dey, T. and Ray, S. K., *Solution Processed Highly Responsive Uv Photodetectors from Carbon Nanodot/Silicon Heterojunctions.* ACS Applied Nano Materials, **2019**. *2*(6): p. 3971-3976.

(165) Jang, C. W.; Shin, D. H. and Choi, S.-H., *Highly-Flexible and -Stable Deep-Ultraviolet Photodiodes Made of Graphene Quantum Dots Sandwiched between Graphene Layers.* Dyes and Pigments, **2019**. *163*: p. 238-242.

(166) Alam, M. S.; Boby, M. A.; Chowdhury, F. A.; Albrithen, H. and Hossain, M. A., *Influence of Composition on the External Quantum Efficiency of Reduced Graphene Oxide/Carbon Nanoparticle Based Photodetector Used for Human Body Ir Detection.* RSC Advances, **2019**. *9*(33): p. 18996-19005.

(167) Chen, X.; Yang, C.; Sun, H.; Ning, S.; Zhou, H.; Zhang, H.; Wang, S.; Feng, G. and Zhou, S., *Enhanced Photoresponsivity in Carbon Quantum Dots-Coupled Graphene/Silicon Schottky-Junction Photodetector.* Laser Physics Letters, **2019**. *16*(7): p. 076201.

(168) Sahatiya, P.; Jones, S. S. and Badhulika, S., *2d Mos2–Carbon Quantum Dot Hybrid Based Large Area, Flexible Uv–Vis–Nir Photodetector on Paper Substrate.* Applied Materials Today, **2018**. *10*: p. 106-114.

(169) Liu, D.; Li, H.-J.; Gao, J.; Zhao, S.; Zhu, Y.; Wang, P.; Wang, D.; Chen, A.; Wang, X. and Yang, J., *High-Performance Ultraviolet Photodetector Based on Graphene Quantum Dots Decorated Zno Nanorods/Gan Film Isotype Heterojunctions.* Nanoscale Research Letters, **2018**. *13*(1): p. 261.

(170) Sun, M.; Fang, Q.; Xie, D.; Sun, Y.; Qian, L.; Xu, J.; Xiao, P.; Teng, C.; Li, W.; Ren, T. and Zhang, Y., *Heterostructured Graphene Quantum Dot/Wse2/Si Photodetector with Suppressed Dark Current and Improved Detectivity.* Nano Research, **2018**. *11*(6): p. 3233-3243.

(171) Kim, S.; Shin, D. H.; Kim, J.; Jang, C. W.; Kang, S. S.; Kim, J. M.; Kim, J. H.; Lee, D. H.; Kim, J. H.; Choi, S.-H. and Hwang, S. W., *Energy Transfer from an Individual Silica Nanoparticle to Graphene Quantum Dots and Resulting Enhancement of Photodetector Responsivity.* Scientific Reports, **2016**. *6*: p. 27145.

(172) Tsai, M.-L.; Tsai, D.-S.; Tang, L.; Chen, L.-J.; Lau, S. P. and He, J.-H., *Omnidirectional Harvesting of Weak Light Using a Graphene Quantum Dot-Modified Organic/Silicon Hybrid Device.* ACS Nano, **2017**. *11*(5): p. 4564-4570.

(173) Mihalache, I.; Radoi, A.; Pascu, R.; Romanitan, C.; Vasile, E. and Kusko, M., *Engineering Graphene Quantum Dots for Enhanced Ultraviolet and Visible Light P-Si Nanowire-Based Photodetector.* ACS Applied Materials & Interfaces, **2017**. *9*(34): p. 29234-29247.

(174) Shellock, F. G. and Kanal, E., *Safety of Magnetic Resonance Imaging Contrast Agents.* Journal of Magnetic Resonance Imaging, **1999**. *10*(3): p. 477-484.

(175) Cormode, D. P.; Naha, P. C. and Fayad, Z. A., *Nanoparticle Contrast Agents for Computed Tomography: A Focus on Micelles.* Contrast media & molecular imaging, **2014**. *9*(1): p. 37-52.

(176) Hasebroock, K. M. and Serkova, N. J., *Toxicity of Mri and Ct Contrast Agents.* Expert Opinion on Drug Metabolism & Toxicology, **2009**. *5*(4): p. 403-416.

(177) Boghossian , A. A.; Zhang , J.; Barone, P. W.; Reuel, N. F.; Kim, J.-H.; Heller, D. A.; Ahn, J.-H.; Hilmer, A. J.; Rwei, A.; Arkalgud, J. R.; Zhang, C. T. and Strano, M. S., *Near-Infrared Fluorescent Sensors Based on Single-Walled Carbon Nanotubes for Life Sciences Applications.* ChemSusChem, **2011**. *4*(7): p. 848-863.

(178) Mao, H.; Kawazoe, N. and Chen, G., *Uptake and Intracellular Distribution of Collagen-Functionalized Single-Walled Carbon Nanotubes.* Biomaterials, **2013**. *34*(10): p. 2472-2479.

(179) Zhang, M.; Yue, J.; Cui, R.; Ma, Z.; Wan, H.; Wang, F.; Zhu, S.; Zhou, Y.; Kuang, Y.; Zhong, Y.; Pang, D.-W. and Dai, H., *Bright Quantum Dots Emitting at ~1,600 Nm in the Nir-Iib Window for Deep Tissue Fluorescence Imaging.* Proceedings of the National Academy of Sciences, **2018**. *115*(26): p. 6590-6595.

(180) Hinds, S.; Myrskog, S.; Levina, L.; Koleilat, G.; Yang, J.; Kelley, S. O. and Sargent, E. H., *Nir-Emitting Colloidal Quantum Dots Having 26% Luminescence Quantum Yield in Buffer Solution.* Journal of the American Chemical Society, **2007**. *129*(23): p. 7218-7219.

(181) Hu, D.; Zhang, P.; Gong, P.; Lian, S.; Lu, Y.; Gao, D. and Cai, L., *A Fast Synthesis of near-Infrared Emitting Cdte/Cdse Quantum Dots with Small Hydrodynamic Diameter for in Vivo Imaging Probes.* Nanoscale, **2011**. *3*(11): p. 4724-4732.

(182) Roxbury, D.; Jena, P. V.; Williams, R. M.; Enyedi, B.; Niethammer, P.; Marcet, S.; Verhaegen, M.; Blais-Ouellette, S. and Heller, D. A., *Hyperspectral Microscopy of near-Infrared Fluorescence Enables 17-Chirality Carbon Nanotube Imaging.* Scientific Reports, **2015**. *5*: p. 14167.

(183) Huang, X.; Gao, N. and Deng, Y., *Bromate Ion Formation in Dark Chlorination and Ultraviolet/Chlorination Processes for Bromide-Containing Water.* Journal of Environmental Sciences, **2008**. *20*(2): p. 246-251.

(184) Baskin, Y. and Meyer, L., *Lattice Constants of Graphite at Low Temperatures.* Physical Review, **1955**. *100*(2): p. 544-544.

(185) Vieira Ferreira, L. F. and Costa, S. M. B., *Fluorescence Quantum Yield Evaluation of Strongly Absorbing Dye Solutions as a Function of the Dye Concentration.* Journal of Luminescence, **1991**. *48-49*: p. 395-399.

(186) Rurack, K. and Spieles, M., *Fluorescence Quantum Yields of a Series of Red and near-Infrared Dyes Emitting at 600−1000 Nm.* Analytical Chemistry, **2011**. *83*(4): p. 1232-1242.

(187) Ong, K. J.; MacCormack, T. J.; Clark, R. J.; Ede, J. D.; Ortega, V. A.; Felix, L. C.; Dang, M. K. M.; Ma, G.; Fenniri, H.; Veinot, J. G. C. and Goss, G. G., *Widespread Nanoparticle-Assay Interference: Implications for Nanotoxicity Testing.* PloS one, **2014**. *9*(3): p. e90650-e90650.

(188) Holder, A. L.; Goth-Goldstein, R.; Lucas, D. and Koshland, C. P., *Particle-Induced Artifacts in the Mtt and Ldh Viability Assays.* Chemical research in toxicology, **2012**. *25*(9): p. 1885-1892.

(189) Campbell, E.; Hasan, M. T.; Gonzalez Rodriguez, R.; Akkaraju, G. R. and Naumov, A. V., *Doped Graphene Quantum Dots for Intracellular Multicolor Imaging and Cancer Detection.* ACS Biomaterials Science & Engineering, **2019**. *5*(9): p. 4671-4682.

VITA

Personal Background: Md. Tanvir Hasan

Education:

Doctor of Philosophy, Texas Christian University, TX, USA, 2019
Master of Science, Texas Christian University, TX, USA, 2018
Bachelor of Science, Chittagong University of Engineering and Technology, Chittagong, Bangladesh, 2007

Professional Experience:

2015-2019 Graduate Teaching/Research Assistant, Texas Christian University
2013-2014 Graduate Teaching Assistant, The University of Texas at San Antonio
2012-2015 Graduate Research Assistant, The University of Texas at San Antonio
2011-2012 Senior Executive Engineer, Atlas Copco Bangladesh Limited
2008-2010 Executive Engineer, Siemens Bangladesh Limited

Patent and Publications:

1. Lynn Kirkpatrick, Anton V. Naumov, ***Md. Tanvir Hasan*** "Methods and Compositions of Single-Walled Carbon Nanotubes for Treating Liver Diseases", U.S. Provisional Patent Application No. 62/839,920; Filing Date: April 29, 2019
2. ***Md. Tanvir Hasan***, *R. Gonzalez-Rodriguez, C. Ryan, and A. V. Naumov* "Variation of Optical Properties of Nitrogen-doped Graphene Quantum Dots with Short/Mid/Long-wave Ultraviolet for the Development of the UV Photodetector", ACS Applied Materials and Interfaces, doi:10.1021/acsami.9b10365 (2019).
3. ***Md. Tanvir Hasan***, *E. Campbell, V. Lyle, G. R. Akkaraju, L. Kirkpatrick, A. V. Naumov* "Multi-Drug/Gene NASH Therapy Delivery and Selective Hyperspectral Near-IR Imaging Using Chirality-Sorted Single-Walled Carbon Nanotubes." Cancers, doi:10.3390/cancers11081175 (2019).
4. ***Md. Tanvir Hasan***, *R. Gonzalez-Rodriguez, C. Ryan, Kristof Pota, Kayla N. Green, J. L. Coffer and A. V. Naumov* "Nitrogen-doped graphene quantum dots: Optical Properties Modification and Photovoltaic Applications" Nano Research, doi:10.1007/s12274-019-2337-4 (2019).
5. *A. Khazi-Syed,* ***Md. Tanvir Hasan***, *E. Campbell, A. V. Naumov* "Single-Walled Carbon Nanotube-Assisted Antibiotic Delivery and Imaging in S. Epidermidis Strains Addressing Antibiotic Resistance" Nanomaterials, doi: 10.3390/nano9121685 (2019).
6. *E. Campbell,* ***Md. Tanvir Hasan***, *R. Gonzalez-Rodriguez, G.R. Akkaraju, and A. V. Naumov* "Doped Graphene Quantum Dots for Intracellular Multicolor Imaging, and Cancer Detection" ACS Biomaterials Science and Engineering, doi:10.1021/acsbiomaterials.9b00603 (2019).
7. *E. Campbell,* ***Md. Tanvir Hasan***, *C. Pho, K. Callaghan, G.R. Akkaraju, and A. V. Naumov* "Graphene Oxide as a Multifunctional Platform for Intracellular Delivery, Imaging, and Cancer Sensing" Scientific Reports, 9:416, doi:10.1038/s41598-018-36617-4 (2019).
8. ***Md. Tanvir Hasan***, *R. Gonzalez-Rodriguez, C. Ryan, N. Faerber, J. L. Coffer and A. V. Naumov,* Photo-and Electroluminescence from Nitrogen-Doped and Nitrogen–Sulfur Co-doped Graphene Quantum Dots. Advanced Functional Materials, *28*(42): p. 1804337, doi:10.1002/adfm.201804337 (2018).
9. ***Md. Tanvir Hasan***, *B. J. Senger, C. Ryan, M. Culp, R. Gonzalez-Rodriguez, J. L. Coffer, A. V. Naumov* "Optical Band Gap Alteration of Graphene Oxide *via* Ozone Treatment" Scientific Reports, 7(1): p. 6411, doi:10.1038/s41598-017-06107-0 (2017).
10. ***Md Tanvir Hasan***, *B. J. Senger, P. Mulford, C. Ryan, H. Doan, Z. Gryczynski, A. V. Naumov* "Modifying optical properties of reduced/graphene oxide with controlled ozone and thermal treatment in aqueous suspensions" Nanotechnology 28, 065705, doi:10.1088/1361-6528/aa5232 (2017).
11. ***Md. Tanvir Hasan***, *A. Bhalla, R. Guo* "Investigation of Electrical, Optical and Structural Properties of Sputtered Indium Tin Oxide Thin Film" Proc. of SPIE Vol.9586 95860J-1, doi: 10.1117/12.2188971 (2015)
12. ***Md. Tanvir Hasan***, "Characterization and Modification of Optical Properties of Graphene Oxide and Reduced Graphene Oxide" ProQuest, 10843705 (2018) (Masters thesis).
13. ***Md. Tanvir Hasan***, *Ching-Wei Lin, Ainsley McDonald-Boyer, R. Gonzalez-Rodriguez, Bong Han Lee, and A. V. Naumov* "NIR Emitting Graphene Quantum Dots Synthesized *via* Top-down approach for Biological Imaging Applications" Manuscript under preparation (2019).

ABSTRACT

SYNTHESIS, ADVANCED CHARACTERIZATION, AND OPTOELECTRONIC/BIOLOGICAL APPLICATIONS OF NOVEL GRAPHENE QUANTUM DOTS

By Md. Tanvir Hasan, 2019
Department of Physics and Astronomy, Texas Christian University
Thesis Advisor: Dr. Anton V. Naumov, Assistant Professor

In this work, we focus on developing novel graphene quantum dots (GQDs) utilizing two separate synthetic approaches (bottom-up/top-down) and exploring their optoelectronic and bioimaging applications. Nitrogen-doped (N-GQDs) and nitrogen/sulfur co-doped (NS-GQDs) GQDs are synthesized with glucosamine/thiourea precursor *via* a simple/cost-effective microwave-facilitated hydrothermal method yielding water-soluble GQDs showing excitation-dependent fluorescence in the visible and near-infrared with high quantum yield. These GQDs are applied further to fabricate electroluminescence (EL) devices, solar cells, and UV photodetectors. The fabricated EL devices with N-GQDs as an emissive layer show bright EL emission with moderate turn-on voltage (~7V) indicating that the synthesized quantum dots are a promising material for low cost eco-friendly organic LEDs. The optical properties of as-prepared N-GQDs are optimized further via the controlled ozone treatment providing significant enhancement of photovoltaic performances of GQDs-based solar cells such as fill factor (28 to 86.40%), PCE (0.41 to 2.64%), I_{sc} (1.13 to 4.8mAcm^{-2}), and V_{oc} (0.57 to 0.83V)

over those with untreated N-GQDs. Further significant modification of optical/structural properties of N-GQDs takes place under short (254 nm)/mid (302 nm)/long-wave (365 nm) UV irradiation leading us to fabricate UV photodetectors using untreated/UV-treated NGQDs as a sensitizer. These devices provide highly reproducible and fast photo-switching characteristics with high photosensitivity up to 0.59 A/W and excellent photodetectivity up to $1.03X10^{11}$ Jones. In the separate work on biological applications, these GQDs are utilized for multi-color *in-vitro* imaging and pH-dependent fluorescence-based ratiometric cancer detection.

On the other hand, a separate UV-driven aqueous top-down approach was developed to synthesize novel fluorescing GQDs (RGQDs) from optically inert reduced graphene oxide. Those exhibit partially excitation-independent emission in the visible and NIR-I (~950 nm) with quantum yields from ~1.4 to ~8%. As-synthesized RGQDs with an average size of 3.54±0.05 nm are biocompatible with ~80% cell viability up to a high 1mg/mL concentrations as verified *via* MTT and Luminescence cytotoxicity assays. Due to advantageous high tissue penetration depth NIR emission, small size, high water solubility, and biocompatibility, RGQDs are utilized as both in-vitro/in-vivo bioimaging agents. *In vitro* study indicates effective cellular internalization with observable intracellular NIR/VIS fluorescence from RGQDs compared to the control, whereas in-vivo/ex-vivo mice imaging shows RGQD accumulation mainly in the spleen, kidney, liver, and intestine suggesting a promising material for image-guided drug delivery.